Modeling and Estimation for Non-invasive Monitoring of Intracranial Pressure and Cerebrovascular Autoregulation

by

Faisal M. Kashif

B.Sc. (2000), Electronic Engineering, Ghulam Ishaq Khan Institute, Pakistan
S.M. (2006), Massachusetts Institute of Technology

Submitted to the Department of Electrical Engineering and Computer Science
in partial fulfillment of the requirements for the degree of

Doctor of Philosophy

at the

MASSACHUSETTS INSTITUTE OF TECHNOLOGY

June 2011

Author ....
Department of Electrical Engineering and Computer Science
April 15, 2011

Certified by.....
Professor George C. Verghese
Professor of Electrical Engineering
Thesis Co-supervisor

Certified by.....
Dr. Thomas Heldt
Research Scientist
Thesis Co-supervisor

Accepted by ...
Professor Leslie A. Kolodziejski
Chairman, Department Committee on Graduate Students

Modeling and Estimation for Non-invasive Monitoring of Intracranial Pressure and Cerebrovascular Autoregulation

by

Faisal M. Kashif

Submitted to the Department of Electrical Engineering and Computer Science
on April 15, 2011, in partial fulfillment of the
requirements for the degree of
Doctor of Philosophy

Abstract

Brain tissue is highly vulnerable to unbalanced oxygen demand and supply. A few seconds of oxygen deficit may trigger neurological symptoms, and sustained oxygen deprivation over a few minutes may result in severe and often irreversible brain damage. The rapid dynamics coupled with the potential for severe injury necessitate continuous cerebrovascular monitoring in the populations at greatest risk for developing or exacerbating brain injury. Intracranial pressure (ICP), which is the pressure of the cerebrospinal fluid, is a vitally important variable to monitor in a wide spectrum of medical conditions involving the brain, such as traumatic brain injury, stroke, hydrocephalus, or brain tumors. However, clinical measurement of ICP is highly invasive, as it requires neurosurgical penetration of the skull and placement of a pressure sensor in the brain tissue or ventricular spaces. Measurement of ICP is thus currently limited to only those patient populations in which the benefits of obtaining the measurement outweigh the significant attendant risks, thus excluding a large pool of patients who could potentially benefit from ICP monitoring. The primary goal of our work is to address the non-invasive monitoring of ICP. A secondary aim of this work is to develop methods for the assessment of cerebrovascular autoregulation, which is the innate ability of the vasculature to maintain cerebral blood flow in the face of changes in cerebral perfusion pressure. Cerebrovascular autoregulation is often impaired in patients with brain trauma or stroke, and also in pre-term neonates, as their cerebrovascular system is not fully matured.

We develop methods for *non-invasive*, *continuous*, *calibration-free* and *patient-specific* ICP monitoring. Specifically, we present a model-based approach to providing real-time estimates of ICP and cerebrovascular resistance and compliance, for each cardiac cycle, from non- or minimally-invasive time-synchronized measurements of arterial blood pressure and cerebral blood flow velocity in a major cerebral artery. In the first step, our approach exploits certain features of cerebrovascular physiology, along with model reduction ideas, to deduce a simple mathematical model of the cerebrovascular system. In the second step, we develop algorithms to compute robust estimates of model parameters by processing the measured waveforms through the

constraints provided by the models dynamic equation.

For validation, our non-invasive estimates of ICP were compared against invasive measurements from 45 comatose brain-injury patients, with a total of 35 hours of data (over 150,000 beats), providing more than 3,500 independent ICP estimates. Our estimates track measured ICP closely over a range of dynamic variations. Pooling all independent estimates resulted in a mean estimation error (bias) of less than 2 mmHg and a standard deviation of error of about 8 mmHg. We also suggest how variations in estimated cerebrovascular resistance and compliance in response to variations in cerebral perfusion pressure may be used to provide novel approaches for assessment of cerebrovascular autoregulation.

Thesis Co-supervisor: Professor George C. Verghese
Title: Professor of Electrical Engineering

Thesis Co-supervisor: Dr. Thomas Heldt
Title: Research Scientist

Acknowledgments

It is a pleasure to thank those who made this thesis possible. First and foremost, I thank my thesis advisors, Professor George Verghese and Dr. Thomas Heldt. This work would have not been possible without their constant mentoring, advice, encouragement, exchange of ideas, and discussions throughout the project. In particular, whenever there were any obstacles to overcome, they dedicated time to go over my problems for as long as it took to get them completely resolved. In the final phase of writing, they have dedicated huge chunks of their time to read my several drafts, provide me with critical feedback, and guide me through several iterations. I am immensely grateful for their support, on both the professional and personal level.

That George is an excellent advisor, you will hear from everyone out there. But what touched me most was George as a person; his care, compassion and impeccable standards of ethics are simply exemplary. I feel that I have learned even more on this side of things from him than about the particular items that are the topic of this dissertation. Thank you, George, for everything you did for me!

I have spent a tremendous amount of time with Thomas since my joining this group in January 2007. Thomas is a great person, an extremely dedicated researcher, and a super advisor. The way he took time out to meet and discuss various research problems is only one aspect of his impact on my work. He has gone above and beyond the usual responsibilities of an advisor to keep me focused and help me meet my deadlines, even if it meant spending his vacations reading my drafts. As a friend, he has helped me numerous times to overcome problems outside research. Thank you very much, Thomas!

I would like to thank Dr. Vera Novak of Boston's Beth Israel Deaconess Medical Center (BIDMC) for very helpful discussions, ideas, and support throughout this work. Vera guided us at the initial stages of this project, when we were exploring cerebrovascular modeling and estimation. Her role has been very instrumental in setting our goals and planning our work. She also provided us with data from a stroke study for our exploration of cerebrovascular autoregulation. Finally, Vera served on

my thesis committee, for which I owe her much gratitude.

Dr. Marek Czosnyka at the University of Cambridge, UK, has very generously provided us the patient data that were essential for validation of the work presented in this thesis. We have interacted across the Atlantic all this time. However, the promptness of his responses to our never-ending questions was as if he were at MIT (in Cambridge, MA), which helped to make ours a fruitful collaboration. I am greatly inspired by his energy and enthusiasm to advance the field of cerebrovascular monitoring and non-invasive monitoring of ICP. I am indebted to him for his kind support in this work.

I am honored to have had Professor Roger Mark of MIT on my thesis committee, and thank him for several discussions, thoughtful criticism and advice, and careful reading and feedback on my thesis draft. He has inspired numerous people who work in the field of biomedicine, and I too feel fortunate to have learned from him.

I thank Dr. Adré du Plessis, who is now at the Children's National Medical Center, Washington DC. He exposed us to the field of neonatal neurological monitoring. I learnt a great deal from him about this field during our regular meetings at the Children's Hospital, Boston. Adré's passion and dedication for advancing this field are contagious, and I feel lucky to have been affiliated to his group in Boston.

Special thanks are due to Dr. Ajith Thomas of BIDMC for sharing his experience — as a neurosurgeon — in the monitoring of patients with severe brain injury. Dr. Thomas has been a great supporter of this project, and has encouraged us to advance in the field of ICP monitoring.

Several colleagues provided support during these four years. I thank members of the Computational Physiology and Clinical Inference group and my colleagues at LEES at MIT, and members of the Fetal/Neonatal Brain Development and Injury group at the Children's Hospital, Boston. I want particularly to thank Irena Hwang, who started working on this project with me a few months ago, and has already helped advance this work.

Support from friends surely made life easier. I thank Asif Khan, Zaid Samar, Tariq Hussain, Tariq Bashir, Rehan Tahir, Tushar Parlikar, Demba Ba, Bill Richoux and

Gireeja Ranade. Special thanks are due to Jahanzeb Latif, Hassan Saud, Safdar Ali and Imran Zaman for their care and support. I thank Khurram Afridi for his guidance and encouragement. I thank Zubair Anwar and his family for their friendship and care over the years, particularly during the crunch times. I also thank Zahid Yaqoob and his family for their support and love. Finally, I would like to thank Wajih Umar and his family, who have always been there for me. Wajih and I have discussed several issues related to this research in detail, and he has been very supportive of my work.

Now comes the list of silent contributions: I thank my parents, brothers, and sisters for their love, care and support. They have nurtured me, taught me, given me confidence to go out in the world, and did everything in their capacity to help me grow. Finally, I want to thank my wife Misbah, without whose help this work would not have been completed in this way. In the last year and a half, she has taken care of so many matters alone, to allow me to focus on my work. She easily owns more than half of what I have accomplished in this thesis. Our little daughter, Haniyah, who was born during the days of writing this thesis, has filled our lives with happiness, and made looking to the future very pleasant.

I hope the contributions in this thesis will eventually be helpful in saving lives and improving the quality of life of those who suffer from brain injury or cerebrovascular disease. I dedicate the rewards of my effort to my parents, my siblings, Misbah, and Haniyah.

I thank MIT and the Center for Integration of Medicine and Innovative Technology (CIMIT) for a two-year Medical Engineering Fellowship. I also thank the Higher Education Commission of Pakistan for providing support in starting my graduate program. This work was also supported in part by the National Institute of Biomedical Imaging and Bioengineering of the National Institutes of Health through grant R01 EB 001659.

Contents

Contents 9

List of Figures 13

List of Tables 21

1 Introduction 23

1.1 Background 23

1.2 Motivation 25

1.3 Approach 26

1.4 Thesis Contributions 28

1.5 Organization of Thesis 30

I Cerebrovascular Physiology and Neuro-critical Monitoring 31

2 Cerebrovascular Physiology and Brain Injury 33

2.1 Physiology 33

2.1.1 Brain tissue 34

2.1.2 Cerebrovascular physiology 36

2.1.3 Cerebrospinal physiology 42

2.2 Epidemiology of Brain Injury 47

2.3 Pathophysiology of Brain Injury 48

2.3.1 Cerebral edema 49

2.3.2 Intracranial hemorrhage 50
2.3.3 Moderate and mild TBI 50

3 Cerebrovascular Monitoring **51**
3.1 Methods of ICP Measurement 52
3.2 Assessment of Cerebrovascular Autoregulation 55
3.3 Approaches to Non-invasive ICP Estimation 60
3.4 Potential Impact of Non-invasive ICP Monitoring 64

II Mathematical Modeling and Estimation **67**

4 Models of the Cerebrovascular System and Intracranial Dynamics **69**
4.1 Background on Modeling Approaches 70
4.1.1 Black-box and statistical models 70
4.1.2 Physiological models 72
4.2 Review of Cerebrovascular Models 74
4.2.1 A Simple Ursino-Lodi model 80
4.3 Modified Ursino-Lodi Model 84
4.4 Reduced Model for ICP Estimation 87
4.4.1 Simple compartmental view of cerebrovascular system 88
4.4.2 Model 89
4.4.3 Validation via simulation 91
4.5 Salient Features of the Reduced Model 91
4.6 Concluding Remarks 93

5 Model Parameter Estimation **95**
5.1 Estimation Algorithm 96
5.2 Clinical Measurements 100
5.2.1 Arterial blood pressure 100
5.2.2 Cerebral blood flow (velocity) 101
5.2.3 Discrepancy between available and desired measurements . . . 102

5.3 Pre-processing and Phase-offset Estimation 104
5.3.1 Pre-processing steps 105
5.3.2 Phase-offset estimation 106
5.4 Summary of Estimation Algorithm 108
5.4.1 Utilizing input signal quality in estimation algorithm 108
5.5 Key Features of Estimation Approach 110
5.6 Concluding Remarks 111

III Validation and Performance Analysis 113

6 ICP Estimation Performance 115
6.1 Validation Data 116
6.2 ICP Estimates and Error Statistics 117
6.2.1 Comparison of beat-by-beat estimates 118
6.2.2 Comparing independent estimates across all records 122
6.2.3 Correlation analysis of ICP estimation error 127
6.2.4 Estimates using bilateral TCD 129
6.3 Discussion 131
6.3.1 What is acceptable clinical accuracy? 131
6.3.2 Estimation accuracy 133
6.3.3 Sources of error in our nICP estimation 133
6.4 Concluding Remarks 136

7 Exploring Model-Based Assessment of Cerebrovascular Autoregulation 139
7.1 Using R and CPP Estimates to Assess Autoregulation 140
7.1.1 Example 1 141
7.1.2 Example 2 144
7.1.3 Why MAP *alone* fails to tell the story? 145
7.2 Exploratory Study Involving Stroke Patients 147
7.2.1 Data and interventions 148

7.2.2 Cerebrovascular estimates 148
7.3 Discussion 151

8 Conclusions and Future Work **153**
8.1 Conclusions 153
8.2 Future Work 155

IV Appendices and Bibliography **159**

Appendices **161**

A Cerebral Venous System and Starling Resistor Model **161**
A.1 The Starling Resistor Model 161
A.2 Collapsibility of Cerebral Venous System 164

B Validation of Estimation Algorithm Using Simulated Data **165**
B.1 Model Simulation for Data Synthesis 166
B.2 Analysis of Data for Estimation Results 166

C Other Parameter Estimation Approaches **171**

D Summary of Clinical Data and Estimation Performance **175**

E Correlation Coefficient Fails to Quantify Agreement **177**
E.1 Assessing Agreement Between Two Measurement Modalities 178
E.2 The Inadequacy of Correlation Analysis 180
E.3 Examples 181

Bibliography **187**

List of Figures

2-1 Intracranial space and CSF circulation [1]. 34

2-2 Human central nervous system [2]. 36

2-3 Blood supply to the brain: main arteries are shown in (a), and a view of the cerebral hemispheres is shown in (b). 37

2-4 Cerebro-venous system: the superficial veins [3]. 39

2-5 A graphical view of cerebrovascular autoregulation: steady-state CBF is maintained at the desired level of 45-50 ml min^{-1} $100g^{-1}$ tissue while MAP varies from about 60 mmHg to 150 mmHg. 41

2-6 An approximate graph for the CSF pressure-volume relationship. (Figure is adapted from [4].) 44

3-1 Various methodologies available for clinical monitoring of ICP; all of them require penetration of the skull and placement of a catheter or a sensor to measure ICP. (Figure is adapted from [5].) 52

4-1 A compartmental model of the cerebrovascular system by Sorek *et al.* [6]. The nominal pressure and flow values at different compartments are specified inside braces and parenthesis, respectively. 77

4-2 An elaborate model of the cerebrovascular system proposed by Ursino *et al.* [7], shown in the form of an electrical circuit. The variables labeled as G, C, P and q denote conductance, capacitance, voltage and current, respectively. The arrows indicate time-varying components to accommodate autoregulation. 78

4-3 An elaborate model of the cerebrovascular system proposed by Stevens *et al.* [8]. 79

4-4 A mechanical view of the cerebrovascular system in terms of pressures and flows [9]. 81

4-5 The Ursino-Lodi model of the cerebrovascular system, given in an electrical circuit form. 81

4-6 Typical autoregulation plateau observed from our implementation of the Ursino-Lodi model. For each value of the autoregulation gain, MAP was increased linearly over 20 minutes (quasi steady-state simulation) and the corresponding mean CBF was recorded. 84

4-7 Modified Ursino-Lodi model. 85

4-8 The modified Ursino-Lodi model was simulated to synthesize ABP, CBF, and ICP. Beat-to-beat averages (or means) of ABP (top), CBF (second row) and ICP (third row) are shown. The last window shows the perturbation $I_i(t)$ that causes sudden rises in ICP. A pulsatile ABP waveform is used as an input to drive the model, and the simulated CBF and ICP waveforms are recorded as model outputs. 86

4-9 Simulated ABP (top) and CBF (bottom) waveforms obtained from the modified Ursino-Lodi model. Figure highlights the intrabeat pulsatility in these signals. 87

4-10 Compartmental view of the intracranial space (adapted from [4]). Red arrows indicate circulation of CSF. 88

4-11 Our simplified model obtained from an aggregate mechanistic view of the intracranial space. By exploiting some key physiological features, the computational model provides a dynamic relationship between ICP and the measurable quantities [10]. 90

5-1 Graphical description of the idea for compliance estimation: when arterial blood pressure has a steep gradient, capacitance (or compliance) offers the smallest-impedance path for the current (or flow) $q(t)$, storing charge (volume) on C. The points marked as t_{b} and t_{s} correspond to the 'begin' and 'stop' times of the diastolic-to-systolic transition of ABP within the indicated beat, and the stored volume is equal to the area under the flow over this interval. 97

5-2 Radial ABP (blue, top) and CBFV at the MCA (red, bottom) recordings shown over a period of almost two cardiac beats. ABP is measured in units of mmHg and CBFV in cm/s. 101

5-3 A method for the phase-offset estimation: various candidate phase-offsets are applied until a linear model well approximates the relation between CBFV and the shifted ABP (at the selected low-$\frac{dp_{\mathrm{a}}(t)}{dt}$ points in a cardiac cycle). The left panel shows the case of an offset for which a linear model has a large residual error, while the right panel shows the case of an offset for which a line is a good fit to the data. 108

5-4 A flow-chart description of the estimation algorithm and pre-processing steps. An optional step of low-pass filtering the input waveforms is added in cases where significant high-frequency noise is present. . . . 109

6-1 Comparison of nICP (red) and the invasively measured ICP (blue) in three patients. The left panel in each case shows beat-by-beat ICP and nICP; the right panel shows the corresponding Bland-Altman plot, to assess agreement between the two methods. 119

6-2 For clinical monitoring, an ICP estimate every 50-100 beats sufficiently meets the clinical monitoring needs. The comparison in this figure plots ICP (blue) and nICP (red) only every 60 beats. The left panels show ICP and nICP. The right panels show the corresponding Bland-Altman plots to assess the level of agreement between the two methods. . . . 121

6-3 Examples representing two extreme cases of estimation performance, comparing nICP (red) and the invasively measured ICP (blue). The top row shows a case of poor estimation performance. The bottom row presents a case of very good ICP estimation, which picks up even small variations in the underlying ICP as well as tracking the baseline ICP. The left panels show beat-by-beat ICP and nICP. The right panels show Bland-Altman plots to assess agreement between the two methods. 123

6-4 Bland-Altman plot of all 3,529 independently obtained estimates, each over a distinct 60-beat window. The bias is 2 mmHg, and standard deviation of error is 9 mmHg. 124

6-5 Bland-Altman plot of 10-point average of independent estimates, providing one comparison for each 600-beat window, hence 353 points total. The bias is 2 mmHg, and standard deviation of error is 8.2 mmHg. 125

6-6 Bland-Altman plot of error between respective time-averages of measured ICP and nICP estimates; the bias is 1.8 mmHg and standard deviation of error is 6.8 mmHg. 126

6-7 Cumulative distribution of number of independent estimates as a function of absolute estimation error |nICP − ICP|. About 80% estimates have an absolute error less than 10 mmHg. However, requiring nICP estimates to be independent is unnecessarily stringent; see text for detail. 126

6-8 A linear model between average ICP and the estimation error has poor predictive value, as $R^2 = 0.032$ and the slope of the least-squares line is -0.09. 128

6-9 Exploring correlation between ICP estimation error and MAP: the scatter plot and best linear fit of the data indicate that error has no significant relationship with MAP. 128

6-10 Exploring correlation between ICP estimation error and mean CBFV: the scatter plot and best linear fit of the data indicate that error has no significant relationship with mean CBFV. 129

6-11 Left (blue) and right (red) nICP estimates obtained from the bilateral TCD measurements: estimates from the two sides generally agree within a close range. The invasively measured ICP (green) is also shown as a reference. 130

6-12 Signal quality of the recorded ABP (blue) and CBFV (red) waveforms varied across patient data. Both sampling frequency and amplitude resolution have a significant effect on the intrabeat analysis performed in our estimation algorithm. 134

7-1 Cerebral autoregulation in action, as revealed by concomitant variations in CPP (actual) and R: while CPP falls by more than 30 mmHg, between 100 and 360 seconds, (mean) CBFV is remarkably maintained about its baseline (about 37 cm/s), which is explained by the accompanying drop in resistance. After CPP falls below 60 mmHg, CBFV also starts to drop. 142

7-2 Time scale of autoregulation: the estimate of R has a fast response to variations in CPP, particularly in the most active region of autoregulation, CPP $>$ 60 mmHg. 143

7-3 An assessment of autoregulation can be made by combining measurements of mean CBFV and estimated CPP and resistance. An example of a patient record is shown. 145

7-4 Characterization of autoregulation based on MAP alone, rather than CPP, can lead to erroneous conclusions (see text for a detailed discussion). 146

7-5 Comparing MAP and mean CBFV measurements along with the ICP, resistance and compliance estimates for stroke (left column) and control (right column) cases. Mean CBFV and the estimates are shown for both the left and right hemispheres, in blue and red respectively. The dashed markers indicate the intervals of the various interventions. 149

8-1 An example of very striking estimation performance, particularly because no invasive measurement was used to train or calibrate the estimation method. Estimation performances like these point to the promise of our model-based patient-specific approach. 157

A-1 Flow through a collapsible tube: P_1 and P_2 are the upstream and downstream pressures, respectively, and P_e is the external pressure. Flow is denoted by Q. 162

A-2 Behavior of the Starling resistor model. The heavy black line corresponds to flow in the uncollapsed state, with $Q = (P_1 - P_2)/R)$. Different external pressure conditions lead to collapse of the tube at different values of P_2, causing different net flow in each case. 163

A-3 Pressure-flow relationships for a more realistic representation of collapsible tubes than the Starling model. 164

B-1 Simulation data set 1: cycle-averaged ABP, CBF, and q_1 (flow through R_a) obtained by simulating the modified Ursino-Lodi model are shown (top to bottom). 167

B-2 Estimation performance: beat-by-beat values of C, R and ICP are shown, where the blue (dashed) lines correspond to the simulated values in the Ursino-Lodi model, and the estimates are shown in red (solid) lines. 167

B-3 Simulation data set 2: cycle-averaged ABP, CBF, and q_1 (flow through R_a) generated by simulating the modified Ursino-Lodi model are shown (top to bottom). 168

B-4 Estimation performance: beat-by-beat values of C, R and ICP are shown, where the blue (dashed) lines correspond to the simulated values in the Ursino-Lodi model, and the estimates are shown in red (solid) lines. 169

E-1 Waveform comparison of non-invasive ICP estimate (red) against invasive ICP (blue) for Example 1. 182
E-2 A Bland-Altman plot and a histogram of error for the nICP estimate and invasive measurement of ICP in Example 1. 183
E-3 Waveform comparison of non-invasive ICP estimate (red) against invasive ICP (blue) for Example 2. 184
E-4 A Bland-Altman plot and a histogram of error for the nICP estimate and invasive measurement of ICP in Example 2. 184
E-5 Two examples to show how the correlation coefficient R completely fails to quantify agreement between two methods of assessing a common quantity. 185

List of Tables

D.1 A record-by-record summary of clinical data and the ICP estimation error in all 45 patient records. 176

Chapter 1

Introduction

1.1 Background

Blood is responsible for carrying oxygen and nutrients to tissue throughout the body, and taking away metabolic waste products. Most organs can survive a short interruption in their blood supply. Skeletal muscle, for example, can survive a disruption of blood flow for minutes. Brain tissue, however, cannot withstand ischemic conditions: neurological symptoms appear within seconds, and if ischemic conditions prevail for a few minutes, there is a high risk of irreversible damage to brain function [1].

Even though the brain accounts for only around 2% of total body weight, it accounts for almost 20% of the body's oxygen demand under resting conditions [1]. The stringent constraint of meeting the brain's blood supply requirements is primarily achieved by sophisticated local regulatory mechanisms to control blood flow, referred to in aggregate as *cerebrovascular (or cerebral) autoregulation.* (Mean arterial blood pressure, by contrast, is fairly uniform throughout the body, and not controlled locally.) To maintain the desired local blood supply, the cerebral vasculature has the innate ability to adapt to pressure, flow and metabolic changes by altering the diameters of the blood vessels to achieve vasoconstriction or vasodilation, and by altering the compliance of the arteries.

A key factor in determining perfusion to the brain is *intracranial pressure* (ICP), which is the pressure of the cerebrospinal fluid (CSF) that bathes the brain tissue

and spinal canal. While ICP is a pulsatile waveform, in the context of this document we will use the acronym ICP to denote the mean (or beat-averaged) value of the waveform. Particular references to instantaneous values or morphological features of the underlying waveform will be made clear.

ICP affects cerebral perfusion through the Starling resistor mechanism [11, 12] acting at the level of the cerebral veins: since ICP is usually higher than the far-end venous pressure, it collapses the veins and thereby acts as the effective downstream pressure [13, 14]. Thus, mean blood flow through the cerebral vasculature is determined by the difference between mean arterial blood pressure (MAP) and ICP, rather than between MAP and venous pressure. This difference, MAP − ICP, is therefore termed cerebral perfusion pressure (CPP). An increase in ICP, for instance in brain injury, causes CPP to drop, which is initially compensated by alterations in the cerebrovascular resistance through cerebral autoregulation, as long as the autoregulatory reserve is not exhausted, to maintain a steady cerebral blood flow (CBF). However, a continued rise in ICP, and thus drop in CPP, can outrun the cerebral vasculature's autoregulatory capacity, causing CBF to drop, and hence compromising oxygen supply to the brain. Cerebral autoregulation in humans maintains a steady blood flow in the face of CPP variations, caused by variations in either MAP and ICP or both. The typical range of operation of autoregulation is specified in terms of MAP, with lower and upper limits of autoregulation at about 60 mmHg and 150 mmHg, respectively [1].

ICP is normally 7-15 mmHg in the supine position in adults, but it is elevated in brain injury. An ICP above 20-25 mmHg sustained for a period of even a few minutes can be dangerous and requires immediate intervention to bring it back to normal [15,16]. It is also important to maintain a steady CPP of at least 60-70 mmHg to avoid brain ischemia that may result from damage to, or exhaustion of, cerebral autoregulation [17–20]. Elevated ICP signals compression of the neural tissue, and a continued increase can ultimately lead to sudden death. For example, in severe traumatic brain injury (TBI), brain swelling leads to increased ICP and consequent obstruction of blood vessels, causing hypoxic and hypercapnic conditions [21], and can have fatal consequences [15, 22, 23]. In the case of intracranial hemorrhage, bleeding

into the cranial cavity can cause the intracranial volume to increase, thereby causing ICP to rise dramatically, leading to a reduction in CPP and consequently poor cerebral tissue perfusion. ICP is elevated by brain tumors and in hydrocephalus (literally 'water on the brain', a condition with an abnormally high CSF volume). Accumulation of CSF in the cerebrospinal space is sometimes caused by vascular disease that affects intracranial compliance or blocks the absorption of CSF into the cerebral veins.

In ischemic strokes, blockage of an artery by a clot interrupts or stops blood supply to some brain tissue, and in many cases cerebrovascular autoregulation is partly or completely lost [24]. Disease of the cerebral arteries may also impair cerebrovascular autoregulation. It is also hypothesized that very premature neonates lack a fully developed cerebral autoregulation mechanism, hence cannot buffer cerebral blood flow under changing perfusion pressure or metabolic needs [25, 26].

1.2 Motivation

The primary aim of critical care for patients suffering from brain injury or cerebrovascular disease is to closely monitor the patient state and provide appropriate therapeutic intervention. A key component of such monitoring involves continuously tracking ICP and the state of cerebral autoregulation [17,20,27,28]. However, current methods for direct measurement of ICP are highly invasive, as they require neurosurgical penetration of the skull to place a pressure sensor, and carry risks of tissue damage and infection [29]. They are, therefore, not part of routine clinical procedures in this broad patient population and are applied only in the sickest cases. Thus, there is a clear and compelling need for developing procedures to monitor and track ICP and cerebrovascular autoregulation as a function of time with minimal invasiveness.

A method for minimally- or non-invasive monitoring of ICP would be a seminal improvement in the diagnosis and treatment of brain trauma and neurological diseases. It will open up the possibility for use in several settings where ICP monitoring would improve care, but is currently avoided because of the highly invasive nature of available methods. For instance, non-invasive monitoring of ICP will have

impact on diagnosis and monitoring of the early non-symptomatic stages of TBI, in mild and moderate TBI, as well as for repetitive concussions (e.g., sports injury), hydrocephalus, brain tumor, stroke, post-neurosurgical care, or even in abnormal eye exams. Another potential application is the monitoring and programming of CSF shunts in chronic hydrocephalus patients. Non-invasive monitoring of ICP could also be informative in a still broader population in which elevated ICP may be involved in specific pathophysiological pathways, possibly even in such common conditions as migraine. The technology could well eventually replace the invasive procedures that are currently employed, saving patients from the risks and complications associated with current measurement modalities.

Estimation of ICP will make CPP available, which can then be used along with the estimates of the resistance and compliance properties of the vasculature to quantify the state of autoregulation. This will enable rational assessment and better treatment. Current methods of autoregulation assessment are mostly within the realm of research, are based on indirect indicators and correlations rather than directly on the physiology; there is no commonly accepted method of clinical assessment of autoregulation [30]. A physiologically based assessment of autoregulation is expected to meet greater clinical acceptance, because it will enhance the understanding of the functioning of the cerebral vasculature and can potentially lead to guided therapeutic interventions.

1.3 Approach

We adopt a *model-based* approach to develop methods for non-invasive and continuous monitoring of ICP and autoregulation. We develop a reduced-order mathematical model that is rooted in fundamental cerebrovascular physiology, and that represents the relationships among the essential physiological variables involved in cerebrovascular dynamics. The model then provides dynamic constraints for processing of clinically accessible non-invasive measurements to obtain continuous estimates of the unmeasured variables of interest. Our simplified mechanistic model of the relevant

cerebrovascular physiology is critical to the development in this work, so we provide below a brief overview of mathematical modeling approaches for the cerebrovascular system, and discuss what distinguishes our development from others.

The understanding of cerebrovascular physiology has been captured in the literature in the form of various mathematical representations, or models, at different levels of detail [31]. These models relate blood pressures and flows in various segments of the cerebral vasculature, as well as pressures and flows of CSF in the intracranial space. These representations are helpful in understanding system behavior, as they can mimic the actual human physiology in ever greater detail, and are the basis for further study of pathological scenarios and exploration of desired therapeutic interventions. However, most of these models are too large and complex to be suitable for use in real-time clinical inference. They contain dozens of unknown parameters, which are difficult to identify robustly from a few measurable quantities, such as arterial blood pressure (ABP) and CBF. Therefore, the use of physiologically-based mathematical models has been limited to computer simulations for academic illustrations and exploratory studies.

Statistical and machine-learning type approaches for estimating and then using empirical relationships among the desired cerebrovascular quantities have been reported [32–34], as we discuss in detail later in this document. These modeling approaches rely on empirically learning relationships among the physiological variable of interest (e.g., ICP) and observable data (e.g., ABP, CBF), and training on relevant population data. Generally, the models in this category are partially or completely blind to the physiological dynamics that govern these variables. Even though useful relationships may be extracted by these models, the richness of the cerebrovascular system, particularly under various pathologies as well as in patient-specific situations, means that there is a significant penalty to be paid for not taking account of what is known of the underlying physiological mechanisms and processes.

We believe that simple but physiologically-based models of the cerebrovascular system can be developed. Such models would be aimed at overcoming the disadvantages of each of the two categories above: models in the first category are physiologically

meaningful but complex; models in the second category may be simpler but lack a physiological foundation and interpretation. Models of the type we are aiming at need to be well-suited for integrating and interpreting clinical data and allowing one to infer physiological variables of interest in patient monitoring. We are also motivated and inspired by the success of similar model-based efforts in other physiological systems, such as cardiovascular, respiratory, and renal physiology. A very pertinent example, for what we aim to obtain and use for cerebrovascular monitoring, is the Windkessel model (and its several variants) for the cardiovascular system [35, 36]. It is a simple two- or three-element model that elegantly represents the system-level dynamics, relating ABP and cardiac output through peripheral resistance and arterial compliance. The Windkessel model has been extensively used to study and illustrate cardiovascular dynamics, as well as for application in patient monitoring [37].

In this thesis we make key observations about cerebrovascular physiology and use model-reduction ideas to obtain a simple mathematical model of cerebrovascular dynamics. We validate the reduced model via simulation against a well-established (but more elaborate) model of the cerebrovascular system. Based on our reduced model, we develop algorithms for combining clinical measurement waveforms of peripheral ABP and cerebral blood flow velocity (CBFV), obtained via transcranial Doppler (TCD), to provide continuous estimates of ICP and cerebrovascular resistance and compliance.

1.4 Thesis Contributions

The work in this thesis has four major contributions.

- We develop a simple and physiologically-based mathematical model of cerebrovascular dynamics, aimed at the task of ICP monitoring. The model represents essential cerebrovascular dynamics with minimal complexity, as it has only three unknown parameters.

- We develop a *calibration-free* and *patient-specific* method for *non-invasive* and

continuous estimation of the model parameters, including ICP (and hence CPP), that can be performed in real-time. No training on population data is involved. The algorithm interprets clinical measurements of radial ABP and CBFV, extracting the intrabeat features of the time-synchronized waveforms, and uses the constraints provided by our model to obtain robust estimates. The model-based intrabeat analysis of TCD waveforms, time-synchronized with ABP, is a novel feature of our approach.

- We validate our ICP estimates by comparing against invasively obtained measurements of ICP in 45 patients, a total of more than 150,000 beats, and more than 3,500 independent estimates. The ICP estimates track measured ICP closely over a range of dynamic variations. Comparison of aggregate mean ICP for each record, i.e., time-averaged over an entire patient record, yields a bias of 1.8 mmHg and a standard deviation of error of about 6 mmHg. Comparison of all independent estimates yields a mean estimation error (bias) of less than 2 mmHg and a standard deviation of error of about 8 mmHg. The standard deviation of error across all patient records is about 6 mmHg. These error statistics are not yet within the 4-5 mmHg error tolerance that would be a worthwhile practical goal, but are still comparable to some of the current invasive methodologies for ICP measurement. Estimation performance is expected to improve by upgrading the data acquisition for a higher signal quality of the input measurements, better noise and artifact elimination strategies, and possibly further refinements of the pre-processing algorithms.

- The method provides beat-by-beat estimates of cerebrovascular resistance, compliance and CPP. Temporal profiles of resistance and compliance estimates, possibly independent estimates for the left and right hemispheres, along with measurements of CBFV, reveal much about the state of the cerebral vasculature. Appropriate variations in the resistance, or a lack thereof, in response to abrupt changes in CPP can be used to form a non-invasive and continuous assessment of cerebral autoregulation. The approach has two key advantages over

the majority of current indices: the assessment is based on CPP (rather than MAP alone), and it is derived from a physiologically-based model. Preliminary results are encouraging enough to suggest that further analysis and validation are warranted.

1.5 Organization of Thesis

The thesis is organized as follows. The first section, titled *Cerebrovascular Physiology and Neuro-critical Monitoring*, comprises the next two chapters and provides background on cerebrovascular physiology and monitoring in neuro-critical care. The importance of ICP monitoring, its current measurement methodologies, and need for a non-invasive method of ICP estimation are discussed. The section also provides an overview of cerebral autoregulation and its assessment.

The second section of the thesis, *Mathematical Models and ICP Estimation*, deals with mathematical modeling of the cerebrovascular system, and approaches for non-invasive estimation of ICP. Chapter 4 summarizes various mathematical models of the cerebrovascular system that have been proposed and studied in the last four decades. It then presents and develops our reduced-order model. In Chapter 5, we describe parameter estimation algorithms for our cerebrovascular model.

The third section of the thesis, *Validation and Performance Analysis*, contains estimation results and validation of our ICP estimates against invasive measurements in a pool of severe traumatic brain injury patients (Chapter 6). Finally, in Chapter 7, we discuss a few case studies related to assessment of cerebral autoregulation, which indicate the potential for forming an index that can be used in clinical settings. However, much of this autoregulation work remains for future exploration and validation. Chapter 8 summarizes and concludes the thesis.

Part I

Cerebrovascular Physiology and Neuro-critical Monitoring

Chapter 2

Cerebrovascular Physiology and Brain Injury

In this chapter we provide a very brief overview of the relevant anatomy and physiology of the cerebrovascular and cerebrospinal systems, and the pathophysiology of brain injury. This overview will be helpful in understanding the peculiarities of this physiological system and the problem of cerebrovascular monitoring. Physiological understanding will be particularly useful in the development of various mathematical models that we will discuss in Chapter 4. In Section 2.1, we describe the details of the brain tissue, cerebral vasculature, and cerebrospinal fluid spaces. Section 2.2 gives an outline of the epidemiology of brain injury. Finally, Section 2.3 provides details on cerebral edema and other pathophysiological conditions following TBI, which is one of the main settings in which ICP monitoring is indicated.

2.1 Physiology

The brain is a soft tissue enclosed inside the rigid skull and bathed by CSF. The volume of the cranial cavity is taken up by three distinct components: the brain tissue, the cerebral vascular network, and the CSF spaces. Figure 2-1 shows a view of the intracranial space and CSF circulation pathways. Since, to a first approximation, the skull is a closed system, expansion of one component must therefore be accompanied

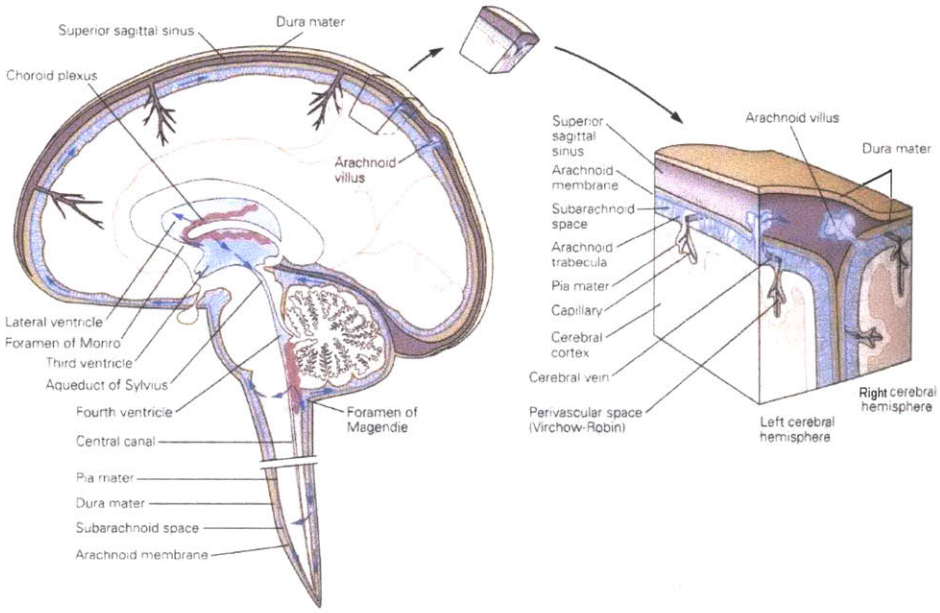

Figure 2-1: Intracranial space and CSF circulation [1].

by compression of one or both of the other two. This is termed the Monro-Kellie doctrine [38–40]. As we will detail in Section 2.3, such compression has direct adverse functional consequences. In the following, we provide an overview of each of the three constituents of the cranial cavity.

2.1.1 Brain tissue

As shown in Figure 2-1, the brain tissue is surrounded by three layers of connective tissue. The *dura mater* is the outermost membrane of the three, and is attached directly underneath the skull. The arachnoid membrane, the second layer, separates the *dura mater* and the subarachnoid space, which is bounded internally by the third membrane, *pia mater*. The cerebral cortex which is the outermost layer of the brain, lies beneath and in direct contact with the *pia mater*.

The brain consists of four major anatomical divisions: the brain stem, the diencephalon, the cerebellum, and the left and right cerebral hemispheres (also collectively called the telencephelon). Figure 2-2 shows the detailed anatomical structure of the brain. The brain stem consists of the medulla, pons, and the midbrain. It is an

extremely important part of the brain because the nerve connections of the major sensory and motor systems from the brain to the rest of the body pass through the brain stem. It also plays an important role in the regulation of the central nervous system, cardiac and respiratory function, and sleep cycle.

The diencephalon is part of the forebrain, and comprises the thalamus, hypothalamus, and posterior portion of the pituitary gland. The cerebellum is a separate structure, a tightly folded and crumpled layer of cortex, attached to the posterior-inferior surface of the brain. It has an important role in motor control, motor learning and possibly cognitive function. Above the cerebellum are the left and right hemispheres, which make up the bulk of the brain and consist of an outer layer of grey matter (cell bodies) and an inner layer of white matter (the axonal connections). Various parts of the two hemispheres are commonly labeled as lobes (the frontal, parietal and occipital lobes are marked in Figure 2-2). The spinal cord extends from the base of the skull down to the first lumbar vertebra.

The human nervous system comprises two parts: the central nervous system (CNS), and the peripheral nervous system (PNS). The CNS consists of the brain and the spinal cord; the PNS includes sensory receptors, nerves, and ganglia outside the CNS. Neural activity is the result of a close communication between the CNS and the PNS. The spinal cord has 31 pairs of spinal nerves that are used to collect sensory information from the peripheral organs such as muscle, joint, skin, and visceral organs, and to send motor information from the spinal cord to the periphery. There are ascending and descending pathways (i.e., a series of neurons and synaptic relays) within the spinal cord for the purpose of carrying information to and from the higher levels of the CNS, where the information-processing unit — the brain — lies. Different parts of the brain perform specific neuro-cognitive functions, including processing sensory information (vision, hearing, etc.), motor control (limb movement, speech, etc.), learning, and memory. A lot more detail is known about each part of the brain and its specific functional role; however, we do not go into this because it is not directly relevant to the development in this work.

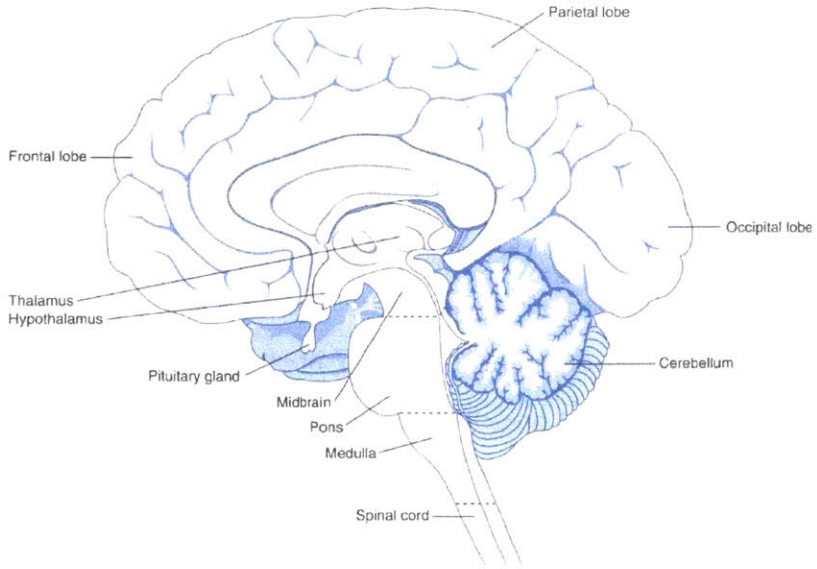

Figure 2-2: Human central nervous system [2].

2.1.2 Cerebrovascular physiology

The second constituent of the cranial space is the vascular network that supplies oxygen, glucose and nutrients to the brain, and removes CO_2, lactic acid and other metabolic waste products. The consumption of oxygen and glucose depends on the local cerebral activity level. In normal conditions, CBF is 45-50 ml min^{-1} $100g^{-1}$ tissue, and is about 3 to 4 times higher in the grey matter than in the white matter. Physiological electrical function of the neural cells begins to fail if CBF drops below 18-20 ml min^{-1} $100g^{-1}$ tissue [4]. The blood circulation within the brain is accomplished through a network of cerebral arteries, arterioles, capillaries, and veins. We describe these components next.

Cerebro-arterial system

Figure 2-3(a) shows a view of the main arteries originating from the aortic arch and carrying blood to the cerebral region. A pair of internal carotid arteries arises from the common carotid arteries, and together this pair is responsible for supplying almost 80% of cerebral blood flow (CBF). Another pair of arteries, called the vertebral arteries, originates from the right and left subclavian arteries, travel upwards along

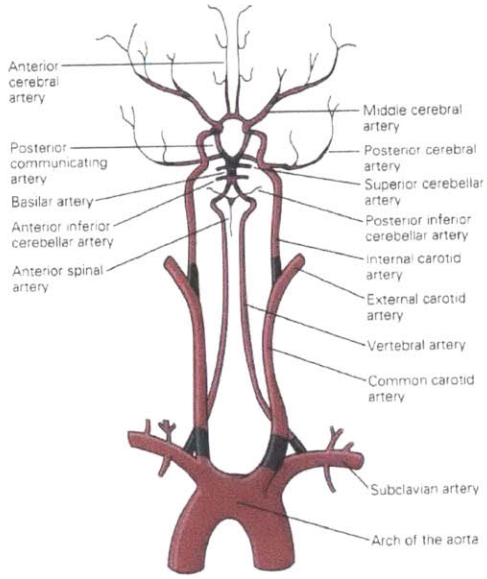

(a) Cerebral blood circulation: main arteries [1].

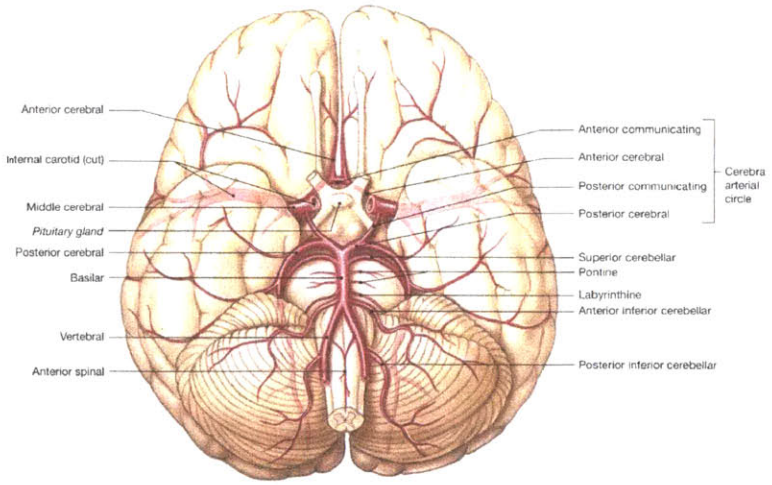

(b) Arteries of the brain (inferior view): detailed view in the cerebral hemispheres. [41].

Figure 2-3: Blood supply to the brain: main arteries are shown in (a), and a view of the cerebral hemispheres is shown in (b).

the vertebral column, enter the skull through the *foramen magnum*, and fuse to become the basilar artery. Together, the basilar and internal carotids form a ring-like structure at the base of the brain, called the Circle of Willis, shown in Figure 2-3(b). Three main arteries branch out from the left and right sides of the Circle of Willis to supply the corresponding cerebral hemispheres. They are the middle cerebral artery (MCA), the anterior cerebral artery (ACA), and the posterior cerebral artery (PCA), shown in Figure 2-3(b). The right and left MCAs can be seen prominently on each hemisphere in Figure 2-3(b).

The MCA is responsible for the majority of the blood supply in each hemisphere. It feeds the bulk of the lateral surface of the hemisphere, except for the superior aspect of the parietal lobe, which is supplied by the ACA, and the inferior part of the temporal lobe. It also covers the latero-inferior frontal lobe and lateral temporal lobe. The ACA supplies the medial surface of the frontal lobe and parietal lobes, the olfactory bulb and tract, and the anterior aspect of the base of the brain. Finally, the PCA supplies blood to the posterior aspect of the brain, namely the occipital lobe. These main arteries branch into smaller arteries and arterioles, which further subdivide to capillaries where most of the oxygen and nutrients are exchanged. An exclusive property of those capillaries inside the brain ventricles (to be discussed in the next subsection) is that their epithelial walls allow the water and ions to escape from the plasma, albeit mediated by the blood-brain-barrier, to constitute CSF [42].

Cerebro-venous system

The capillaries combine downstream into relatively larger blood vessels of the cerebral venous system. For organization purposes, the cerebral venous system can be divided into a superficial and a deep system. The superficial system comprises the sagittal sinuses and cortical veins; they drain blood from superficial surfaces of both cerebral hemispheres. The deep system comprises the lateral sinus, the straight sinus, and the sigmoid sinus; they drain blood from the deeper cortical veins. The blood in both of these systems mostly drains into the internal jugular veins. Figure 2-4 shows important superficial veins in the system. The superior sagittal sinus (a superficial vein)

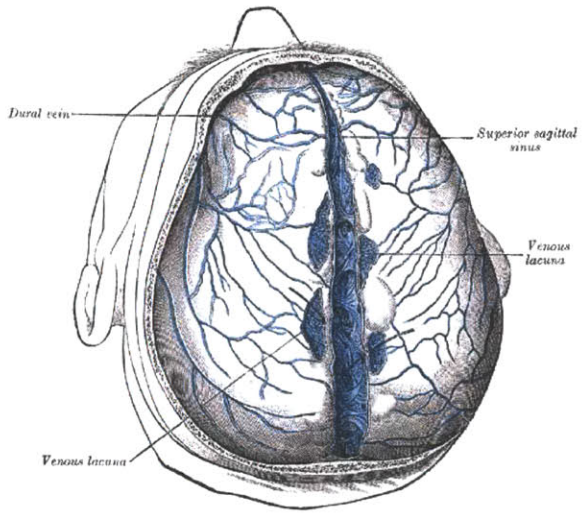

Figure 2-4: Cerebro-venous system: the superficial veins [3].

is located around the middle of the two hemispheres. Venous lacunae are located on each side of the superior sagittal sinus. For cerebrovascular dynamics, we do not need to delve into the details of the inherently complex, three-dimensional network of cerebral veins, but we want to underline two aspects of it. Firstly, the veins draining blood from the brain do not follow the same course as the arteries that supply them. Generally, venous blood drains to the nearest venous sinus. However, in the case of the deepest structures, blood first drains into the deep veins, and from there into the venous sinuses [43]. Secondly, cerebral veins are collapsible vessels, and the pressure of the blood inside is lower than the external pressure, namely ICP, acting on them. The physiological consequences of this second observation are described next.

Starling mechanism and cerebral perfusion pressure

Since ICP is typically higher than the cerebral venous pressure, and the cerebral veins are collapsible vessels, ICP becomes a key determinant of cerebral blood flow through the cerebral vasculature. More specifically, ICP acts as external pressure to the blood vessels, and at the level of the cerebral veins this external pressure (7-15 mmHg normally, in the supine position) exceeds the internal luminal pressure in the large cerebral veins (around 5 mmHg) [13, 14]. Smaller cerebral veins join in to

larger cerebral veins, which then ultimately connect to the venous sinuses. The mean luminal capillary pressure is normally about 30 mmHg, which decreases along the flow in the venous system, reduces to less than 10 mmHg in the large veins, and is only about 5 mmHg in the venous sinuses. The collapse occurs at the large cerebral veins, as they are like flexible tubes, while the venous sinuses do not collapse due to the rigidity of their walls [13]. ICP thus causes the veins to collapse, and effectively acts as the downstream pressure for blood flow through the cerebral vasculature [14]. This phenomenon is reminiscent of a Starling resistor [11, 12], whose operation we summarize in Appendix A.

For a constant cerebrovascular resistance (as would be the case over a time that is shorter than autoregulation time scales), CBF is proportional to the difference of MAP and ICP, i.e., proportional to what was defined as CPP. Therefore, it is critical to monitor CPP, not just MAP, in patients with cerebrovascular injury or disease. Medical guidelines require CPP to be above 60-70 mmHg to maintain the desired CBF and avoid inadequate cerebral perfusion [16, 20], though optimal thresholds for CPP are not fully established [17,44]. As noted earlier, variations in CPP are compensated by variations in cerebrovascular resistance, the primary mechanism for autoregulation. We discuss this in detail next.

Cerebrovascular autoregulation

As briefly mentioned in the introduction, the cerebral vasculature has an innate ability to maintain a close match between the demand for and supply of oxygen to the brain tissue. Cerebral arteries and arterioles respond to changes in CPP (due to changes in MAP or ICP or both) by varying their diameters, thus altering the resistance to blood flow. If the pressure drops, these vessels dilate to reduce their resistance to flow and maintain enough CBF to protect the brain tissue against hypoxic-ischemic conditions; conversely, during hypertension, they constrict to raise resistance (and also protect against edema). This sophisticated control mechanism is at the core of cerebral autoregulation, which is normally responsible for maintaining a steady CBF for CPP variations over a range of about 90-100 mmHg in humans [1, 4].

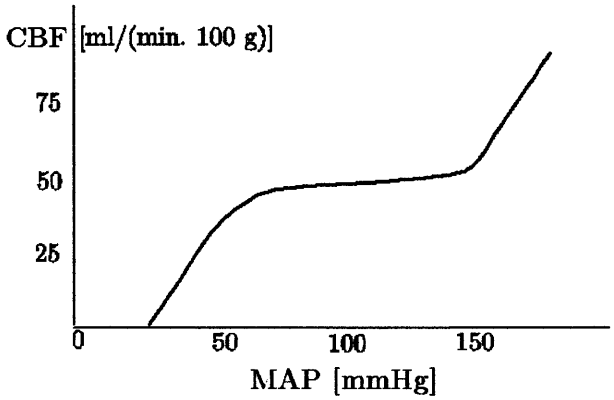

Figure 2-5: A graphical view of cerebrovascular autoregulation: steady-state CBF is maintained at the desired level of 45-50 ml min^{-1} $100g^{-1}$ tissue while MAP varies from about 60 mmHg to 150 mmHg.

Figure 2-5 shows a graphical view of autoregulation. Steady-state CBF is constant as MAP varies over a wide range. (It is customary to state autoregulation in terms of MAP only, perhaps assuming a constant, normal ICP. However, it is CPP that drives flow through the vasculature, and ICP interacts with autoregulation [30].) Outside of this regulatory range, i.e., in extreme hypotensive or hypertensive situations, or when an abnormally high ICP leads to extremely low CPP, CBF varies almost linearly with pressure. In normal circumstances, CPP is between 70 and 100 mmHg, and the vasculature operates around the central, flat part of the autoregulation range.

The diameter variations in the arteries and arterioles are caused by the action of smooth muscle cells inside these vessel walls. It is believed that the arterial smooth muscle responds to changes in the transmural pressure, CBF, oxygen content in the blood, cerebral metabolic rate, neural stimuli, and possibly even other factors [45]. However, the relative contributions of these various mechanisms to cerebrovascular autoregulation are incompletely understood and might be dependent on the particular stimulus. One of the primary modes of action is thought to be mediated by changes in transmural pressure that trigger the release of vasoactive substances from the endothelium and peri-adventitial nerves, which then modulate changes in vascular smooth muscle tone and alter the vessel diameters [45]. *In vitro* experiments confirmed that the arterial diameter starts to change within a few seconds of pressure

perturbations and completes a response in about 15-30 seconds. Similarly, metabolic regulation is mediated by changing concentrations in K^+ and H^+ ions, which in turn are thought to affect the arterial smooth muscle and cause relaxation or contraction. The details of this pathway are still being actively investigated.

2.1.3 Cerebrospinal physiology

Figure 2-1 shows a set of connected spaces, the cerebral ventricles, that communicate with each other, with the subarachnoid spaces, and with the spinal canal. A clear water-like fluid resides in all these spaces. It is, therefore, appropriately called the cerebrospinal fluid (CSF). CSF is secreted at the boundary of the lateral ventricles by a specialized capillary network, the choroid plexus, shown in Figure 2-1. CSF flows from the lateral ventricles, through the inter-ventricular foramina of Monro, into the third ventricle, as shown by arrows in Figure 2-1. From here it flows into the fourth ventricle through the cerebral aqueduct of Sylvius and then into the subarachnoid space through the foramina of Magendie and Luschka. Within the subarachnoid space, CSF flows down the spinal canal and also upward over the convexity of the brain into the subarachnoid space, where it is reabsorbed in the venous system through granules called arachnoid villi.

Equal rates of formation and reabsorption in steady-state maintain a constant CSF volume [42, 46]. The total CSF volume has not been measured accurately but is estimated to be between 140 ml and 250 ml. It gets replenished about three to four times during the course of 24 hours [47], which amounts to a rate of formation/reabsorption of less than 0.1 ml per minute. As can be noticed from the respective volumetric flow rates of CSF and blood (which is about 1000 ml per minute in a normal adult [48]), the formation and reabsorption pathways for CSF have much higher resistance than that of the cerebral blood vessels. These disparate flow rates give rise to different time scales in the dynamics of the cerebrovascular system.

CSF has several functions. It provides buoyancy to the brain, reducing its effective weight and thus allowing it to float within the cranial vault without compressing the more caudal structures of the CNS. It also provides a mechanical cushion to protect

the brain from impact with the bony skull. The CSF does not come in direct contact with the neurons or the glial cells, due to the action of the blood-brain-barrier, however it plays an important role in the exchange of materials between the neural cells and the interstitial fluid, whose composition is critical to provide a constant, controlled environment for the brain cells, to protect it against neurotoxins, and to prevent escape of local neurotransmitters [2, 42]. The constituents of CSF and blood are carefully retained in their respective spaces by the blood-brain and blood-CSF barriers. Some components common to both CSF and blood are in almost the same concentration (Na^+, Cl^-, HCO_3^-), while others are found in higher concentration in either blood or CSF. ($[K^+]$ and glucose are higher in blood, while $[Mg^+]$ and creatine are higher in CSF [2].)

CSF pressure and volume relationship

The CSF pressure inside the ventricles, sometimes referred to in the literature as the ventricular fluid pressure (VFP), is considered the gold standard for ICP, and normally measures 7-15 mmHg for a supine adult. A practical assumption common to various models and monitoring methods is to take CSF pressure to be essentially uniform in the entire intracranial space, from the ventricles to the subarachnoid space and also into the spinal column. However, the flow of CSF through the cerebrospinal space requires a pressure gradient to overcome the resistance to flow along the pathway, and CSF pressure therefore becomes location-dependent, being higher at the brain ventricles and lower at the downstream end of CSF flow, e.g., in the subdural space. The pressure gradient and associated spatial variation of ICP is more pronounced when CSF flow is increased, as may arise when a lumbar puncture is performed to extract CSF in conditions such as 'normal pressure hydrocephalus' [49]. (The opening pressure on such a lumbar puncture, before flow is established, is thus more reflective of ICP.)

Due to its rigidity, the skull is assumed to be a fixed-volume compartment. There is very little compliance associated with the cranial cavity: the pressure may change inside the cranium but there is negligible change in volume of the total cranial con-

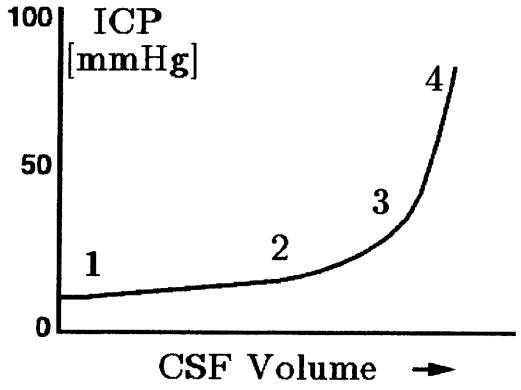

Figure 2-6: An approximate graph for the CSF pressure-volume relationship. (Figure is adapted from [4].)

tent. As summarized in the Monro-Kellie doctrine, any change in volume of one of the constituents of the cranial compartment must be compensated by an opposite change in volume of the others [38–40]. For example, if there is any increase in the volume of CSF, it causes a compression of the brain tissue and cerebral vasculature, with a concomitant increase in pressure due to the compliance of this combination of tissue and vasculature. Similarly, if the brain swells due to cerebral edema, ICP rises, possibly well above normal. The relationships between the CSF system and ICP have been studied in great detail, and a nonlinear pressure-volume relation between CSF volume and ICP is observed [50–52]. In animal experiments, this relationship is studied by injecting fluid into the brain ventricles and recording the corresponding steady-state increase in ICP. Figure 2-6 shows the response of ICP to changes in the CSF volume. Initially, for the part between Points 1 and 2, an increase in CSF volume causes very small change in ICP. However, the pressure-volume curve gets steeper at a higher CSF volume (between Points 2 and 3). At further increase in volume (between Points 3 and 4), ICP increases dramatically in response to a small injected volume. The possible causes of high ICP in clinical settings are discussed next.

Causes of elevated ICP

An ICP above 15 mmHg is termed intracranial hypertension, and immediate intervention is indicated for ICP above 20-25 mmHg [16], though precise guidelines depend

on the involved pathology. An elevated ICP is dangerous primarily because it affects cerebral perfusion and may lead to irreversible brain damage and fatal consequences. An increase of ICP above normal generally involves an increase in the volume of at least one major cerebral component. The following are a few major causes [53].

- Cerebral edema or brain swelling: In traumatic brain injury, the brain swells and occupies a larger space than usual, thus causing ICP to rise. In the absence of an external intervention, the edema can build up and lead to dangerously high ICP, well above the 15 mmHg threshold, with possibly fatal consequences.

- Increase of CSF volume: This happens when something blocks the normal drainage of CSF, for example slow absorption due to high sagittal pressure, or a disease causing increased formation or impaired reabsorption of CSF. Hydrocephalus is an example of excess CSF. The increase in CSF volume generally results in a higher ICP. The build-up in this case generally occurs over longer time periods than in cerebral edema.

- Hemorrhage: Bleeding inside the cranial cavity adds fluid volume, which raises the level of ICP. There are various types of hemorrhage, involving different pathophysiological mechanisms and response of the cerebral vasculature, so the exact dynamics of intracranial hypertension vary.

- Tumor lesions: Brain tumors take up space and hence cause an increase in ICP. A big enough lesion can, in fact, gradually shift the brain from its normal position.

Other causes of typically mild intracranial hypertension may also be observed. An increase in CO_2 content in the blood will make the cerebral vessels dilate, thus reducing space for CSF and increasing ICP [54]. Finally, Valsalva maneuvers, noxious stimuli, and seizure activity also cause ICP to rise, though usually well below the point of danger [53]. Below we discuss a few clinical interventions aimed at lowering an elevated ICP.

Treatment for elevated ICP

Immediate actions to bring ICP down include the following.

- Head elevation: Simply changing the head-of-bed angle of a patient can ameliorate intracranial hypertension somewhat [55]. In hyper-volemic conditions, a head-up tilt causes the fluid volume in the cerebral region to decrease, due to the top-down pressure gradient, leading to a small drop in ICP.

- Hyperventilation: The hypocapnic conditions induced by hyperventilation quickly lead to vasoconstriction of the cerebral arteries, creating more space for CSF and thus decreasing ICP [54].

- Hyperosmolar agents: Administration of hyperosmolar therapy is a common practice in the treatment of elevated ICP in traumatic injury to the head, and is usually more effective than hyperventilation [56]. Immediately after bolus administration of a hyperosmolar agent, such as mannitol or hypertonic saline, the circulating blood volume expands, blood viscosity decreases, and CBF and cerebral oxygen delivery increase. The action of an osmotic diuretic takes effect in about 15-30 minutes, when it sets up an osmotic gradient between the intravascular and the extravascular spaces, in the regions where the blood-brain-barrier is not damaged during the brain injury. This gradient causes water to be drawn out the interstitial fluid spaces into the capillaries, thus reducing the intracranial fluid volume. The reduction in volume leads to lowering of ICP [57].

- CSF drainage: Draining CSF through the brain ventricles reduces the CSF volume and thus lowers the ICP. The process is called ventriculostomy; it entails a hole to be drilled in the skull and an external ventricular drain or intraventricular catheter to be placed into the brain ventricles. A desired amount of fluid is extracted via the catheter to reduce the CSF volume and thus decrease ICP. (The same catheter may also be used for ICP monitoring, which we discuss in more detail in the next chapter.) In chronic hydrocephalus patients, in whom

CSF draining is required quite often to reduce the excess amount, CSF shunts are sometimes implanted inside the skull that drain fluid from the ventricles into a peritoneal cavity. (Detail on CSF shunts and their effectiveness can be found in [58].)

- Decompressive craniectomy: A part of the skull is removed, allowing the brain to swell outwardly, hence reducing ICP. After swelling subsides, the skull is closed again.

2.2 Epidemiology of Brain Injury

Stroke is a cerebrovascular accident that leads to severe consequences, including both life-long morbidity and mortality. According to the American Heart Association, about 780,000 Americans suffer a new or recurrent stroke each year [59]. Stroke is the cause of death in more than 150,000 people in the U.S. annually, and it is the third leading cause of death in the U.S., behind only heart disease and cancer; about one of every 16 deaths is due to stroke [59].

Traumatic brain injury (TBI) ranks among the top health-care challenges we face today, as it often results in persistent neurological and psychiatric morbidity and is associated with significant health-care expenditure. Annually about 420,000 Americans suffer a traumatic injury to the head, and about 50,000 deaths are attributed to such injuries each year; about 6 million Americans, or 2% of the population, live with the effects of TBI [60]. Diagnosis and management of these patients remains an elusive challenge even after decades of scientific and technological development.

Attention to TBI has increased recently, prompted in part by the large fraction of combat casualties from the wars in Iraq and Afghanistan, injuries in military and civilian populations alike caused by explosive blasts, and repetitive concussions in contact sports. In fact, TBI has been called the 'signature injury' of the Iraq War [61, 62], as Improvised Explosive Devices generate shock waves that cause traumatic injuries of various kinds and severity. Exposure to such blasts has been correlated with the development of post-traumatic stress disorder and psychological and neuro-cognitive

impairment, leading to life-long disability [60]. In sports, evidence suggests that repeated, mild injuries to the brain can lead over time to depression and other psychological and neuro-cognitive problems [63]. The realization is growing that TBI is not merely an event, but a process that has lasting effects on the central nervous system and other organ systems, and is associated with long-term mortality, disability and higher incidences of various neurological disorders [64].

In extremely premature neonates, hypoxic-ischemic and hemorrhagic brain injury are major causes of mortality and permanent disability [65]. Due to insufficiently developed blood vessels and immature cerebral autoregulation in these pre-term infants, bleeding into the peri-ventricular space damages fragile brain tissue, causing permanent and quite often severe loss of function. About 40-50% of children with cerebral palsy, for example, are survivors of pre-term birth [66]. Brain injury in prematurely born babies is a primary concern, and leads to long-term medical and social consequences [67].

2.3 Pathophysiology of Brain Injury

The pathophysiology of brain injury consists of the initial insult, generally termed as primary injury, and occurs over the time span of only a few milliseconds. The primary injury is commonly followed by a physiological response, possibly leading to secondary injury that ensues within minutes to hours and that tends to exacerbate the effects of the primary injury [68,69]. During the transition to secondary injury, cerebral edema can develop, which causes ICP to rise, possibly to critical levels, thereby decreasing CPP and potentially compromising blood flow to the brain. Decreased perfusion exacerbates the neurological deficit, which leads to further injury; the vicious cycle can ultimately lead to fatal consequences. The work by Miller *et al.* suggests that elevated ICP is responsible for the majority of deaths in severe TBI [15]. Mild and moderate TBI also pose serious concerns. Though their exact mechanisms are not fully understood, recent results from animal experiments demonstrate that ICP shows a dose-dependent increase even in response to low-intensity blast exposures at levels

commonly considered non-injurious [70]. A hemorrhagic stroke occurs when a blood vessel inside the cranium ruptures, cutting down blood supply to the arteries downstream and thus compromising perfusion to associated tissue. The blood spilling in the intracranial space causes ICP to increase, which leads to a drop in CPP, which may then lead to ischemia.

2.3.1 Cerebral edema

Cerebral edema is one of the most common consequences of TBI and ischemia. Unless an external control stops the cascade of events, it leads to raised ICP and may eventually lead to brain herniation. Development of cerebral edema contributes to brain swelling, and it is well established that this swelling causes ICP to increase. Increased ICP leads to obstruction of blood vessels, causing hypoxic and hypercapnic conditions, and increased ICP [21]. For this reason, cerebral edema remains a critical problem for which no effective solution has been identified.

Cerebral edema is classified into two types, defined on the basis of its cause: cytotoxic or vasogenic. In both cases, an abnormal situation arises in which plasma constituents and proteins leave the blood vessels (i.e., capillaries), enter the parenchyma, and finally spread into the cerebral interstitium. The spread is into white matter alone in the case of vasogenic edema, or into both white and grey matter in the case of cytotoxic edema. The fundamental cause of this abnormal transport of plasma is either the destruction of endothelial membranes due to brain injury, or some other pathology of the blood-brain-barrier [71]. The accumulation of plasma leads to the edematous situation. These transport processes are governed by osmotic pressures inside and outside the capillaries, as well as the hydrostatic pressure differences. A physiologic representation of the processes will include a unidirectional flow from blood capillaries into the cerebrospinal space — or interstitial and then CSF compartments — where the flow is modulated by capillary pressure, external (interstitial) fluid pressure, osmotic pressures inside and outside the vessels, and permeability of the membranes.

2.3.2 Intracranial hemorrhage

In an intracranial hemorrhage, such as subarachnoid or epidural hemorrhage, blood joins the CSF space. Bleeding in the cranial cavity causes the intracranial blood volume to rise slowly, which may not always manifest itself immediately. Development of a hematoma after a physical impact is a common cause, for example. The accumulation of blood volume leads to increase in ICP, which causes CPP to drop. Autoregulation attempts to compensate for the drop in CPP, but the hemorrhage may eventually exhaust the autoregulatory capacity and cause ischemic conditions.

2.3.3 Moderate and mild TBI

Severe and penetrating TBI are easily diagnosed, and treatment is generally initiated expeditiously, including transfer of the affected individual to highly specialized treatment facilities. The majority of TBI cases in the civilian and military populations, however, fall into the category of mild TBI, which can also lead to significant long-term impairment [72,73]. Unfortunately, mild TBI is notoriously difficult to diagnose. In the military population, mild TBI is strongly associated with post-traumatic stress disorder and physical health problems following deployment [61, 62], while repeated concussions in professional athletes have been associated with cognitive impairment, depression, and dementia [63,74]. Recent evidence suggests that mild TBI might also involve cerebrovascular and brain injury, and low-intensity blasts in animal studies were shown to cause a dose-dependent elevation in ICP [70].

Chapter 3

Cerebrovascular Monitoring

Diagnosing, monitoring and managing patients suffering from or suspected of having sustained brain injury requires continuous, real-time monitoring of their cerebrovascular state. ICP is a central variable — a vital sign — in cerebrovascular monitoring because of its importance in intracranial dynamics, its direct effect on cerebral perfusion, and its correlation with prognosis and outcome in head-injury patients. ICP measurements are also required in conditions such as hydrocephalus, tumor, pseudotumor cerebri, and in management of CSF shunts. Similarly, we noted in the previous chapter that autoregulation plays a central role in cerebrovascular dynamics, and ICP interacts with autoregulation in determining the patient's cerebrovascular state and its evolution. Therefore, assessment of cerebrovascular autoregulation along with ICP adds critical information in diagnosis and management of patients after neurotrauma, stroke, or at risk of developing brain injury.

In this chapter, we describe the current state of the art in cerebrovascular monitoring. In Section 3.1, we cover the current clinical methodologies for measurement of ICP. Section 3.2 discusses various approaches for the assessment of autoregulation. We give an overview of existing research on developing non-invasive ICP estimation in Section 3.3. Finally, in Section 3.4, we discuss the need and potential impact of clinically acceptable methods for non-invasive monitoring.

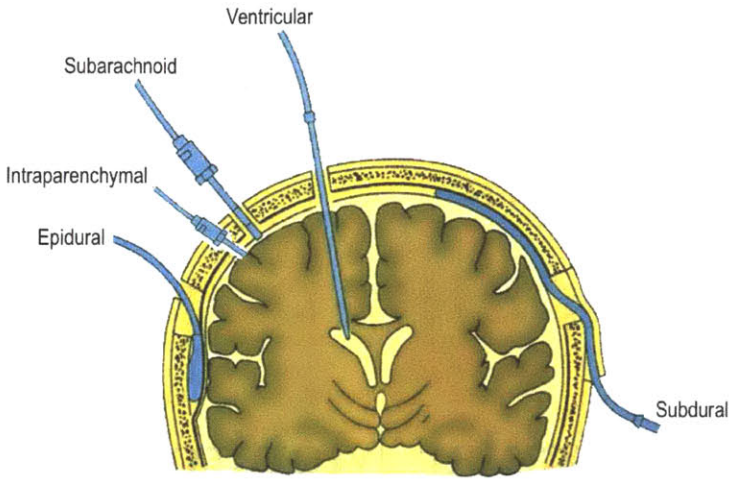

Figure 3-1: Various methodologies available for clinical monitoring of ICP; all of them require penetration of the skull and placement of a catheter or a sensor to measure ICP. (Figure is adapted from [5].)

3.1 Methods of ICP Measurement

A detailed study on ICP monitoring was presented in 1960 by Lundberg [75]. It described several records of continuous ICP measurement, labeled as "ventricular fluid pressure" because CSF pressure was measured in the brain ventricles. Since then, various devices have been designed to continuously measure and record ICP. However, even today, the methodologies applied for clinical measurement of ICP and CPP remain highly invasive [29]. They require drilling a hole in the skull and passing a catheter or pressure transducer into the brain ventricles or parenchymal space, or (with some sacrifice in measurement accuracy) into the subarachnoid or subdural spaces. They thus require neurosurgical expertise and are considered a surgical intervention. There is an associated risk of infection, hemorrhage and injury to brain tissue. A schematic of ICP monitoring methodologies is shown in Figure 3-1. Below, we discuss the measurement approaches depicted in the figure.

A fluid-filled catheter placed inside the lateral ventricle and connected to an external strain-gauge has been used as the most reliable and common measurement mechanism for several decades, since its first use in the 1950's. This is still considered the "gold-standard" ICP measurement, though it can sometimes have problems due

to the catheter getting clogged or the ventricles being compressed [29, 76]. Placing a ventricular probe requires a significant degree of care and precision. The catheter has gone through various design improvements, but the basic methodology remains the same. In addition to being the most accurate method of ICP measurement, the intraventricular catheter has the advantage that it allows for sampling and therapeutic drainage of CSF. However, this is also the most invasive of all the measurement modalities, and has greater risk of hemorrhage and infection, particularly when the continuous measurement is made over several hours or days. A fiber-optic catheter-tip transducer has increasingly replaced the fluid-filled column method. Unlike the fluid-filled catheter with external calibration, the catheter-tip transducer gets calibrated only once before insertion and cannot be re-calibrated *in vivo*.

Figure 3-1 also shows the intraparenchymal method for ICP monitoring. A pressure transducer placed in the brain parenchyma is the second-most accurate method of ICP measurement. The parenchymal probe is placed more easily than the ventricular probe. The method still poses risks of infection and bleeding, and unlike the ventricular catheter, it does not allow draining of CSF for therapeutic or diagnostic purposes. The Codman MicroSensor (Codman and Shurtleff Inc., Raynham, MA) and Camino (Camino Laboratories, San Diego, CA) probes are the two most popular devices in this category in current clinical use [77].

Other measurement methods do not pass the pressure sensor into the ventricles or the brain parenchyma, but rather access CSF in, or around, the subarachnoid space. Though, they still penetrate the skull. For example, a hollow subdural 'bolt' measures pressure in the subdural space. This approach, however, lacks the desired accuracy. At high pressures, for instance, the subdural bolt provides a lower reading of ICP because of the pressure drop associated with CSF flow from the ventricles to the subdural space. The bolt also has a tendency to become blocked [78]. Nevertheless, the bolt is still quite widely employed due to its relative ease of placement, particularly in situations where cannulation of the ventricles may not be possible. Finally, an epidural sensor is the least penetrating of the devices that access CSF in the cranium; however, it is also the least accurate of the methods currently in use.

Another approach for ICP measurement, albeit intermittent, is to access CSF in the spinal canal via lumbar puncture. A small needle, commonly called a spinal tap, is inserted into the spinal canal below the first lumbar vertebra, and a pressure transducer is connected at the other end of the needle to measure CSF pressure. Under normal conditions, the pressure measurement through this approach is a reasonably accurate estimate of ICP. This method of measurement is used in cases where ICP is not believed to be much higher than normal, for example in patients suspected of suffering from normal-pressure hydrocephalus, where ICP may be slightly increased towards the higher end of its normal range. However, in brain injury, ICP can be markedly different from the pressure in the spinal canal, and therefore other measurement procedures have to be used. Moreover, lumbar puncture during intracranial hypertension is very risky, as a high pressure gradient between the cranial fluid and the point of spinal tap can lead to sudden downward flow of CSF, pushing the brainstem towards the *foramen magnum* and thus causing fatal brain herniation. Lumbar puncture is also not suitable for continuous monitoring [1].

Accuracy of invasive methods

Out of the several available ICP measurement methodologies, only two are generally considered for routine application in clinical settings. These are the ventricular probes and the parenchymal microsensor probes. Even for the ventricular measurement of ICP, a catheter that does not allow external re-calibration (e.g., the Camino catheter-tip transducer) suffers from an accumulated zero-drift error of up to 3 mmHg in 24 hours [79].

Although the parenchymal measurement of ICP is a popular choice in clinics, it is not clear that this method provides the desired clinical accuracy. Laboratory testing of the Codman probe shows a maximum absolute error of 6 mmHg, and the sensor measurement has a drift of about 2 mmHg in a period of 24 hours, reaching up to 4 mmHg over a few days [80]. In one study involving simultaneous measurement of ICP by the Codman and Camino parenchymal probes, it was found that in cases where the two probes mostly agree, the difference between them is less than 10 mmHg

in 99% of the comparisons; however, in cases of larger disagreements, the two probes can differ by more than 15 mmHg [77]. Chambers *et al.* compared parenchymal measurements of ICP by the Spiegelberg transducer (B Braun Ltd.) against simultaneous ventricular measurements in 10 patients for several hours. The two methods provide reasonably close measurements, with a 96% agreement limit of ± 10 mmHg [81]. An important aspect of the Spiegelberg system is its unique capability of performing regular automatic zeroing *in situ*, which removes the accumulated drift and thus improves its measurement accuracy.

Subarachnoid space measurements of ICP using a bolt device were shown to have large errors, even sometimes completely inconsistent with the intracranial conditions [78]. Epidural measurement of ICP also contains significant error. Comparison of simultaneous measurements via epidural and parenchymal (or ventricular) sensors reveals a difference of 10 mmHg or larger for at least 10 minutes in 33% cases [82,83].

3.2 Assessment of Cerebrovascular Autoregulation

Another important aspect of cerebrovascular monitoring is assessment of cerebral autoregulation. As discussed in the previous chapter, a sophisticated and rather poorly understood control mechanism maintains an appropriate CBF by altering the diameters of the cerebral arteries and arterioles, thereby varying their resistance to blood flow to compensate for any change in CPP and metabolic demand. The regulatory mechanism is believed to be primarily myogenic; the smooth muscle responds to changes in transmural pressure. However, metabolic and neural mechanisms are also involved, making cerebral autoregulation a complex phenomenon [45]. Despite the complex nature of the underlying system, it is important to monitor the state of cerebral autoregulation in patients who might have exhausted their autoregulatory mechanisms due to cerebral artery disease, stroke, or TBI [84]. Such monitoring will help guide the choice of appropriate therapeutic strategy.

Due to the nature of the mechanism, assessment of autoregulation has to rely on indirect observation of cerebrovascular hemodynamics. The basic idea is to form a

qualitative or quantitative assessment by analyzing the response of CBF to abrupt changes in CPP, which may be endogenous or externally induced. An actively controlled CBF indicates a fully functional cerebral autoregulation. With the development of technology for cerebrovascular monitoring, researchers have applied such approaches to different clinical measurements in various types of neurological conditions. For instance, in an early effort, Aaslid *et al.* pioneered the use of transcranial Doppler (TCD) ultrasound to examine the cerebral arteries in order to study the autoregulation behavior of the vasculature [24, 84]. These studies remained qualitative, limited to observing the response of CBFV to a change in ABP induced by the thigh-cuff pressure method.

Mathematical modeling of cerebral blood circulation and autoregulation has been an active area over the last two decades [7, 85–88]. Models of the complete cerebrovascular system include autoregulation by incorporating control mechanisms to adapt cerebrovascular resistance and/or compliance properties to perturbations in CBF and CPP. One can study various scenarios of interest by simulating these models. Validation of these models using clinical data provides further insight into the working and dynamics of the control mechanisms.

A plethora of indices of autoregulation have been coined and analyzed [30, 89]. Most approaches discussed in the literature as potential avenues to clinical assessment of autoregulation are simply based on examining the 'black-box' input-output relationship between ABP and a measure of CBF, e.g., cerebral blood flow velocity (CBFV) or near-infrared spectroscopy (NIRS) measurements of oxygenated and deoxygenated hemoglobin. These approaches can be categorized into two groups, one pursuing a transfer function analysis (TFA) of the input and output measurements, and the other computing an autoregulation index (ARI) by analyzing the response of the system to a step change in the input. We discuss these two approaches in more detail now.

TFA assumes a linear and time-invariant relationship between the input, ABP and output, CBF (or CBFV), for the duration of an analysis window. A time-domain or frequency-domain analysis then aims to capture the dynamics of autoreg-

ulation. Various metrics of autoregulation are developed based on the input-output response [89–92]. In a typical time-domain analysis, computations may estimate the input-output cross-correlation function, as an indicator of the regulatory response of the system. In frequency-domain analysis, both gain and phase responses are computed, and it is generally noted that the phase response contains more information about autoregulation. A small phase at the desired frequency is taken to indicate lack of active control, and thus an impaired autoregulation system.

In [26], a cerebral autoregulation index is computed from the group-delay of a numerically evaluated transfer function between CBFV and a resistance-area product. The authors present a slightly adapted approach in [93], based on MAP and mean CBFV. A linear regression analysis is performed using MAP-CBFV slopes, computed only during the intervals of fluctuations in MAP. Statistics are collected for pre-term and term infants in critical-care, and results are compared in the high-risk and control groups. In [91], a transfer function between CBFV and ABP is identified using the input and output measurements.

A fundamental issue that plagues the TFA approach is that the assumption of a linear and time-invariant relation between MAP and CBFV may not universally hold [89]. It is only when the input-output coherence function [94] is close to unity that one can postulate a simple linear, time-invariant system relating input and output, and meaningfully consider its frequency response. Various examples in the literature point to the contrary, namely that the coherence function is not close to unity, though studies continue to use linear system theory in their analyses. Only a few studies address this issue by limiting the frequency-domain analysis to a certain narrow range of frequencies, e.g., to less than 0.1 or 0.15 Hz, assuming the time scale of autoregulation resides below these upper limits. Clinical data do not always adhere to this assumption, and produce low coherence in this proposed frequency range as well.

The ARI approach is based on identifying the response of CBFV to a small step in ABP, usually using an ABP perturbation induced by thigh-cuff release, though the same idea has been explored using head-up tilt or spontaneous ABP fluctuations [95]. The step response is derived from the measurements of ABP and CBFV waveforms.

An ARI index then classifies the step response into one of 10 categories, based on how rapidly and completely the response returns to zero. For a well-functioning autoregulation system, the CBFV is supposed to settle back in 6-8 seconds for a step change in ABP. As we noted earlier, however, the time scale of autoregulation is not completely known, and various hypotheses (myogenic, metabolic, neurogenic) are believed to contribute at slightly different time scales. This analysis suffers from the same problem of low input-output coherence over the range of frequencies involved in a step change, while the step response computation assumes a linear time-invariant system. Nevertheless, despite these issues, both ARI and TFA have been used in studies investigating cerebrovascular dynamics in various clinical scenarios.

Another index, Mx, proposed by Czosnyka *et al.*, is based on computing the correlation coefficient between slow spontaneous variations in CPP and CBFV [96]. A correlation coefficient close to unity is believed to be the result of a passive, or less active, system response, and therefore indicates relative loss of autoregulation. On the other hand, a negative or zero correlation is suggested to indicate good autoregulation. The analytical approach to computing Mx may be considered as intermediate between the ARI method described above and the phase analysis associated with TFA. The authors later suggested the same approach based on ABP instead of CPP [97].

Several other indirect methods to assess the state of cerebral vasculature have been proposed and analyzed. We describe one of them, which has been sometimes quoted along with Mx. A 'pressure-reactivity index', denoted as PRx, is proposed as a measure of the cerebral vasculature's ability to respond to changes in CPP [98]. It is calculated as the correlation coefficient between six-second averages of MAP and ICP. A negative or zero PRx indicates a reactive vasculature. However, it is not an exclusive measure of autoregulation, as a good PRx (negative or zero) points to an intact reactive vasculature, which does not always mean an effective cerebral autoregulation.

Another idea for indirect assessment of cerebrovascular state was described in [99], where latency between systemic and intracranial pulses, measured as the interval between the onset of the QRS complex (in the electrocardiogram) and the peak

CBFV, is related to the vascular condition of a patient. The idea appears to utilize the approach of TFA, where the group-delay or phase of the ABP to CBFV transfer function is associated with autoregulatory status. However, it is not clear if the latency can consistently provide an assessment of autoregulation, as there are several other important variables, ICP for example, that are ignored in this rather simplistic view.

A common problem with all theses indices of autoregulation is that they entail comparison with specific thresholds, based on empirical calculations and observations on a set of patient data, for the assessment of autoregulation. Lack of a clear physiological basis for these criteria makes them difficult to apply for assessment in a wider patient population involving different pathologies.

For physiologically-based assessment of autoregulation, the idea is to work with a model of the cerebrovascular system, perhaps along with its control mechanisms, and use the variation of estimated model parameters to evaluate autoregulation. We describe various cerebrovascular models in detail in the next chapter. However, we note here that there have been very few instances of carrying these models forward to the study of autoregulation. An example of research along this line is [100]. The authors present a simple three-component representation of the cerebral vasculature, and estimate resistance and compliance elements in the model for CBF regulation. However, the procedure ignores ICP estimation, and the method is not aimed at real-time monitoring.

Finally, we note that most proposed indices of autoregulation base their analysis on MAP or ABP rather than CPP which actually determines CBF (recall that CPP = MAP−ICP), and should be the basis for the autoregulation assessment. This substitution of MAP for CPP is understandable, because the invasiveness of ICP measurement makes CPP inaccessible in most scenarios. However, replacing CPP with MAP can lead to erroneous judgments, and a sound assessment should be based on CPP [30]. In other cases, such as PRx, access to ICP is required for computation of the corresponding index.

In summary, there is no clinically accepted and generally used method for au-

toregulation assessment, which consequently is still an area of active research. Various indices proposed in the literature suffer from three problems. First, even though the cerebral vasculature's state is indirectly reflected in the computed indices, their characterization criteria often lack a clear physiological basis, relying instead on correlations between indirect measures of CPP and CBF. Second, the associated computations are often based on MAP as the driving pressure, and are thus prone to systematic error; autoregulation assessment should be based on CPP rather than MAP. Third, clinical validation of these indices remains a subjective topic without any available gold standard. Our work in this thesis opens the door to some novel approaches to model-based assessment of autoregulation. It overcomes the first two flaws outlined above, in that it is based on a physiological model, and a CPP estimate is available (via our ICP estimate) for use in the characterization for autoregulation.

3.3 Approaches to Non-invasive ICP Estimation

The need for ICP monitoring for diagnosis and management in a wide spectrum of injuries to the brain is well-established. However, the treatment of such neurological conditions remains severely handicapped by the lack of non-invasive access to ICP. In recent years, brain trauma and the recognition of the hazards of repetitive concussions in the civilian and military populations have amplified the need for non-invasive ICP estimation. Various ideas for non-invasive estimation of ICP have been proposed and tested in the last three decades, and the field has been progressing. More than 40 patent applications related to non-invasive assessment of ICP have been filed in the last 30 years, half of them in the last decade, though no non-invasive method has yet made it into routine clinical use. We present a brief review here of some of the relevant literature.

Some of the initial ideas for non-invasive assessment of ICP involved using the pulsatility index (PI) and resistivity index (RI) — as well as other similar indices — derived from transcranial Doppler (TCD) ultrasound measurements of CBFV [101]. Another approach was based on relating displacement and vibrations of the tympanic

membrane to ICP [102]. Yet another procedure sought a correlation of ultrasound time-of-flight measurements, performed by sensors placed across the skull, with fluctuations in ICP [103]. However, these approaches did not give absolute measures of ICP with desired accuracies.

Over the last 15 years, several new avenues for non-invasive estimation of ICP have been explored. Schmidt *et al.* [32, 104, 105] introduced an approach using ABP and TCD-based measurement of CBFV. The method utilized TCD data to improve a linear transformation between ABP and ICP, with the goal of predicting ICP. However, as pointed out by Raksin *et al.*, it is unclear whether such a linear mapping from ABP to ICP is meaningful, and what the physiological basis for such a mapping might be [106]. Furthermore, the method relates CBFV to ICP in a highly nonlinear manner: a linear function of ABP-to-CBFV transformation coefficients, these coefficients divided by ABP, PI and pulse length is used to adapt the coefficients of the ABP-to-ICP transformation, where the weights of the linear function are calibrated using invasive measurements of ICP [104]. As a result, the selection of various algorithm parameter values, such as the number of coefficients in each regression and the number of input data samples, lacks motivation. Another aspect of the method is that the mapping has to be trained on data (including invasively obtained ICP) derived from a relevant population of patients. The resultant ICP estimates would therefore only be patient-specific in the sense that patient-specific ABP is utilized as the input to their linear transformation. The estimation performance, therefore, is going to depend critically on whether the test case is sufficiently represented in the training set. Partly for that reason, the method was upgraded by allowing it to adapt to the autoregulation status of the particular patient, thus essentially switching the algorithm choices between versions trained on one of two populations, namely those with intact and impaired autoregulation [104]. In yet another modification [105], the authors demonstrated that calibration of their non-invasive ICP estimates against true (invasively measured) ICP for a given patient reduces the prediction error [105]. However, it is in fact precisely in situations where true ICP *is not available* that accurate and robust non-invasive ICP estimates are most needed.

Utilizing ABP and TCD-based measurements of CBFV has been tried by others as well, but in more elaborate machine-learning and neural network settings. Mourad and co-workers [33] utilize ABP and CBFV as input variables to a neural network for predicting ICP. The coefficients of the neural network are learned via training on a relevant patient population for which invasive ICP measurements are obtained as a reference output. After the training phase, the coefficients are frozen and the network is applied to predict ICP in patients from measurements of ABP and CBFV on them. As the relationship between ICP and the given inputs is not learned in a patient-specific way (i.e., the neural network parameters are not patient-specific), there is no reason to expect that the method will perform well in a patient whose pathology is not well represented in the training set. Furthermore, there is no clear physiological basis to understand the structure and parameter values for the neural network, which is a serious impediment to clinical acceptance and use.

Various other approaches based on machine-learning or observing empirical correlations between ICP and physiological features of ABP and/or CBFV have been explored, for example in [34, 107], but with limited success in producing patient-specific estimates. Hu *et al.* [34] process these input measurements using a data-mining approach to extract features of ABP and CBFV waveforms, and employ a support-vector-machine approach to relate them to ICP. The learning is performed over a training set of patient records containing invasive measurement of ICP. However, the estimation performance degrades when tested on a general population.

In another empirical approach, Swoboda *et al.* [107] present a method for predicting ICP from certain features of the ABP pulse alone. Several carotid artery pressure measurements are obtained (via a tonometry sensor attached to the skin) at various levels of ICP, and a quantitative relationship is investigated between ICP and each of the several candidate waveform features, such as wave amplitude, wave systolic-diastolic gradients, ratios of harmonics after Fourier analysis, times between waveform features, distances between waveform features in the phase plane, area of the cycles on the phase plane, power of the reflected waveform, and amplitude of the reflected waveform. Only the feature(s) showing strong relationship with ICP are retained in

the ICP predictive algorithm. For example, the approach finds a strong relationship between ICP and the interval between the systolic peak and the dicrotic notch in an ABP pulse. The rationale behind this approach is that ICP affects the reflection properties of the pressure pulse by changing the 'transmission line impedance', as a change in ICP affects the intracranial compliance.

Another approach to non-invasive, albeit intermittent and resource-intensive, ICP monitoring is described by Alperin *et al.* in [106], and is based on the use of magnetic resonance imaging (MRI) to determine (incremental) intracranial compliance through an elaborate computation of incremental volume and pressure changes over the cardiac cycle, from which ICP is inferred. In [106] the authors also review several other approaches to non-invasive ICP estimation, most of which seem unsuited for routine use in a clinical environment. The most robust approaches of those reviewed involve measuring ABP and CBFV (using TCD ultrasound), but these are faulted in the paper for lacking a theoretical basis or physiological principles that relate CBFV to ICP.

Wakeland and co-workers [31,108] have introduced somewhat elaborate simulation models to demonstrate various clinically interesting scenarios. The model in their recent work contains a rather large set of parameters, most of which need to be supplied *a priori*. ICP is estimated from transient changes in clinical data streams in response to changes in the elevation of the head. It is also unclear to what extent the resultant ICP estimates are robust against variations in these pre-set parameter values, given the large set of parameters. As the parameters are expected to change from patient to patient, and also in different conditions for the same patient, the model is not aimed at real-time application in standard clinical settings.

A number of research efforts have explored using intraocular pressure — and variants of the same idea, possibly combined with some measures of blood flow in the ophthalmic artery — to infer ICP [109, 110]. A recent approach along this line was proposed by Ragauskas *et al.* in [110], and is based on applying an increasing external pressure (via pressure on the eyeball) on the extra-cranial segment of the optical artery, until a Doppler ultrasound analysis of the flow in the extra-cranial

segment matches that of the intracranial one, thus indicating that applied pressure has "balanced" the internal pressure, which is ICP. The approach has been verified against lumbar puncture-based ICP measurements, which is performed only in less severe cases of intracranial hypertension. Furthermore, the application of pressure externally to the eye is not suited to continuous monitoring, and there are also limits on the external pressure that can be applied to the eye. It also requires a high level of technical expertise to perform the procedure, as two ultrasound beams need to be focused simultaneously on two different anatomical structures.

Overall, the proposed approaches for non-invasive ICP estimation are either unsuited for routine use in a clinical environment, or require training data and/or calibration against invasively obtained ICP from patients with similar pathology and characteristics, and/or lack physiological interpretability. Our work in this thesis addresses precisely these gaps. It develops an approach for non-invasive ICP estimation based on a physiological model to interpret the accessible ABP and CBFV measurements and thereby infer ICP, CPP, and cerebrovascular properties, which can potentially lead to an assessment of autoregulation. The approach is patient-specific, as it does not require any training on population data, and does not need calibration using invasive measurements of ICP. The method is computationally simple enough to run in real-time and provide continuous ICP estimates at the patient-bedside, and even in ambulatory settings.

3.4 Potential Impact of Non-invasive ICP Monitoring

Currently, monitoring of ICP and CPP is performed only in the most severe cases, due to the invasiveness of measurement methods. The primary impact of a non-invasive method of ICP monitoring will be on a large patient pool in which ICP monitoring is currently avoided, but in which the availability of a clinically reliable ICP estimate would improve the timeliness and accuracy of diagnosis, and open up treatment options. In this pool are patients who transition from primary brain insult to sec-

ondary injury [69, 71], for example in an epidural hemorrhage, in which intracranial blood volume increases or a hematoma develops quietly over a few hours after the initial impact, and eventually leads to extremely severe situations and — all too often — death. A non-invasive ICP monitoring modality would allow emergency medical technicians (EMTs) or medics to assess and track ICP for patient management on route to a properly equipped trauma center. It can also prove vitally important in emergency care, for faster diagnosis and titration of therapeutic intervention.

Non-invasive ICP monitoring can also be very valuable in mild and moderate cases of TBI, in which ICP is typically not monitored currently, but in which diagnosis and management remain a difficult challenge. Enough evidence has accumulated showing the potential benefit of ICP measurement in such cases [61, 62, 70, 72]. Furthermore, a non-invasive ICP technology might help us distinguish between mild, moderate and severe TBI, and understand the physiological links that may underlie psycho-cognitive disorders after various degrees of exposure to brain trauma. Currently patients diagnosed with post-traumatic stress disorder (PTSD) are treated as having a psychological impairment, rather than a potential physical injury to the brain, as might be indicated by ICP and cerebral autoregulation abnormalities. However, growing evidence suggests that a blast wave may cause injuries to the brain at the cellular and tissue level – due to impact of the tissue with the cranium and shear along it, and also due to the sudden variations in blood pressure and flow; these insults may well damage cerebrovascular function in subtle ways [62].

Another benefit of a non-invasive and thus a less risky method of ICP monitoring is the possibility of early diagnosis and tracking of hydrocephalus, and also in programming of CSF shunts in chronic hydrocephalus patients. One might also expect such monitoring to be beneficial in post-neurosurgery monitoring of patients.

Finally, non-invasive ICP estimation can potentially provide useful information in a still broader population in which elevated ICP may be involved in the relevant pathophysiological pathways, possibly even in such common conditions as migraine, where studies indicate a correlation between intracranial hypertension and migraine involving bilateral transverse sinus stenosis [111], as well as in chronic daily headache [112].

Part II

Mathematical Modeling and Estimation

Chapter 4

Models of the Cerebrovascular System and Intracranial Dynamics

In this chapter, we discuss mathematical modeling of the cerebrovascular system. We first provide an overview of various modeling approaches, and then provide a literature review of cerebrovascular models that are based on physiological understanding of the system. These models represent relevant physiological relationships in a mathematical and computational form, which can be used to mimic and analyze the system's behavior. We then develop a simple model of the cerebrovascular system that is particularly suited for robust, real-time ICP estimation and is radically simpler than other cerebrovascular models. Our simplified model provides dynamic constraints that link clinically available measurements to the desired cerebrovascular quantities.

Section 4.1 describes two common modeling approaches and provides examples in each category. In Section 4.2, a review of cerebrovascular models is given, leading in Section 4.3 to our modifications of a well-studied model. Finally, we describe our simple cerebrovascular model in Section 4.4.

4.1 Background on Modeling Approaches

Mathematical modeling of the cerebrovascular system has been an active area of research in the past four decades, and several developments have been made over these years [6,8,31,52,87,88,113]. We can classify the models into two categories, based on the approach used to build them or the rationale behind the relationships provided by these models. In the first category are approaches that attempt to identify top-level statistical correlations, or transfer function relationships, among key cerebrovascular variables. These models rely on data-mining or machine-learning methods applied to observed data, and extract relationships by training or learning on a patient database. Such models are usually aimed at supporting statistical inference. In the second category, models are based on physiological understanding of the interaction of the system components, and are typically obtained by synthesizing the results of many detailed studies of the components and their interactions. These models therefore represent fairly detailed structural or mechanistic knowledge of the physiology, and understanding about mechanisms at play at various levels of detail and at different time scales. Such models are generally aimed at supporting simulation studies. We describe these two categories of models below.

4.1.1 Black-box and statistical models

In this category, models are derived by observing statistical correlations of some of the quantities of clinical interest, and then extracting relationships among them. Generally, such relationships are blind, completely or partially, to the physiology of the system that contains these variables. Therefore, these models are often called black-box models as they merely provide empirical relationships connecting their input to their output variables. In certain settings, this approach reduces to obtaining a transfer function representation connecting output to input variables. The complexity of models in this category varies from simple linear regression to complicated, multi-layer neural networks involving nonlinear processing elements. The task of learning or training model parameters involves minimizing some measure of the error between

the model output and observed data (the training set). Neural networks and other machine-learning models are examples of this approach, where the unknown relationships are estimated by training on available data, and the learned relationships are applied to the test data to obtain performance statistics.

These models can sometimes expose simple empirical relationships, but in these cases it is often true that such relationships reflect well-understood physiology. These models are generally 'physiology-blind' mathematical relationships that can fit the observed data streams, but are limited in their ability to yield clinical insight.

In the context of the cerebrovascular system, this modeling approach has been used to seek relationships between specific variables, rather than representing the complete system. For example, a transfer function between ABP and CBF may be sought for the assessment of autoregulation [89, 91, 92], or a correlation coefficient between slow fluctuations in CPP and mean CBFV may be computed as an indicator of autoregulation [96]. Similar approaches can be found in [26, 28, 84, 114, 115]. We have already discussed a few examples of this type of model in Sections 3.2 and 3.3, in the context of non-invasive approaches for ICP monitoring and assessment of autoregulation. Here we briefly review only two of them, to illustrate this approach further.

In [33], a machine-learning approach is used to relate ICP to ABP and TCD-based CBFV. A neural network is trained on a relevant patient population (the training set), for which invasively obtained measurements of ICP have been obtained. Parameter weights in the neural network represent the estimated relationship between the two model inputs, ABP and CBFV, and its output ICP. This empirically learned model is assumed to remain the same in a broader population, as the parameters of the neural network are frozen after the training phase, and the model is used to predict ICP in other patients (the test set). Even though the model allows complex nonlinear relationships to be extracted, there is no guarantee for its accuracy in patients with a pathology that is not well represented in the training set. Furthermore, the model lacks the sort of interpretability required to facilitate understanding and acceptance by clinicians. Another machine-learning approach for ICP estimation is proposed

in [34], and a relationship between ICP, ABP and CBFV is extracted via correlating these measurements in a training set of patient data.

Sometimes, a model provides a relationship between certain selected features of the input waveforms and a cerebrovascular quantity. For example, in [107] several morphological features of the carotid artery blood pressure waveforms are tested for correlation with ICP via a linear regression analysis. In some cases, the interval between the systolic peak and the dicrotic notch in the ABP pulse shows a significant correlation with ICP, and is therefore used as a relationship for prediction of ICP. The success of this model, however, is limited to situations similar to the ones used in performing the regression analysis.

4.1.2 Physiological models

In the second category, mathematical models are formulated using what is understood about the underlying physiology of the cerebrovascular system. A compelling example of this approach, though in the cardiovascular domain, is the work of Arthur Guyton [48]. He illustrated several human physiological mechanisms via their mechanistic representations, usually comprising an interconnection of components that each capture the physiological behavior of a particular functional unit. Guyton's representations can often be conveniently cast into mathematical form.

Models of this kind represent the system behavior at varying levels of detail, through components and associated parameters that have physiological interpretations, and the relationships among these that are governed by the relevant physiology. It is rather natural to analyze these models, and relate them to the clinical measurements at various points in the system. Unlike the statistical or black-box models described in the previous section, correlations among various system variables do not come as surprises, as one can, in principle, trace the relationships (though this can be non-trivial in a large and complex model). An important attribute of these models is that they can resonate well with clinicians, who routinely think in similar physiological terms and are the end-users of these models or developments based on them.

Such mechanistic models are attractive from many points of view, including for purposes of instruction and simulation [116]. However, one problem is the context of their application to real-time monitoring is that they can often (as in the Guyton model) have many more parameters than can be reliably estimated from clinical data. Strategies such as subset selection [117] or careful model reduction will then need to be employed for parameter estimation [118].

The Windkessel model of the cardiovascular system is an example of a much simpler physiologically-based model [35,36]. It provides a dynamic-system representation relating ABP and cardiac output through aggregate properties of the vasculature. The two model parameters are an aggregate compliance (representing primarily the compliance of the large arteries) and aggregate resistance, the total peripheral resistance, (representing primarily the resistance of the arterioles and capillary beds). Due to its elegant simplicity, Windkessel-type models have been extensively used to study and illustrate cardiovascular dynamics, as well as for application in patient monitoring [37]. The paucity of parameters in this model makes it particularly suited to estimation from data.

A few examples of physiologically-based models of the cerebrovascular system can be found in [8, 52, 87, 88, 108]. Typically, various functional-anatomical units are represented by lumped-parameter system models, and interconnections of these compartments build up the whole system. The level of anatomical and physiological detail determines the model complexity: models that represent detailed structure involve a large number of compartments [7, 113]. However, as already noted, the limited availability of physical data at various spatial resolutions means that these models cannot generally be fully validated. Currently, such models are mainly restricted to teaching, demonstration and simulation purposes only. Nevertheless, simpler models in this category are amenable to parameter estimation in clinical settings. Since models in this category are physically meaningful, observations made on these models can be readily related to the clinical environment.

The work in this thesis revolves around this category of models. We next provide a detailed review of various cerebrovascular models in this class in the next section.

4.2 Review of Cerebrovascular Models

Several mechanistic mathematical models have been developed based on the anatomical structure and physiology of the intracranial and cerebrovascular system. Lumped-parameter models are one class of models that aggregate various anatomical segments of the system into a single functional unit. In the context of modeling the hemodynamic system, these models are commonly formulated in terms of electrical analogs, with pressure corresponding to voltage and blood flow to current. Resistors then represent resistance to blood flow, capacitors represent the compliance of vascular segments, and inductors represent the inertial properties of the blood and vascular wall (though inertial effects are often ignored). Resistance to flow depends on the radius of a vessel (in the case of blood flow) or the permeability of the membrane (in the case of CSF formation and reabsorption); compliance of a structure depends on its elasticity. The desired resolution of these anatomical segments controls the number of resistance and compliance parameters in a particular model. A relatively comprehensive review of models developed to characterize the dynamics of the cerebral vasculature and the CSF system is provided in [31]. In the following, we provide a brief review of some of the salient model development efforts.

A three-compartment model, comprising the brain, blood, and CSF, has been the basis for our understanding of the intracranial system for about 150 years [38–40]. Around four decades ago, models of intracranial dynamics started to go into more anatomical detail, paying attention to the distributed nature of the system, and examining the dynamics of each compartmental sub-system. Based on the involved physiological mechanisms, the cerebrovascular system can be divided into at least the following major compartments: the cerebral arterial compartment, the cerebral venous compartment, the CSF generation and reabsorption system, and the cerebrospinal compartment. The last two are sometimes studied as one system. Most of the early mathematical modeling efforts focused on only one of the compartments rather than the complete cerebrovascular system. We provide a brief summary of each sub-system before discussing the more comprehensive models.

Cerebrospinal compartment

Mathematical models to characterize the CSF volume and pressure relationship focused on the CSF system, independently of the vasculature and cerebral hemodynamics [50–52]. In these models, the key variables are the flow of CSF, the resistive drop along its pathways, and the intracranial compliance (due to the brain tissue and vasculature that bounds CSF). These models were used to study the dynamics of ICP, which by then could be measured in clinical settings. An important contribution of these models was the analysis of the nonlinear relationship between ICP and the CSF volume. The work in [51] presented a mechanical perspective of the intracranial system and represented its dynamics in a mathematical model. The authors employed their model to simulate and analyze hydrocephalus and normal-pressure hydrocephalus. Further developments in regard to CSF dynamics and hydrocephalus were presented using a two-compartment model in [119].

Two important observations can be made on the terminology used in models related to intracranial physiology. First, the space containing CSF inside the cranium is often termed the intracranial space, which we think can possibly be mistaken as the entire space inside the cranium. We instead call it the CSF space or ventricular space. (The latter term ignores the relatively smaller volume of the subarachnoid spaces.) Second, with the exception of some detailed models of CSF flow, the literature in this area does not distinguish between the ventricular fluid pressure (VFP) and the CSF pressure elsewhere, and summarily labels as ICP any measurement of CSF pressure, irrespective of measurement location. We use ICP to denote VFP.

CSF generation and reabsorption

Generation of CSF from specialized capillaries (the choroid plexus) inside the brain ventricles and its reabsorption in the veins through the arachnoid villi have been studied through experiments in humans and animals [46, 47]. CSF formation is known to be an active process, and the CSF production rate is affected by variations in ICP and CBF. Mathematical models either represent this by a constant source of flow from the capillaries to ventricular space ignoring the pressure-dependent variations [120],

or by a unidirectional flow through a resistance element that connects to the capillary pressure at one end and ICP at the other [87]. Pathway for the reabsorption of CSF is also modeled as a resistance element, and the outflow is determined by the difference of ICP and venous pressure. This is shown in detail in the models below.

Cerebro-arterial compartment

Similar to models of the arterial vasculature elsewhere in the body [116, 117], the dynamic relationship between ABP and blood flow through cerebral arteries is represented by a system comprising resistance and compliance elements. The arterial bed can be represented by one or more sub-compartments, depending on the desired resolution. Again, the models introduced later in this subsection provide examples and more details.

Cerebro-venous compartment

The dynamics of the cerebro-venous system gained particular attention due to the peculiar property of collapse of the larger cerebral veins (before entering the dural sinuses). This phenomenon is due to external pressure, ICP, being higher than the luminal blood pressure [13]. Typically, ICP is above 7 mmHg, and blood pressure at the large veins is about 5-6 mmHg, dropping further to less than 5 mmHg at the sinuses. The collapse behavior led to adoption of the Starling-resistor model for representing blood flow through the cerebral veins [13, 14]. The Starling model for the cerebro-venous system is employed in several cerebrovascular models. We have discussed this briefly in Chapter 2, and more detail is given in Appendix A.

Models of the complete system

Representations for the complete cerebrovascular system have also been proposed. For instance, Sorek *et al.* proposed a lumped-parameter compartmental model of the cerebrovascular system to represent the dynamics of cycle-averaged pressures and flows in the cerebrovascular system [6]. As shown in Figure 4-1, the system comprises seven compartments: brain tissue, arteries, capillaries, veins, venous sinus,

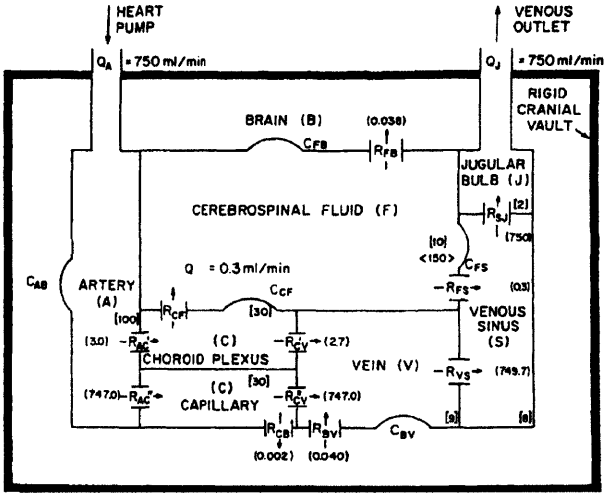

Figure 4-1: A compartmental model of the cerebrovascular system by Sorek *et al.* [6]. The nominal pressure and flow values at different compartments are specified inside braces and parenthesis, respectively.

jugular bulb, and CSF. The pressures and flows in the system are related by nine resistance elements and five compliance elements. A prime objective of the authors was to estimate the model parameters from the nominal values of various pressures (including ICP) and flows, and thus demonstrate clinically interesting profiles of these parameters. Conversely, the model was simulated to predict pressure changes as the resistances and compliances were changed.

However, it was Ursino and Lodi's model in 1988 that, for the first time, combined almost all the essential compartments and relevant dynamics. They proposed a series of mathematical models of the cerebrovascular system, validating via simulations, refining, elaborating and also simplifying their models. A key aspect of the first Ursino-Lodi model [87] is that it combined the CSF dynamics with the cerebral blood circulation, included a Starling resistor for venous collapse, and also introduced a mathematical, albeit phenomenological, equivalent of autoregulation. The CSF dynamics were represented by introducing CSF generation and reabsorption pathways, and a notion of compliance of the bounding surfaces of the ventricular space was borrowed from previous studies. A simulation study of the model was carried out to replicate clinical waveforms [88]. These models represented the cerebral vasculature

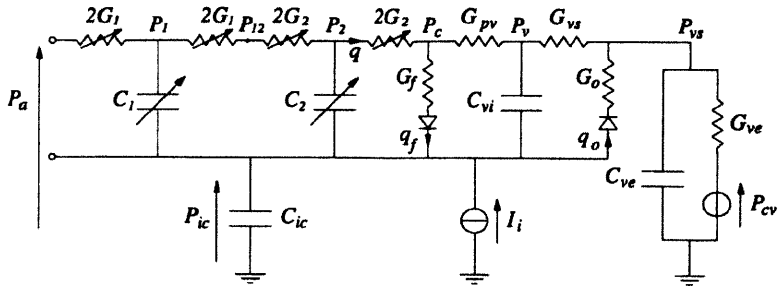

Figure 4-2: An elaborate model of the cerebrovascular system proposed by Ursino *et al.* [7], shown in the form of an electrical circuit. The variables labeled as G, C, P and q denote conductance, capacitance, voltage and current, respectively. The arrows indicate time-varying components to accommodate autoregulation.

in an elaborate manner, separating the arteries from arterioles, and large from small veins. These models contained certain nonlinear elements, making their analysis and parameter estimation challenging. In order to represent cerebrovascular autoregulation, an external control mechanism was used to vary certain resistance and compliance elements in the model in response to variations in mean arterial blood pressure (MAP) and mean CBF, though several variants of the feedback mechanism and the time-constant of its action were tried in later publications [7, 9, 121].

An example of this type of model is shown in Figure 4-2 in an electrical circuit analog. A model of autoregulation using pressure-dependent compliance and flow-dependent resistance was adopted in [9], about a decade after the introduction of their first mathematical model. During these several revisions, the authors developed simpler versions — with fewer compartments — of their initial mathematical model, and also included interaction of ICP dynamics and CO_2 reactivity [7]. Another variation of these models was aimed at mathematical characterization of ICP dynamics, which the model represented through a nonlinear dynamical system. Various simulations were carried out to demonstrate the effects of injecting fluid into the ventricular space, varying the intracranial compliance, and controlling the gain of the autoregulation loop. This model is relatively simple, yet characterizes the cerebrovascular dynamics fairly accurately, as shown in several simulation studies. It has been used in further studies and investigations into cerebrovascular dynamics [122]. After Ursino

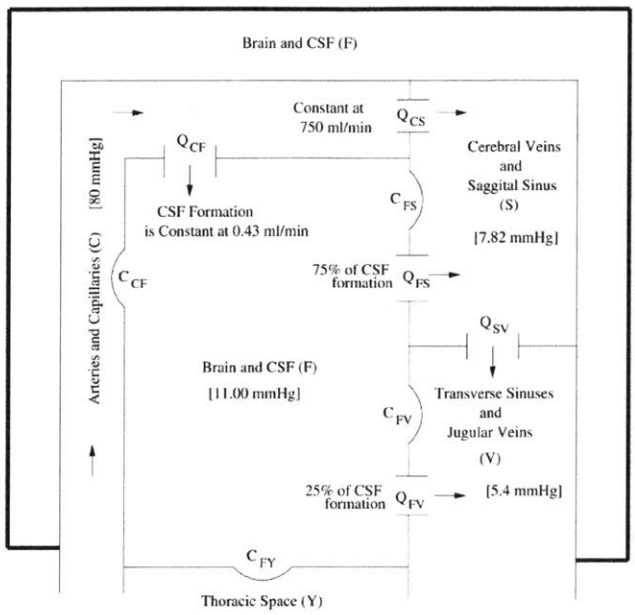

Figure 4-3: An elaborate model of the cerebrovascular system proposed by Stevens *et al.* [8].

Lodi models, the cerebrovascular models developed by others retained the four necessary compartments and important aspects, such as the Starling-resistor mechanism and CSF formation and reabsorption.

The development of compartmental models of the cerebrovascular system is still an active area of research. These models aim to either illustrate certain clinical scenarios of interest or to relate the clinical data-streams that are now available rather conveniently and abundantly. For instance, Stevens *et al.* recently proposed a model to represent idiopathic intracranial hypertension [8]. This work derives from earlier work on ICP dynamics by the authors [113]. Figure 4-3 shows a mechanical description of their model. The approach looks strikingly similar to the models discussed above, and in particular the model by Sorek *et al.* [6]. However, the focus of this modeling exercise is to study idiopathic intracranial hypertension and its various modes. In another recent development [108], Wakeland *et al.* presented a six-compartment simulation model, and demonstrated that with pre-set model parameters (nominal values from the literature are used as the baseline values) the simulated waveforms

can be made to match clinically measured data. They used the model to replicate ICP in response to two external interventions: variations in the head-of-bed angle, and respiratory rate. The authors use a nonlinear optimization routine to estimate a small set of model parameters. The routine is used to predict ICP from the pre-set model parameters, though the parameters are allowed to change from one intervention to the next.

In summary, compartmental models of the cerebrovascular system have been employed to represent relevant dynamics and explain clinical scenarios. As access to clinical data has become easier due to the advances in technology, further developments in the area of cerebrovascular models are expected.

4.2.1 A Simple Ursino-Lodi model

As described above, mathematical models developed by Ursino and Lodi captured the cerebrovascular and intracranial dynamics, and also included control mechanisms to represent autoregulation. These models are easy for simulation studies, and hence were adopted by various other researchers as the basis of further explorations. However, these models contained too many unknown parameters to be robustly identified from clinically accessible measurements. After several simplifications, Ursino and Lodi proposed another model, containing only 8 unknown parameters [9]. We describe this model in more detail below, and refer to it as the Ursino-Lodi model in the remainder of this thesis.

Figure 4-4 shows the structure of the Ursino-Lodi model [9]. Various important segments of the model are labeled by associated pressure (P), flow (q) — both in terms of their cycle-averages — and intrinsic vascular properties, such as resistance (R) and compliance (C). Anatomical segments are indicated by subscript letters: 'a' denotes arterial, 'c' denotes capillary, and 'v' denotes venous. Sub-compartments in the venous region are distal ('d') and proximal ('p') to the arterial side. Intracranial parameters are indicated by 'ic'. Resistance to CSF formation and reabsorption/outflow are indicated by R_f and R_o, respectively, and I_i denotes external injection (or withdrawal) of fluid into (or from) the ventricular space. Arrows at the arterial compliance

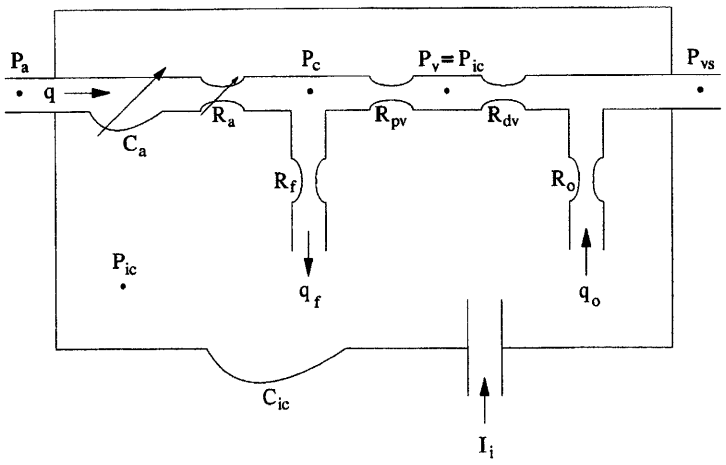

Figure 4-4: A mechanical view of the cerebrovascular system in terms of pressures and flows [9].

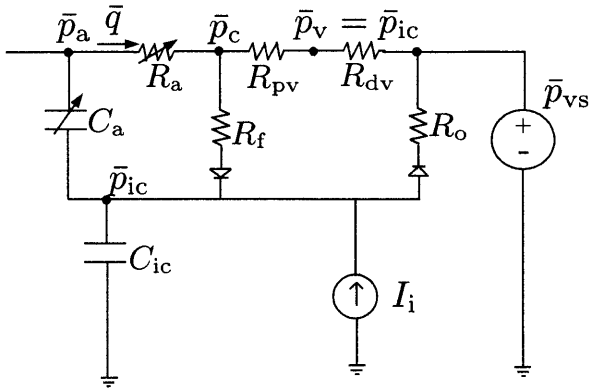

Figure 4-5: The Ursino-Lodi model of the cerebrovascular system, given in an electrical circuit form.

and resistance indicate their dynamic nature, which is responsible for autoregulation. The Starling resistor phenomenon is captured by the condition $P_v = P_{ic}$. Finally, P_{vs} denotes pressure at the venous sinus.

In Figure 4-5, we redraw the Ursino-Lodi model as an electrical circuit model. The original model is formulated in terms of average or mean pressure, flow and volume. Mean pressure at the inlet of a main artery into the cerebral section — right or left MCA — is represented as $\bar{p}_a$, and is almost the same as mean ABP measured elsewhere in the arterial tree. Mean CBF is represented as flow through the arterial resistance, and is shown as $\bar{q}$. Mean pressure inside the ventricular space is denoted

as $\bar{p}_{\mathrm{ic}}$, and the compliance of the bounding surfaces of the ventricular space (which is commonly termed as intracranial compliance) is denoted as C_{ic}. The Ursino-Lodi model adopts a nonlinear relationship between CSF volume and ICP [52], and specifies the incremental compliance as

$$C_{\mathrm{ic}} = \frac{1}{k_{\mathrm{E}}\bar{p}_{\mathrm{ic}}}, \tag{4.1}$$

where k_{E} is a coefficient representing elastance of the ventricular space. This C_{ic} yields an exponential dependence of pressure on volume, consistent with the so-called Monro-Kellie principle [40]; (see Section 2.1.3 , and in particular Figure 2-6).

$$V_{\mathrm{ic}} = V_{\mathrm{ic0}} + \frac{1}{k_{\mathrm{E}}} \ln \frac{\bar{p}_{\mathrm{ic}}}{\bar{p}_{\mathrm{ic0}}}, \tag{4.2}$$

$$\bar{p}_{\mathrm{ic}} = \bar{p}_{\mathrm{ic0}} e^{k_{\mathrm{E}}(V_{\mathrm{ic}} - V_{\mathrm{ic0}})}. \tag{4.3}$$

The arterial-arteriolar segment is represented by a single compliance C_{a} and resistance R_{a}, lumping together the properties of large and small arteries and arterioles. Both R_{a} and C_{a} are modeled as time-varying parameters, to implement autoregulation. Larger arteries have more elastance than small arterioles and capillaries, which are almost purely resistive.

The venous space is divided into two resistive segments, R_{pv} and R_{dv} respectively, to distinguish proximal veins from the collapsible lateral lacunae and bridge veins. The model assumes that the last section of the venous system is collapsed and therefore mean cerebral venous pressure at the interface between un-collapsed and collapsed veins is essentially equal to mean ICP. Furthermore, the venous resistances are kept constant, since they play no role in autoregulation. Compared to arteries, cerebral veins store more blood volume, and their blood volume drops only when ICP rises or the pressure at the venous sinuses decreases. These variations in the venous blood volume occur at relatively long time scales, and therefore their effect on compliance is not important in modeling short-term blood flow dynamics. Mean pressure at the venous sinus is denoted as constant, $\bar{p}_{\mathrm{vs}}$. CSF formation occurs at the capillaries and is captured by a unidirectional flow with a high resistance R_{f}, while CSF reabsorption or outflow is represented by R_{o} at the level of the large veins. Both

R_f and R_o are large compared to R_a, R_{pv} or R_{dv}. Furthermore, the time constants for CSF formation and reabsorption are large compared to the time constants of flow through the arterio-venous system. External injection of fluid into the ventricular space is shown by a current source I_i.

The model has two different control (autoregulation) mechanisms postulated for the arterial compliance and arterial-arteriolar resistance, respectively. Compliance is varied in response to flow changes above or below its nominal value. Positive or negative change in flow is passed through a first-order negative feedback loop to compensate for the flow change. This is expressed in the following mathematical relationships:

$$x = \sigma\left(G\frac{\bar{q} - \bar{q}_n}{\bar{q}_n}\right), \tag{4.4}$$

$$\frac{dC_a}{dt} = \frac{1}{\tau}\left(-C_a + x\right), \tag{4.5}$$

where $\bar{q}$ represents mean CBF, $\bar{q}_n$ represents the nominal value of mean CBF, G is the autoregulation gain with a nominal value of 1.5, σ is a sigmoidal function with different lower and upper saturations, and τ is the time constant of the regulation, which is set to a nominal value of 20 sec.

The second postulated mechanism adapts arterial resistance. A change in perfusion pressure — due to a change in MAP, ICP or both — induces immediate variations in R_a to result in vasoconstriction or vasodilation. This behavior is implemented with the following relationships:

$$V_a = C_a(\bar{p}_a - \bar{p}_{ic}), \tag{4.6}$$

$$R_a = \frac{k_R.C_{an}^2}{V_a^2}, \tag{4.7}$$

where Va is the volume stored in the arterial compliance, k_R is a constant parameter, and C_{an} is the nominal value of the arterial compliance. Details of the parameter values and the particular sigmoidal function can be found in [9].

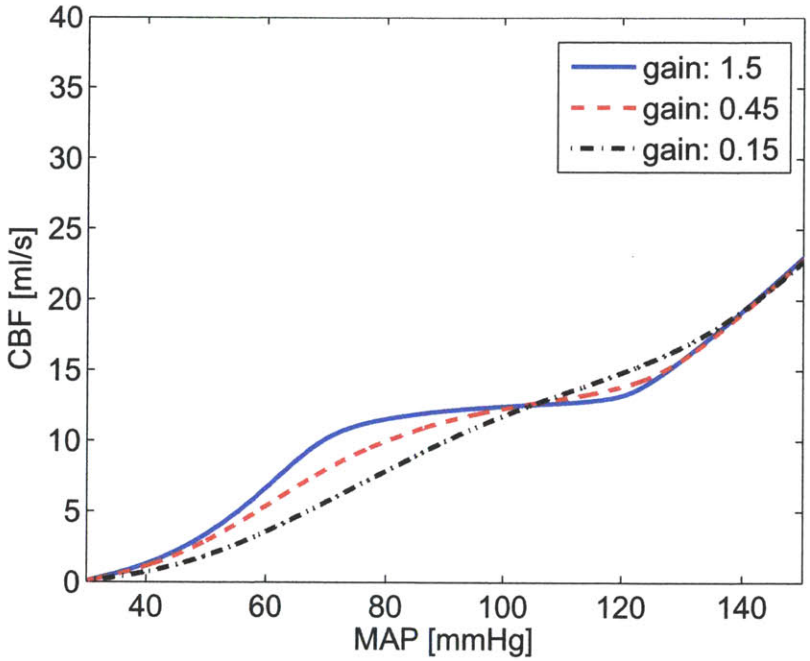

Figure 4-6: Typical autoregulation plateau observed from our implementation of the Ursino-Lodi model. For each value of the autoregulation gain, MAP was increased linearly over 20 minutes (quasi steady-state simulation) and the corresponding mean CBF was recorded.

We implemented the model using the nominal values for the model parameters reported in [9] and supplied the model with a synthetic MAP time-series as input. Simulation of the model generated mean CBF. Figure 4-6 shows the autoregulation displayed by the model at various values of the control gain. Typical autoregulation response is observed for the normal autoregulation (gain value of 1.5) over MAP variations in the range 60-130 mmHg; as MAP gradually increases from 30 mmHg to 180 mmHg (in a period of 20 minutes), the CBF remains almost constant at the selected nominal value of 12.5 ml/s. Weakening the model's autoregulation by decreasing the gain value demonstrates gradual loss of autoregulation.

4.3 Modified Ursino-Lodi Model

As pointed out above, the Ursino-Lodi model is specified in terms of mean quantities. However, hemodynamic waveforms have morphological features that contain informa-

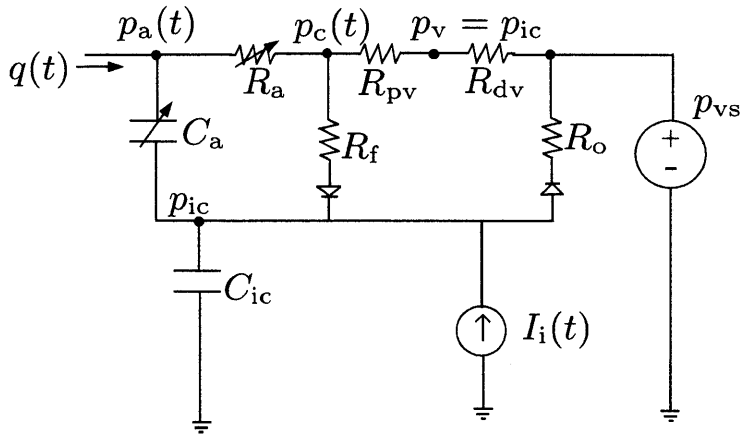

Figure 4-7: Modified Ursino-Lodi model.

tion about the properties of the dynamic system they are derived from. From a system identification perspective, it is prudent to extract information from these intrabeat variations in hemodynamic quantities, due (primarily) to cardiac pulsation, and gain possible advantage in estimation of the desired parameters. Therefore, we need the model to reproduce pulsatile behavior. To achieve this, we modify the Ursino-Lodi model by providing it with a pulsatile ABP waveform as the input. We also define the input flow, $q(t)$, to the model as pulsatile CBF, measured at the large elastic cerebral arteries (rather than in the arterial resistance). The control mechanisms remain implemented in terms of the average quantities, as this is physiologically more likely. Since the input as well as the internal quantities now assume instantaneous values, rather than average values, running-window averages are computed for the pressure and flow, for updating the resistance and compliance through the control loop at every time-step. The step-size for evolving the model is also chosen appropriately for producing waveforms at high temporal resolution.

The modified model is shown in Figure 4-7, where we have used $p_a(t)$, $q(t)$ and $p_{ic}(t)$ to indicate the pulsatile nature of the model quantities. Also CBF, $q(t)$, is shown at the arterial side of the model.

Simulated data for the modified model

We simulate the modified model to mimic interesting clinical scenarios. The wave-

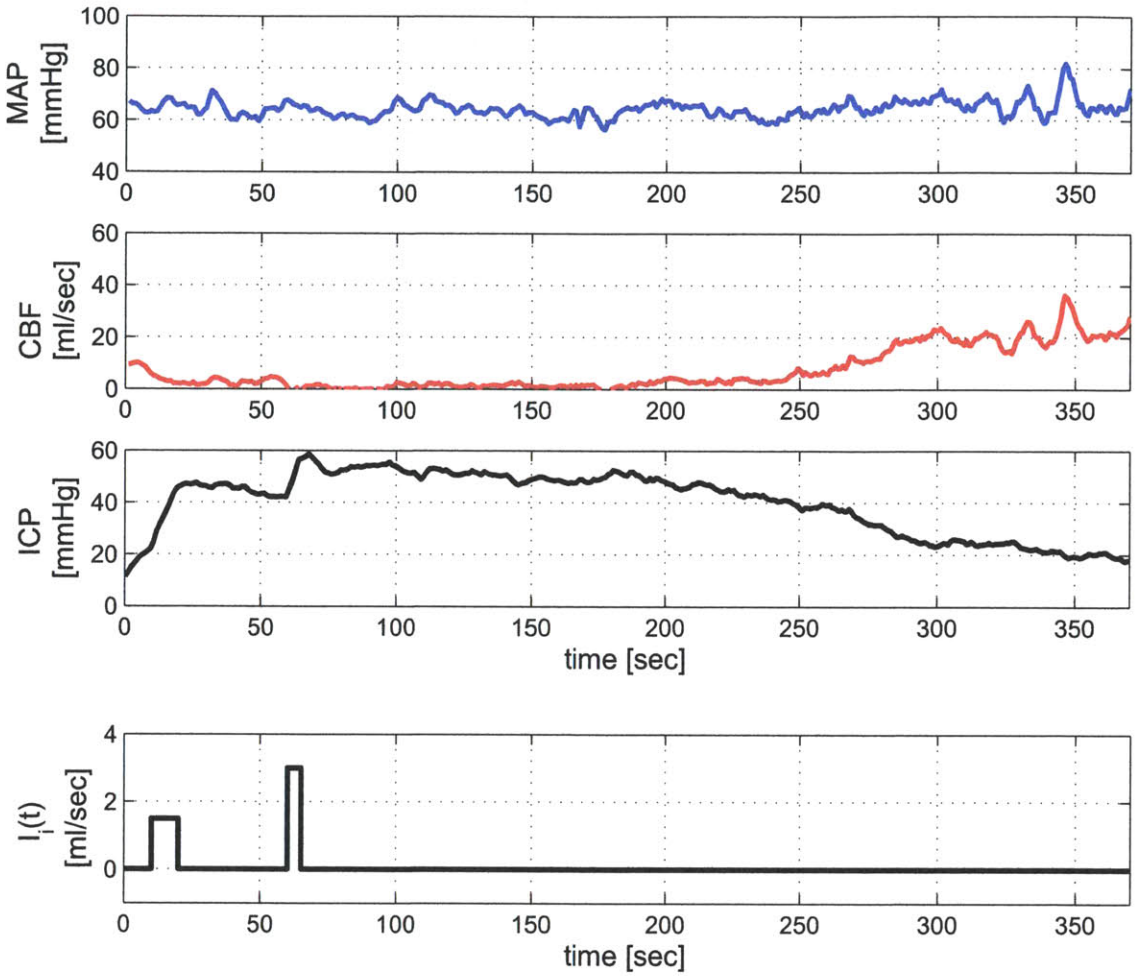

Figure 4-8: The modified Ursino-Lodi model was simulated to synthesize ABP, CBF, and ICP. Beat-to-beat averages (or means) of ABP (top), CBF (second row) and ICP (third row) are shown. The last window shows the perturbation $I_i(t)$ that causes sudden rises in ICP. A pulsatile ABP waveform is used as an input to drive the model, and the simulated CBF and ICP waveforms are recorded as model outputs.

forms generated by this model are later used as a first step to test the parameter estimation scheme that we shall develop. A set of sample beat-to-beat averages of ABP, CBF and ICP is shown in Figure 4-8, and Figure 4-9 shows the pulsatile waveform behavior of these signals over a period of 20 seconds.

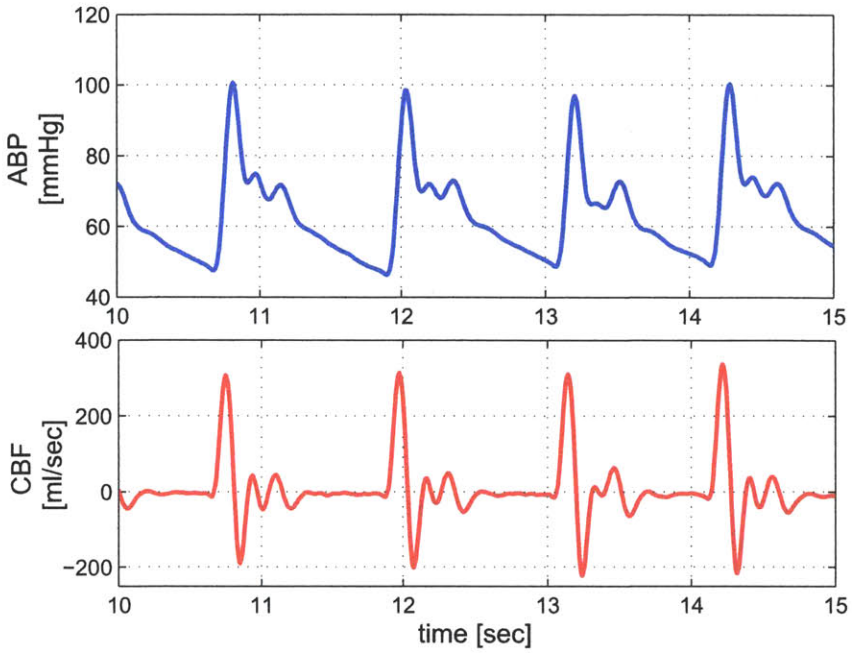

Figure 4-9: Simulated ABP (top) and CBF (bottom) waveforms obtained from the modified Ursino-Lodi model. Figure highlights the intrabeat pulsatility in these signals.

4.4 Reduced Model for ICP Estimation

We note that even the simplest realistic models of cerebrovascular dynamics generally involve about a dozen unknown parameters and state variables. On the other hand, direct clinical measurements are possible for only a very few variables, primarily due to limited access to probe the closed cranial system. That makes the challenge of uniquely and robustly identifying model parameters from actual data very hard, if not impossible. For example, the adapted model presented in Figure 4-7 is a second-order system with nonlinear components, has eight parameters, and two state variables. We can hope to get only two measurement signals, ABP and CBF.

This prompts us to devise simpler or reduced-order models for the system under study, with the objective of making them amenable to system identification. Our primary objective is to obtain a model that can be used for estimation of ICP and cerebrovascular autoregulation. We also want the model to have physiologically in-

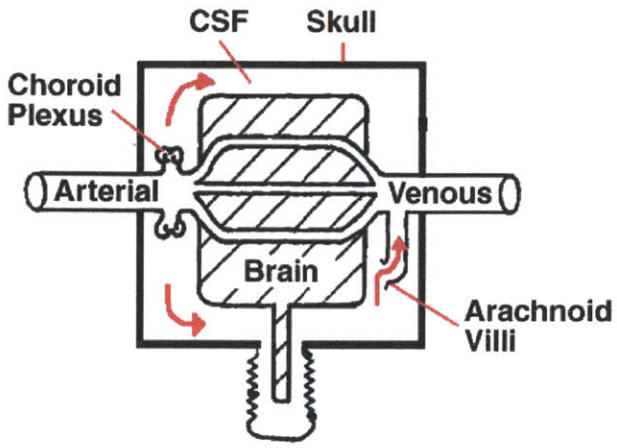

Figure 4-10: Compartmental view of the intracranial space (adapted from [4]). Red arrows indicate circulation of CSF.

terpretable parameters. Starting from a compartmental view of the cerebrovascular space in the next section, we make a few key observations about the physiology and time scales of dynamics to derive a reduced model. We then highlight important features of the model that are exploited in the next chapter for developing parameter estimation schemes.

4.4.1 Simple compartmental view of cerebrovascular system

A schematic view of the cerebrovascular system is shown in Figure 4-10. It displays the three major compartments of the intracranial system, namely brain, the vasculature, and the ventricular space. Blood enters the cerebral space through the arteries, branches into smaller vessels and is collected back by the veins. Arrows in the ventricular compartment indicate the flow of CSF, which is formed at special capillaries in the choroid plexus, and is reabsorbed into the venous system through arachnoid villi or granules. The pressure of CSF inside the ventricular space is ICP, and acts as the effective downstream pressure for cerebral perfusion.

4.4.2 Model

We make the following observations from the compartmental view shown in Figure 4-10; these are key to our simplified mathematical model.

- Starling resistor for venous collapse: As mentioned above, ICP acts as the effective downstream pressure for flow through the cerebral vasculature, because it leads to venous collapse in regions where it exceeds venous pressure. This phenomenon is sometimes described by a simple model, the Starling-resistor [11,12], and is the reason for defining cerebral perfusion pressure as CPP = MAP − ICP.

- Slow and fast dynamics: The second observation utilized in our model reduction is that the dynamic response of the system comprises both fast (on the order of a beat period) and slow (about two orders of magnitude longer than a beat period) time-scales, which can be separated. CSF formation and reabsorption pathways have resistances to flow that are at least two orders of magnitude higher than the dominant cerebrovascular resistances. Thus intracranial CSF volume changes and the associated changes in mean ICP occur at a much slower time-scale (several minutes) than a cardiac beat period (normally less than a second). For the duration of a beat period, the contribution of these slow variables is negligible and can be ignored. After a beat period, any cumulative effect on the system is reflected by the new values for R, C, and ICP.

- Intrabeat variation in instantaneous ICP: We note that under normal conditions, intrabeat variations in instantaneous ICP are small relative to the variations in ABP — only about 5 mmHg in ICP compared to about 50 mmHg or more in ABP — and any physiological changes in the baseline or mean ICP occur over several beats (as noted in the previous paragraph). Moreover, providing only one ICP estimate every beat still meets the clinical requirement of ICP monitoring sufficiently well, and intrabeat pulsation is not generally required to be monitored. Therefore, to make the estimation task easier, ICP can be assumed constant during a beat period.

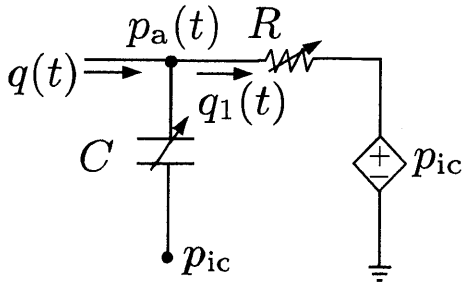

Figure 4-11: Our simplified model obtained from an aggregate mechanistic view of the intracranial space. By exploiting some key physiological features, the computational model provides a dynamic relationship between ICP and the measurable quantities [10].

We exploit these observations to propose a reduced model with only three beat-to-beat varying parameters, namely resistance R, compliance C, and ICP [10]. Figure 4-11 shows our model in a electrical circuit form, where the arrows on the components indicate their time-varying nature due to autoregulation. However, the figure does not show the control mechanisms that govern the variation of these parameters. The model provides a dynamic constraint relating ICP, ABP and CBF.

In the above model, ICP is denoted as p_{ic}, ABP_{mca} as $p_a(t)$, and CBF as $q(t)$. The parameter R represents the overall resistance to cerebral blood flow as seen from the inlet, and C captures the combined compliance of the vascular walls of the arterial bed and compressibility of the brain tissue surrounding these vessels. The net transmural pressure is the difference of ABP and ICP. Beat-to-beat variations in R and C represent the dynamic response of the cerebral vasculature — such as changes in the vessel diameter in order to regulate cerebral blood flow — and changes in effective compliance under different intracranial conditions. For the duration of a beat period, the dynamic relationship described by the model is given by

$$q(t) = C\frac{dp_a(t)}{dt} + \frac{p_a(t) - p_{ic}}{R}. \tag{4.8}$$

Since the model parameters vary from one beat to the next, the correct notation is R_n, C_n, and p_{icn}, where n indicates the beat number. However, we assume this will be clear from the discussion, and omit the subscript to avoid notational clutter.

4.4.3 Validation via simulation

Though our simplified model is derived from a mechanistic representation of the cerebrovascular system, employing our observations about the relevant physiology, we can validate the behavior of the model by comparing some of the common variables against larger models. We employ a simulation approach to validate our simplified model by synthesizing waveforms from the modified Ursino-Lodi model and then using the reduced model to estimate model parameters from the simulated waveforms of ABP and CBF. Clinically interesting scenarios are generated by appropriate perturbations during the simulation. The parameters of the reduced model are estimated (by the algorithm we describe in the next chapter). Over a wide range of simulated ABP changes, the parameter estimates follow dynamic changes in ICP, usually to within 10% of the reference values. Estimates of arterial compliance and cerebrovascular resistance tend to fall within 5% to 10% of the references values. These results suggest that our reduced model captures the dynamic relationship among ABP, CBF and ICP quite well. More detail of the simulation study is given in Appendix B.

4.5 Salient Features of the Reduced Model

Physiologically-based model parameters

Our development of a reduced mathematical model is rooted in the physiology of the cerebrovascular system, instead of statistical correlations or black-box models that provide limited insight into the system. A direct result of this approach is that all our model parameters have a physiological interpretation. This distinguishes our approach, and model, from empirically learned relationships, where one does not know what the model parameters might represent in the physiological system. Despite its low complexity, our model represents the cerebrovascular system quite well for the purpose of monitoring of ICP and autoregulation (see Chapters 6 and 7).

Starling resistor model for venous collapse

Our model exploits the Starling-resistor like behavior of the cerebral vasculature and

blood flow through it. This allows us to reduce the complexity of the model, and provide a simple first-order dynamic relationship between the pressures and flows in the cerebrovascular system.

Constraints vs. complete representation

The model does not capture all the relevant mechanisms/dynamics of the cerebrovascular system. It rather provides constraints relating the observations and the desired quantities. Furthermore, our model is aimed at characterizing the cerebrovascular system at an aggregate level.

Despite this, our model can be thought of as representing the behavior of whatever portion of the cerebral vasculature the blood flow variable $q(t)$ is channeled through. This $q(t)$ may be just the blood flow in the left MCA, for example, or in the right MCA, rather than the entire aggregate arterial inflow to the cerebral vasculature. If it is the left MCA flow, for instance, then R and C in the model represent the resistance and compliance experienced by this particular portion of the flow. Crucial to the relevance of our reduced model for ICP estimation (and to the success we have had with it) is that ICP is essentially uniform in the ventricular space, and thus serves as the downstream pressure on whatever arterial channel $q(t)$ is measured in. Similarly, ABP is essentially uniform across all arterial inlets to the cerebral vasculature. Some validation of this picture is provided later in the thesis, when we show rather consistent agreement between ICP estimates computed separately from left MCA and right MCA flow measurements.

Interpretation of compliance

The compliance C in our model captures the elastically distensible nature of various layers between blood in the arterial vessels and CSF in the ventricles. It thus represents the aggregate compliance due to the elasticity of the arterial walls and the brain tissue. The pressure at one end of this compliance element is ABP or $p_{\mathrm{a}}(t)$, while the CSF pressure is ICP, so the compliance represents the relationship between the transmural pressure (ABP $-$ ICP) and cerebral blood volume (CBV).

4.6 Concluding Remarks

In this chapter we have provided a brief review of mathematical models of the cerebrovascular and intracranial system dynamics. We also presented our explorations and modifications of the Ursino-Lodi model, which we simulated to generate pulsatile dynamics of ABP, CBF and ICP. Finally we developed a simple physiological model of the cerebrovascular system for the purpose of ICP estimation. We exploited several key features of the relevant physiology to obtain a drastically simpler representation than those in the literature. Specifically, the model contains only three patient-specific parameters, namely R, C, and ICP, which are allowed to vary from beat to beat, and which we hope to estimate in a robust manner by processing the accessible clinical measurements of ABP and CBF. Parameter estimation is the subject of the next chapter.

Chapter 5

Model Parameter Estimation

In the previous chapter, we described our reduced-order model of the cerebrovascular system. A key feature of this model is that it captures relationships among the essential cerebrovascular variables in a simple mechanistic form. If we can acquire measurements corresponding to some of the variables in the model, we can develop strategies for identifying the model parameters. We can in fact acquire continuous waveforms that are good approximations of the blood pressure and flow at the arterial inlets to the cerebral vasculature. As the reduced model has only three unknown parameters (R, C, and ICP), it is very suited to estimation of these unknown parameters.

We have developed a suite of possible algorithms for real-time processing of clinical measurements of ABP and CBFV waveforms, to obtain continuous estimates of the unmeasured parameters. The various algorithms incorporate different strategies, including the use of modulating functions, estimation of parameters in a single stage or in two and three stages, and estimation from the cycle-averaged pressure and flow measurements. In this chapter, we describe one of these algorithms in detail, and discuss the others in Appendix C. The algorithm described in this chapter is the one we focused on for validation and further investigations.

In Section 5.1, we describe the estimation algorithm, stage by stage. Section 5.2 describes the accessible clinical measurements and the challenges they pose. We discuss the issue of ABP phase-offset estimation in Section 5.3 and also give a summary

of the required pre-processing steps. Section 5.4 then lays out the full estimation algorithm. We conclude this chapter by summarizing the salient features of the estimation algorithm in Section 5.5.

5.1 Estimation Algorithm

The dynamic relationships given by the reduced model allow computational processing of the ABP and CBF measurements to identify the model parameters, including ICP (which is considered constant within a beat, just as R and C are). Recall the differential equation relating the measured variables $q(t)$ and $p_{\mathrm{a}}(t)$ to the parameters R, C, and p_{ic}:

$$q(t) = C\frac{dp_{\mathrm{a}}(t)}{dt} + \frac{p_{\mathrm{a}}(t) - p_{\mathrm{ic}}}{R}\,. \tag{5.1}$$

We develop a two-step algorithm to identify the model parameters. The algorithm processes non-invasive, time-synchronized clinical waveform measurements of radial ABP and CBFV at the MCA, to provide beat-by-beat estimates of R, C, and ICP. An important feature of our approach is that the algorithm extracts intrabeat information from the beat morphology to identify the model parameters, including ICP, from the two measured waveforms (ABP and CBFV) for each cardiac beat. We now describe the steps of the algorithm.

Step I: Compliance estimation

Sharp transitions in $p_{\mathrm{a}}(t)$ induce a large flow into the arterial compliance, and a comparatively negligible flow through the resistance branch during such transitions. The typical ABP waveform does indeed contain a sharp rise in every beat — within about one-tenth of a beat period — from diastolic pressure to systolic pressure. Hence, during that short transition period, the input flow can be primarily attributed to the compliance branch:

$$q(t) \approx C\frac{dp_{\mathrm{a}}(t)}{dt}\,. \tag{5.2}$$

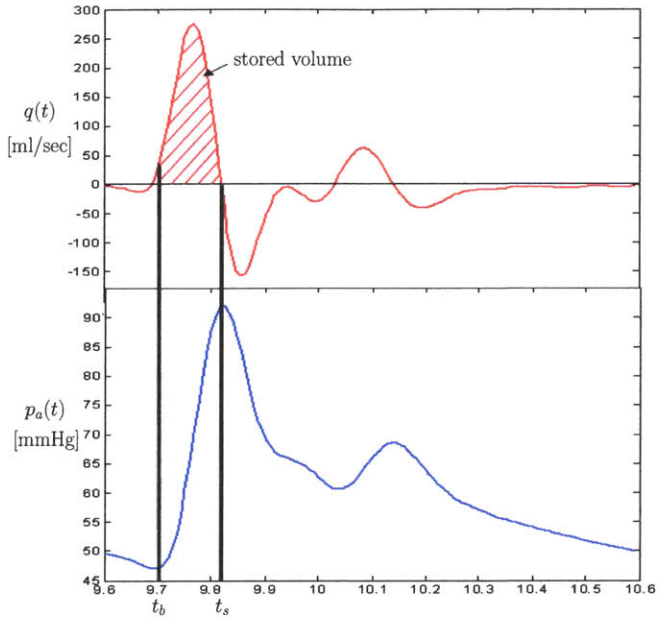

Figure 5-1: Graphical description of the idea for compliance estimation: when arterial blood pressure has a steep gradient, capacitance (or compliance) offers the smallest-impedance path for the current (or flow) $q(t)$, storing charge (volume) on C. The points marked as t_b and t_s correspond to the 'begin' and 'stop' times of the diastolic-to-systolic transition of ABP within the indicated beat, and the stored volume is equal to the area under the flow over this interval.

A graphical description of the situation is given in Figure 5-1. Let t_b and t_s correspond respectively to the begin-time and stop-time of the sharp diastolic-to-systolic transition, in a particular beat of the ABP waveform $p_\mathrm{a}(t)$. We can estimate C by integrating (5.2) over the transition period, obtaining

$$\widehat{C} = \frac{\int_{t_b}^{t_s} q(t)dt}{p_\mathrm{a}(t_s) - p_\mathrm{a}(t_b)} \ , \tag{5.3}$$

where we use a 'hat' to indicate an estimate.

Step II: Estimation of R and ICP

Using the result of the estimation in Step I, we can calculate the flow through the

resistance as

$$\widehat{q}_1(t) = q(t) - \widehat{C}\frac{dp_a(t)}{dt}. \tag{5.4}$$

Note that direct computation of the derivative may accentuate noise in the ABP waveforms. In our simulation experiments, we used an experimental ABP waveform as the input, and a simple finite-difference scheme over the sampling interval of 8 ms (sampling frequency is 125 Hz) provided an adequate approximation of the derivative. In more noisy cases, a more careful approximation scheme will need to be used.

As the resistance R and ICP are assumed to stay constant over a beat interval, ICP can be described in terms of $\widehat{q}_1(t)$ as

$$p_{ic} = p_a(t) - R\widehat{q}_1(t). \tag{5.5}$$

This equation has two unknown quantities, R and p_{ic}. Since $p_a(t)$ and $\widehat{q}_1(t)$ vary freely during a beat period, we can write (5.5) for at least two different time instants t to eliminate one of the unknowns. For example, picking t_1 and t_2 within a beat period and subtracting the two equations yields

$$\widehat{R} = \frac{p_a(t_2) - p_a(t_1)}{\widehat{q}_1(t_2) - \widehat{q}_1(t_1)}. \tag{5.6}$$

Finally, substituting $\widehat{R}$ for R in (5.5), and taking the average over a beat period provides the desired ICP estimate:

$$\widehat{p}_{ic} = \overline{p}_a - \widehat{R}\,\overline{\widehat{q}_1}, \tag{5.7}$$

where the bar indicates the beat-averaged quantity, i.e., $\overline{x} = \frac{1}{t_n - t_{n-1}} \int_{t_{n-1}}^{t_n} x(t)dt$, and t_n marks the onset of the n^{th} beat.

Remark on least-squares set up: In order to mitigate the effects of noise in the measurements and reduce dispersion in the estimates, the algorithm employs a sliding window of several consecutive beats of the measured waveforms, and computes

a least-square-error solution for the estimates in (5.3), (5.6) and (5.7). For example, estimation using (5.6) over N consecutive beats involves least-squares solution to a system of equations of the form

$$\widehat{R}\left[\delta q_1[n]\ \delta q_1[n+1]\ \cdots\ \delta q_1[n+N-1]\right] = \left[\delta p_{\mathrm{a}}[n]\ \delta p_{\mathrm{a}}[n+1]\ \cdots\ \delta p_{\mathrm{a}}[n+N-1]\right], \tag{5.8}$$

where

$$\delta x[n] = x(t_2[n]) - x(t_1[n]), \tag{5.9}$$

and $t_1[n]$ and $t_2[n]$ are the points chosen in the n^{th} beat. The resulting least-squares estimate is

$$\widehat{R} = \frac{\sum_{k=n}^{n+N-1} \delta q_1[k]\delta p_{\mathrm{a}}[k]}{\sum_{k=n}^{n+N-1} \delta q_1^2[k]}. \tag{5.10}$$

Remark on selecting t_1 and t_2: To reduce sensitivity to noise in $\widehat{q}_1(t)$, it is advantageous to pick t_1 and t_2 such that $\frac{dp_{\mathrm{a}}(t)}{dt} \approx 0$ at t_1 and t_2, e.g., near the maximum and minimum of the ABP beat. With this choice, $\widehat{q}_1(t)$ in (5.4) is least affected by errors in $\widehat{C}$, and therefore estimates of R and ICP are also minimally affected. Specifically, consider the estimate $\widehat{q}_1(t)$:

$$\begin{aligned}\widehat{q}_1(t) &= q(t) - \widehat{C}\frac{dp_{\mathrm{a}}(t)}{dt}, \\ &= q_1(t) + (C - \widehat{C})\frac{dp_{\mathrm{a}}(t)}{dt}.\end{aligned} \tag{5.11}$$

That is, the error in the estimate of C scales the derivative of $p_{\mathrm{a}}(t)$ and adds as error in the estimate of $q_1(t)$. In (5.6), we compute the difference of $\widehat{q}_1$ at t_1 and t_2, hence we need to pick t_1 and t_2 such that $\frac{dp_{\mathrm{a}}(t)}{dt}|_{t=t_1} \approx \frac{dp_{\mathrm{a}}(t)}{dt}|_{t=t_2}$. One obvious choice of t_1 and t_2 that meets this criteria is the local minimum and maximum points on $p_{\mathrm{a}}(t)$ within each beat, where $\frac{dp_{\mathrm{a}}(t)}{dt} = 0$.

Remark on beat onset detection and signal quality: Our algorithm processes the measured data on a beat-by-beat basis. Therefore, a necessary pre-processing step before the algorithm can run is to mark the start time for each cardiac beat. We include this in our pre-processing module. Various other essential pre-processing steps are performed to remove measurement or equipment noise and artifact from the acquired signals, to detect beat onsets, and to compute an index of input signal quality that is used in the subsequent computational steps. Details of the signal quality assessment and utilization are discussed separately; it suffices to say here that parameter estimates are computed only during periods when the associated signal quality of the input measurements is deemed good enough for performing the computational steps.

5.2 Clinical Measurements

5.2.1 Arterial blood pressure

Peripheral ABP in a critical care setting is most easily obtained via an intra-arterial catheter at the radial artery. Alternatively, a non-invasive method for continuous ABP measurement is based on the volume-clamp method, and is commercially available as the Finapres, Portapres and Finometer [123]. These devices calculate pressure in the arterial bed of the finger via a pressure-cuff method, in which a control mechanism maintains the blood volume in the finger constant by applying pressure externally. Measurement of blood volume is made through an infrared light sensor, and the applied pressure is considered as mirroring the ABP inside the arteries. Detailed descriptions of the volume-clamp method are in [123, 124]. Measurement accuracy of this method, as compared against intra-arterial catheter measurements, is typically good enough for clinical application [125]. Our algorithm uses peripheral ABP (measured at the radial artery or at the finger) as a proxy for the cerebral ABP in the model, though we shall shortly describe a phase-offset correction we make to the peripheral ABP waveform to get a better proxy.

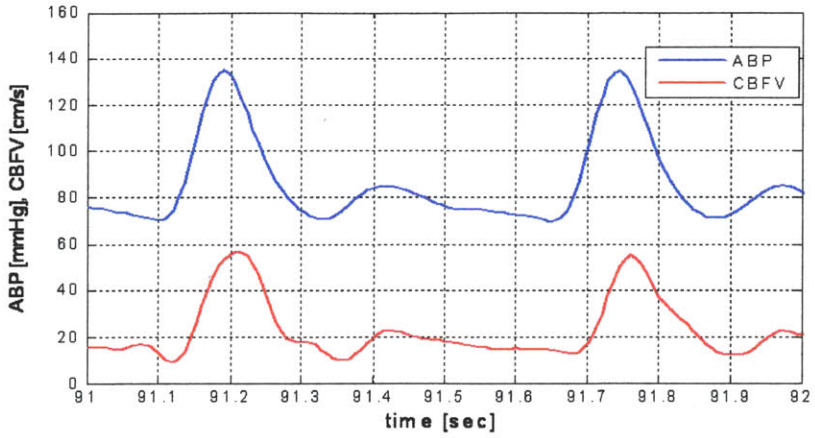

Figure 5-2: Radial ABP (blue, top) and CBFV at the MCA (red, bottom) recordings shown over a period of almost two cardiac beats. ABP is measured in units of mmHg and CBFV in cm/s.

5.2.2 Cerebral blood flow (velocity)

To measure CBFV, we utilize a transcranial Doppler (TCD) ultrasound device, which provides continuous and non-invasive measurement of CBFV. The ultrasonic transducer is typically focused on the left or right middle cerebral artery (MCA) for a unilateral measurement, but a simultaneous or bilateral recording with two transducers is also possible. Besides being the major cerebral artery, the MCA is also accessible via a convenient insonation window at the temple. The measurements are performed by an expert technician, as training and skill are needed to localize the target blood vessel. Aaslid *et al.* demonstrated that a TCD ultrasound exam of the cerebral arteries can be routinely performed in clinical settings [24].

The device performs Doppler-based computations on the backscattered ultrasound wave to determine the speed of the moving (flowing) blood in the targeted artery. A detailed description of the operation of the device involves various parameters, including operating frequency, absorption coefficients of bone, tissue, and blood, acoustic power, and interference sources; see [24, 126].

Taking into account the cross-sectional area of the artery, velocity can be converted into volumetric flow. It turns out, as we shall shortly show, that our ICP estimate does not depends on the cross-sectional area, so CBFV rather than CBF suffices. On

the other hand, our R and C estimate *do* depend, in reciprocal ways, on the assumed area. Figure 5-2 provides a snapshot of the measurement waveforms to show typical pulse shapes and features of the ABP and CBFV waveforms. It is desirable for the continuous waveforms to be sampled at a rate high enough (100 Hz or above) to capture the beat morphology well, and to allow robust time-domain analysis of the measurement waveforms.

5.2.3 Discrepancy between available and desired measurements

So far we have paid little attention to the discrepancies between the accessible measurements of *radial* ABP and CBFV respectively, and the desired *cerebral* ABP and CBF. Below we discuss the problems caused by these differences.

I. **Radial artery ABP in place of cerebral artery ABP**

Clinical measurement of ABP is obtained at a peripheral location, e.g., via a radial artery catheter or a Finapres device on the finger, but the associated CBF is measured at a cerebral artery, generally the MCA. This discrepancy requires translating the measured pressure, $\mathrm{ABP}_{\mathrm{rad}}$, into pressure at the level of the cerebral vasculature, $\mathrm{ABP}_{\mathrm{mca}}$, before it can be associated with CBF by the model.

Ideally, the radial ABP measurements should be transformed to cerebral ABP, perhaps via a transfer function relating the measurements at the two locations, applying ideas similar to those in [127, 128]. However identification of such a transformation is not obvious without any reference cerebral ABP measurement. Therefore, we resort to using an approximate translation. Mean arterial pressure, in the supine position, is about the same at the radial and cerebral arteries. We ignore the differences in the pulse morphology. However the propagation times of the pressure wave to these two sites are quite different, and, as might be expected, the difference significantly affects our parameter estimates. Therefore, it is critical to compensate for the relative time-shift of $\mathrm{ABP}_{\mathrm{rad}}$ with

respect to ABP_{mca}. We shall invoke the relationships provided by our model and utilize physiological features of the waveforms to develop an estimation algorithm in Section 5.3 for this phase-offset, as part of the pre-processing phase in our method.

II. **CBFV in place of CBF**

A second issue regarding the clinical measurements is that TCD ultrasound provides CBFV, which needs to be converted to CBF by taking into account the cross-sectional area of the artery. However, we show below that our ICP estimate is independent of any constant scale factor for CBFV. To see this, we re-arrange the dynamic relationship (5.1) provided by the reduced model as

$$p_{\text{ic}} = p_{\text{a}}(t) + RC\frac{dp_{\text{a}}(t)}{dt} - Rq(t)\,, \tag{5.12}$$

and recall that $q(t)$ represents CBF. Let $v(t)$ denote the CBFV measurements used by the algorithm in place of $q(t)$ in the model, and assume the two are related by $q(t) = \alpha v(t)$, where α is the unknown scale factor that converts CBFV into CBF (e.g., cross-sectional area of the insonated cerebral artery), or any other scaling required to get true $q(t)$. Re-writing (5.12) in terms of $v(t)$,

$$p_{\text{ic}} = p_{\text{a}}(t) + RC\frac{dp_{\text{a}}(t)}{dt} - R\left(\alpha v(t)\right)\,, \tag{5.13}$$

$$= p_{\text{a}}(t) + (\alpha R)\left(\frac{C}{\alpha}\right)\frac{dp_{\text{a}}(t)}{dt} - (\alpha R)\,v(t)\,, \tag{5.14}$$

$$= p_{\text{a}}(t) + \widehat{R}\widehat{C}\frac{dp_{\text{a}}(t)}{dt} - \widehat{R}v(t)\,, \tag{5.15}$$

where

$$\widehat{R} = \alpha R\,, \tag{5.16}$$

$$\widehat{C} = \frac{C}{\alpha}\,. \tag{5.17}$$

Thus, our ICP estimate is not affected by α, but the resistance and compliance

estimates are scaled (in reciprocal ways). We therefore use CBFV measurements in our algorithm, without converting them to CBF. Despite scaling by α, the estimates $\widehat{R}$ and $\widehat{C}$ will capture trends in the underlying resistance and compliance, as long as the scale factor is relatively constant over an observation interval.

III. **Correction in ABP measurement for patient posture**

As we described above, the estimation algorithm uses radial measurement of ABP as a surrogate for cerebral ABP, without any translation except the time-delay. Depending on the position of the subject, however, the radial measurement may be different from the cerebral ABP, due to the effect of the hydrostatic fluid column between the MCA and the location of the pressure transducer. When a subject is in the supine position, and the pressure transducer is calibrated at the level of the heart, mean ABP at the cerebral arteries is about the same as that in the aorta or the radial artery. However, in the head-up position, mean ABP at the cerebral arteries is lower than ABP at the level of the heart, and this must be corrected before feeding into the estimation algorithm. Generally, for a normal-height adult, the length of the hydrostatic column is about 15-20 cm, which translates to about 15-20 cmH_2O or 10-15 mmHg correction in ABP. If this posture change is not accounted for in the ABP measurement, which is usually calibrated to the level of the heart, a bias in the ICP estimate will result when using the given (uncorrected) ABP measurement.

5.3 Pre-processing and Phase-offset Estimation

The estimation algorithm processes data on a beat-by-beat basis. This requires the beat boundaries in the input waveforms to be marked before carrying out the estimation steps described above. Also, the recorded waveform data stretches from a few minutes to several hours, and almost invariably contains various recording artifacts, noise, and signal-interrupts, which calls for noise removal and labeling the waveforms for signal quality. Furthermore, as already noted, the radial ABP needs

to be time-shifted for aligning with the CBFV measurements. These steps are part of the pre-processing stage of the algorithm.

5.3.1 Pre-processing steps

A few necessary pre-processing steps are performed before applying the estimation algorithm of Section 5.1 on the clinical waveform measurements.

- **Noise removal:** A simple finite-impulse response low-pass filter with cut-off frequency at 16 Hz is applied in cases where the clinical measurements are significantly contaminated with wide-band high-frequency noise. The cut-off frequency was chosen to remove the kind of noise in some of the available measurements, however a different choice of cut-off or filtering method may be desirable in other settings.

- **Re-sampling:** The patient data were acquired at different sampling frequencies (20, 30, 50 and 70 Hz). Instead of tuning the algorithm to receive data at varying sampling frequencies, we introduce an up-sampling step. Before subsequent processing by the estimation algorithm, the input ABP and CBFV waveforms are up-sampled at a higher rate of 125 Hz, to aid the beat onset detection and the extraction of the intrabeat features by the algorithm.

- **Beat onset detection:** To be able to process each beat of data individually, the algorithm needs to mark the beat boundaries, or beat onsets. We employed an algorithm that detects beat onsets for a given ABP waveform [129]. The algorithm is based on computing a weighted 'slope-sum' function over a running window of the ABP signal, and then comparing its value against certain adaptive thresholds.

- **Beat annotation and signal quality assessment:** All ABP and CBFV beats were labeled according to the quality of data acquisition, noise, artifact and no-recording period. These labels are combined to form a signal quality

metric, which is then used by the estimation algorithm to select the estimation windows.

- **Phase-offset correction in ABP:** To compensate for the relative time-shift of $\mathrm{ABP_{rad}}$ with respect to $\mathrm{ABP_{mca}}$, we develop a routine that exploits the model constraint between CBF and $\mathrm{ABP_{mca}}$ to provide candidate phase-offsets. The suggested offsets are applied to $\mathrm{ABP_{rad}}$ before further processing by the estimation algorithm.

5.3.2 Phase-offset estimation

The ABP and CBFV measurements are made at different anatomical sites, so there is an unknown phase-offset between the measured and desired pressure waveforms. This offset must be compensated for prior to application of the estimation algorithms. Our offset selection mechanism makes use of the physiological relationships that exist between cerebral pressure and flow. We describe two different methods to estimate the phase-offset that should be applied to radial ABP to get a better approximation to ABP at the MCA.

Method 1: Recall that our model relates cerebral ABP and CBF as

$$q(t) = C\frac{dp_{\mathrm{a}}(t)}{dt} + \frac{p_{\mathrm{a}}(t) - p_{\mathrm{ic}}}{R}. \tag{5.18}$$

Note that near the inflection point of the rising ABP pulse, the term $\frac{dp_{\mathrm{a}}(t)}{dt}$ has its maximum value, which then rolls off to zero by the peak systolic point, where $\frac{dp_{\mathrm{a}}(t)}{dt} = 0$. Thus, within a given beat period, the maximum value of $q(t)$ must occur close to the time corresponding to the inflection point of the rising $p_{\mathrm{a}}(t)$ waveform. To estimate the time-shift between $\mathrm{ABP_{rad}}$ and $\mathrm{ABP_{mca}}$, we determine the time-shift that is required to align the maximum of the CBFV pulse with the inflection point of the $\mathrm{ABP_{rad}}$ pulse. The resulting phase-offset is then used to shift the measured $\mathrm{ABP_{rad}}$. The time-shifted version of $\mathrm{ABP_{rad}}$ is then taken as $\mathrm{ABP_{mca}}$, which is labeled as $p_{\mathrm{a}}(t)$ in the model.

The phase-offset estimation is performed over a window of several consecutive beats to mitigate the effects of noise and timing jitter, and an offset value is computed for each beat by sliding the window by one beat. Finally, a sanity check is performed to see if the estimated phase-offset sequence has a low dispersion. If the sequence has a narrow range of values, a single phase-offset, taken as the median of the offset sequence, is applied to the complete record rather than a phase-offset for every new beat. Other approaches may be tried, where a new phase-offset is estimated every few beats or minutes.

Method 2: We note that during each cardiac cycle, the ABP pulse goes through regions where its derivative is close to zero. During these time intervals, near the local maxima and minima, the compliance-related term in (5.18) can be safely ignored. That simplifies the relationship between CBF and cerebral ABP to a purely resistive one, determined by R and ICP only. Exploiting this, we develop a procedure to identify the time-intervals where $\frac{dp_a(t)}{dt}$ is relatively small in each cycle, and to determine a linear relationship between CBFV and the shifted ABP in those intervals. The procedure is repeated for various phase-offsets applied to the radial ABP, and the offset that results in the smallest residual error with a linear fit is selected. Figure 5-3 depicts, for two candidate phase-offsets, the fit of a least-squares line to the selected points, based on the $\frac{dp_a(t)}{dt} \approx 0$ rule, chosen from CBFV and the shifted radial ABP. Several phase-offsets are applied; the worst (left) and the best (right) are shown in Figure 5-3, and the one corresponding to the smallest residual error is selected as the best phase-offset. As in the previous method, a sliding window of several consecutive beats is employed and a sequence of phase-offsets is obtained.

Based on the above methods, we implemented a routine that constructs a set of offset candidates, and ICP estimation results are obtained for each of the candidate offsets. All the candidate results may be displayed, or the algorithm may choose from among them according to some criterion (for instance, a minimal dispersion of ICP estimates, or to keep the estimates within a physiologic range). When all candidate

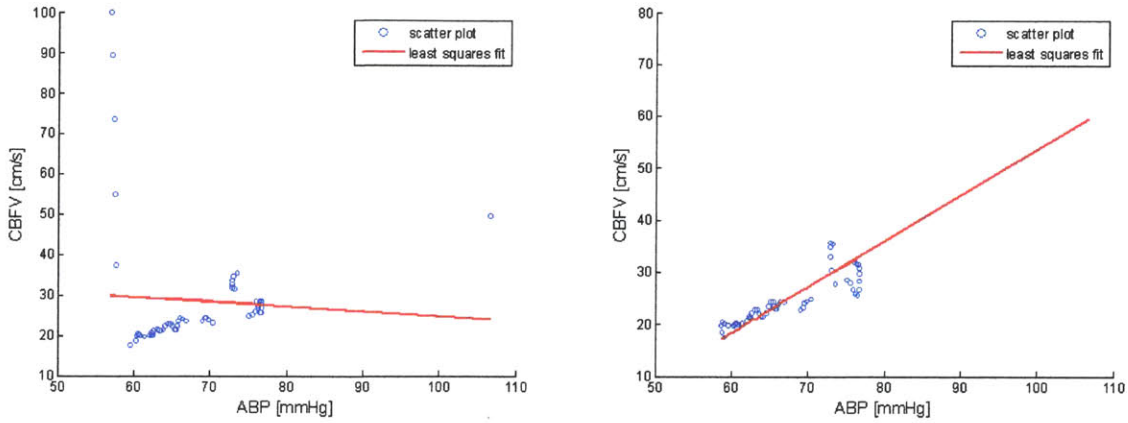

Figure 5-3: A method for the phase-offset estimation: various candidate phase-offsets are applied until a linear model well approximates the relation between CBFV and the shifted ABP (at the selected low-$\frac{dp_a(t)}{dt}$ points in a cardiac cycle). The left panel shows the case of an offset for which a linear model has a large residual error, while the right panel shows the case of an offset for which a line is a good fit to the data.

ICP estimates appear plausible, we compute their arithmetic average and report a single estimate.

5.4 Summary of Estimation Algorithm

Summarizing all the processing steps, Figure 5-4 provides a flow chart of the overall estimation set up. The algorithm processes clinical measurements of ABP and CBFV and provides beat-by-beat estimates of R, C, ICP, and thus CPP for the entire duration of recording of the input waveforms. It is evident from the description of the estimation algorithm that the computational and memory requirements are modest enough to run the algorithm in real-time.

5.4.1 Utilizing input signal quality in estimation algorithm

The estimation algorithm runs a check on the input data within each estimation window, to determine if the signal quality is good enough to carry out the estimation. It keeps track of the signal-quality labels assigned in the pre-processing stage and applies certain logic to form a signal quality index for the given window of data. If

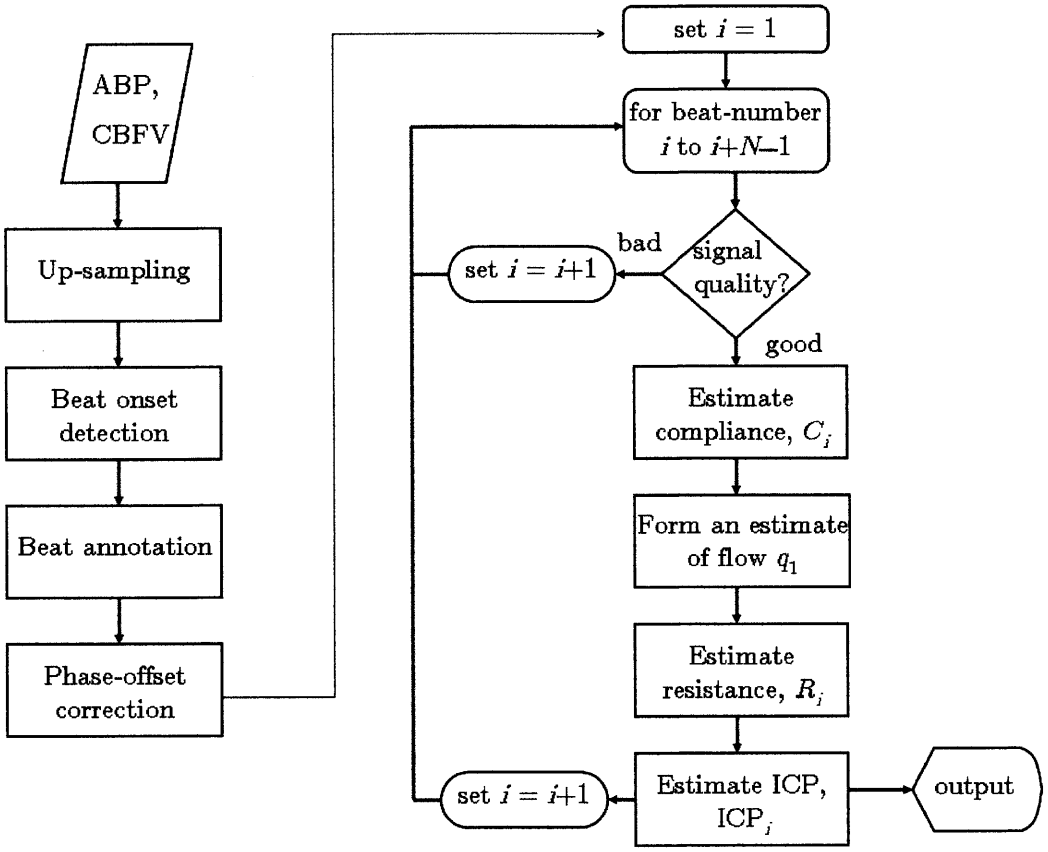

Figure 5-4: A flow-chart description of the estimation algorithm and pre-processing steps. An optional step of low-pass filtering the input waveforms is added in cases where significant high-frequency noise is present.

the labels indicate a signal-break or loss of data (e.g., due to mal-positioning of the radial artery catheter or intermittent calibration) or artifact, the estimates are not computed during that interval. Else, it performs a majority vote based on the labels of the input data, and carries out the estimation steps if at least half the beats have a 'good' label. A signal quality index proportional to the percentage of good beats is formed as an output, which may be displayed as an indicator of reliability of the estimates.

5.5 Key Features of Estimation Approach

Certain features of our approach distinguish it from previous work on non-invasive ICP estimation. Furthermore, some processing aspects are unique to our analysis of the given waveforms. We summarize them below.

- **Model-based estimation:** Our ICP estimate is obtained by processing clinical measurements using the dynamic constraints provided by a mechanistic model of cerebrovascular physiology. The model parameters are physiologically meaningful and the dynamic relationships are guided by the relevant physiology, rather than extracted by any method of learning from observed data. The model does not need any training or *a priori* determination of parameter values.

- **Calibration-free and patient-specific:** The estimation algorithm does not need any calibration data. It produces patient-specific estimates from the ABP and CBFV measurements. Furthermore, the algorithm does not perform any learning within the patient record, beyond its own estimation window (usually 10-60 beats).

- **Immunity against discrepancies in TCD measurements:** Our approach utilizes TCD-based measurements of CBFV as an input signal for computing the ICP estimate. The TCD technology has faced criticism that its measurements do not accurately represent CBF in the insonated artery. First, TCD measures flow velocity. Because the cross-sectional area of the MCA is not known, conversion from velocity to flow is not determined. Secondly, the measurements of velocity are scaled by the cosine of the insonation angle between the Doppler transducer and flow velocity vector. These sources of error are surely important if the goal is to measure CBF. However, as we showed above, our ICP estimates are unaffected as long as the TCD measurements provide a signal proportional to CBF. Discrepancy in translating CBFV to CBF, as well other inaccuracies in the TCD technology that result in multiplicative factors do not affect our ICP estimate. While the estimates of resistance and compliance are scaled re-

ciprocally by such multiplicative factors, their dynamic variations can still be used to form an assessment of autoregulation.

- **Intrabeat analysis:** An important characteristic of our approach is the use of both intrabeat and beat-to-beat features of the measured waveforms to obtain robust estimates of our model parameters. This approach is analogous to what is more routinely done in the setting of cardiac output estimation, where models such as the Windkessel are used to relate arterial pulse morphology and beat-to-beat variations to model parameters [130]. Such an approach is rather lacking in the literature on cerebrovascular dynamics, though our results suggest that a payoff is eminently achievable.

- **Time-synchronized processing of ABP and CBFV:** We have not yet seen any other work that performs time-synchronized analysis of ABP and CBFV measurements. Similarly, to the best of our knowledge, extracting morphological information from the TCD signal has not been reported before. We hope our work prompts further development in TCD technology to provide waveforms at higher amplitude resolution and sampling frequency to facilitate intrabeat morphological analysis.

5.6 Concluding Remarks

In this chapter we described the processing of the time-synchronized measurements of radial ABP and TCD-based CBFV waveforms using our reduced model, to provide beat-by-beat estimates of ICP, cerebrovascular resistance and compliance. At the heart of the computation lies our two-step algorithm that exploits intrabeat variability in the waveforms to compute robust estimates of the model parameters. Preprocessing of the input waveforms and phase-offset correction for the radial ABP are also specified. We analyzed the effect of discrepancy in TCD measurements of CBF, and concluded that the ICP estimates are independent of a constant scaling of CBF.

Part III

Validation and Performance Analysis

Chapter 6

ICP Estimation Performance

We described our ICP estimation algorithm in the previous chapter. Here, we report on its performance by comparing its estimates against invasively measured ICP. Validation of our ICP estimation algorithm requires access to both the required input measurements and (invasively obtained) reference ICP measurements, all in a time-synchronized manner. It is important to point out, however, that information from the invasive ICP measurements is *not* being fed into our estimation algorithm in any manner, to tune parameters or provide calibration or improve prediction. The parameters in our algorithm are determined directly from the ABP and CBFV measurements, and are set in a patient-specific, calibration-free way. We use invasive ICP *only* for validation of our method.

In this chapter we apply our method on data obtained from severe TBI patients. In addition to plotting the time-series of estimates against the invasive measurements, we also compute various statistical measures of estimation performance, including root-mean-squared error and Bland-Altman analysis, to gauge agreement between the non-invasive estimates and invasive measurements. Finally, we discuss the various possible causes of dispersion and bias in the estimates.

In Section 6.1 we describe the patient data used for validation of our method. Section 6.2 provides the ICP estimation results, their comparison against the measured ICP, and the associated error analysis. In Section 6.3, we discuss the extent to

which the accuracy of our estimates falls in the clinically acceptable range, and we explore error trends as a function of the input ABP and CBFV measurements. We also analyze the degree of concordance between estimates from right and left-sided TCD measurements. The last section describes the possible sources of error in the estimates.

6.1 Validation Data

For validation of our approach, we needed to compare our non-invasive ICP estimates against invasive measurements. The validation data were collected (as part of a data collection effort spanning several years) at Addenbrooke's Hospital, University of Cambridge, UK, and kindly made available to us by Dr. Marek Czosnyka. Each patient record consists of simultaneous and continuous recordings of bilateral CBFV via TCD ultrasound, radial ABP via an intra-arterial catheter, and ICP via an indwelling parenchymal probe. For the validation presented here, we analyzed 45 records from patients with severe TBI (mostly closed-head injuries). The recordings were obtained over a continuous stretch of time that varied from 10 minutes to 4 hours. We used a total of about 35 hours of recorded data or more than 150,000 cardiac beats. All three signals (ABP, CBFV and invasive ICP) were recorded in a time-synchronized manner and sampled at the same sampling frequency. However, the sampling frequency for data from different patients varied between 20 and 70 Hz. Other patient information, including age, gender, Glasgow Coma Scale (GCS) score, and Glasgow Outcome Score (GOS), were also provided.

The subjects included 33 male and 12 female patients with a median age of 29 years, a median GCS score of 5 (indicating severe TBI on admission), and GOS in the range of 1-5, with a median of 2 (indicating very poor outcome six months after admission). Seventeen of the 45 patients died within 6 months after the initial hospitalization. In 5 patients, injury led to severe disability, and 16 patients lived with only moderate disability. Only 6 patients had a good outcome. The outcome score was not available in one case.

When running our estimation algorithm, we only used the ABP and CBFV measurements, i.e., we were blinded to the invasively measured ICP. This 'ICP-blind' analysis of the input waveforms provided our ICP estimates for all 45 patient records. In fact, in 35 patient records, the measured ICP waveforms were revealed to us only after the estimates were computed using the ABP and CBFV signals. In an initial set of 10 patient records, ABP, CBFV and ICP were available simultaneously, which allowed some initial exploration and orientation to the data. However, no parameters from this exploratory phase were carried over into our later studies. The estimation results presented here were obtained in an 'ICP-blind' manner for the initial set of 10 records as well.

6.2 ICP Estimates and Error Statistics

We applied our estimation algorithm to the ABP and CBFV waveforms of the 45 patient records, and computed continuous (beat-by-beat) non-invasive ICP estimates (nICP) for each case. To assess the quality of fit for each patient record, we compute the root-mean-squared error (RMSE) as

$$\mathrm{RMSE} = \sqrt{\frac{1}{N}\sum_{i=1}^{N}\left(\mathrm{nICP}(i) - \mathrm{ICP}(i)\right)^2}, \tag{6.1}$$

where N is the total number of estimates in the patient record.

Bland-Altman analysis is a standard approach for comparing two methods for measuring the same quantity [131, 132]. It is based on a plot of the difference of (or error between) the measurements made by the two methods against their average. The sample mean of the error is indicated as the bias. The limits of agreement, which delineate a 95% confidence interval on the error, are drawn by assuming the error to be normally distributed and are therefore at about twice the (sample) standard deviation of error (SDE) on either side of the bias level. In addition to the conventional Bland-Altman plot, we add a histogram of the error on the vertical axis.

It is worth noting the connection between the RMSE in (6.1) and the bias and

SDE used in the Bland-Altman plot. Let $b = \frac{1}{N}\sum_{i=1}^{N}(\text{nICP}(i) - \text{ICP}(i))$ denote the sample mean error or bias, and s^2 denote the sample variance of the error around this sample mean. Then the quantity under the square-root sign in (6.1) can be re-written as $(b^2 + s^2)$, so RMSE $= \sqrt{b^2 + s^2}$. The number thus serves as a useful aggregate summary of the more detailed information contained in the Bland-Altman plot.

6.2.1 Comparison of beat-by-beat estimates

Continuous estimates of ICP allow us to compare nICP and ICP on a beat-by-beat basis. We are particularly interested in the estimation performance when the underlying ICP goes through dynamics changes. In this subsection we present a collection of representative results, to convey a general sense of the performance of our estimation algorithm. A fuller summary is given in the next subsection.

Figure 6-1 shows a comparison of beat-by-beat estimates in three examples. The first row in Figure 6-1 shows a case of severe progressive intracranial hypertension in a 30-year old male, with GCS = 3, and GOS = 5 (the patient did not survive). The mean ICP increased from 60 mmHg to 120 mmHg over the course of an hour[1]. (MAP in this patient also rose steadily from about 125 mmHg at the beginning to 145 mmHg during this interval, so the lowest CPP was still about 45 mmHg, despite the extraordinarily high ICP.) The nICP estimates remain close to the measured ICP and closely track the slow upward trend. The total RMSE in this patient is 6.5 mmHg. A Bland-Altman plot and the histogram of error are also shown, and indicate a bias of -5.7 mmHg, and an SDE of only 3 mmHg.

The second row in Figure 6-1 shows a case in which the patient's ICP displays plateau waves — a phenomenon characterized by rapid increase in ICP, generally above 20 mmHg, followed by a relatively stable period of high ICP for at least 5 minutes, and then a spontaneous drop to a lower level [75, 133, 134]. The subject is a 17-year old female with GCS = 5, and GOS = 5. Over the duration of about 100

[1]Recall from Chapter 2 that normal ICP ranges between 7-15 mmHg, and that aggressive treatment is indicated if ICP exceeds 20-25 mmHg.

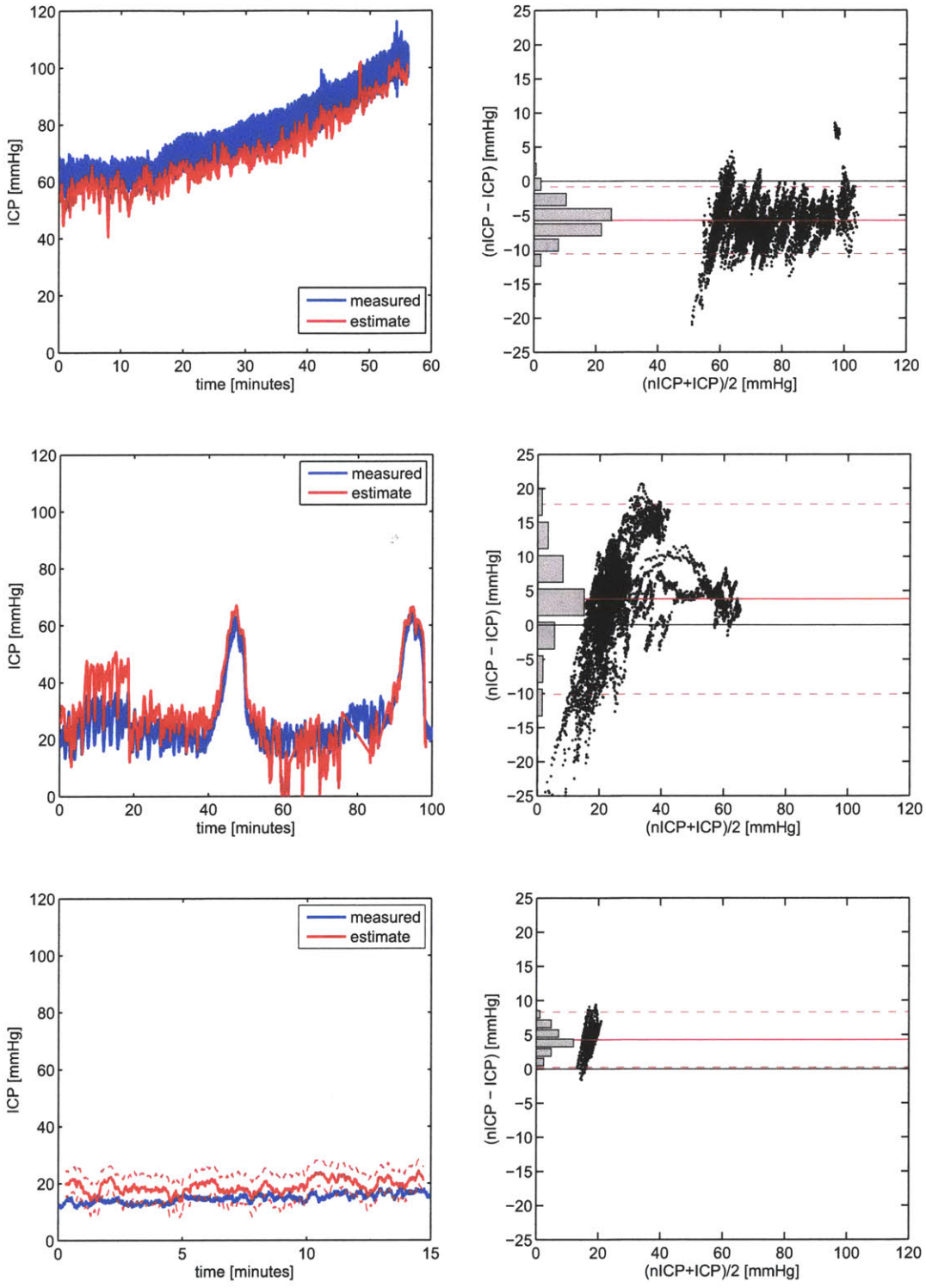

Figure 6-1: Comparison of nICP (red) and the invasively measured ICP (blue) in three patients. The left panel in each case shows beat-by-beat ICP and nICP; the right panel shows the corresponding Bland-Altman plot, to assess agreement between the two methods.

minutes, nICP tracks the transient ICP changes quite well. The RMSE in this record is 8 mmHg. Bland-Altman analysis reveals a bias of 3.8 mmHg and SDE of 7 mmHg. While significant dispersions exist in nICP, the sharp transitions in ICP are captured exceedingly well, both in duration and amplitude.

The last row in Figure 6-1 shows a 15-minute recording of normal ICP in a 32-year old female (GCS = 1, and GOS = 2). Our nICP estimate tracks the actual measurement reasonably well in the normal range. The RMSE is 4.7 mmHg, bias is 4.3 mmHg, and SDE is 2 mmHg. In Figure 6-1(c), we also show two thin traces, one below and one above the nICP. Each of these is the nICP estimate corresponding to a candidate phase (or timing) offset between the measured radial ABP and the required ABP at the MCA. Our phase-offset determination (see Section 5.3) in this case identifies two candidate offsets, and the estimation algorithm computes nICP for each of the candidates. The nICP estimate shown in the red (darker line) is actually the point-by-point average of the two candidate estimates.

One estimate every 60 beats

Our estimates are computed for each cardiac beat, which allows us to compare nICP and ICP for every beat. However, most clinical applications only require ICP every few minutes or at most every few beats. Therefore, we can report an ICP estimate after several cardiac beats or minutes by averaging our beat-by-beat estimates over appropriate window sizes. Such averaging may also be expected promises to reduce part of the dispersion between ICP estimates and measurements, in particular those that stem from respiratory modulation of ICP. In the following, we perform a comparison of nICP and ICP by taking averages over non-overlapping 60-beat windows, which is equivalent to averaging over slightly less than a minute in most cases.

Three examples of 60-beat averages of nICP and ICP are shown in Figure 6-2. (We take this as an opportunity to compare nICP estimates in patients different from those yielding the estimates presented above.) The first row in Figure 6-2 shows a plateau wave in a 15-minute recording for a 23-year old male subject (GCS = 7, and GOS = 5). Our nICP tracks the transients in ICP closely. The RMSE is 5.4 mmHg.

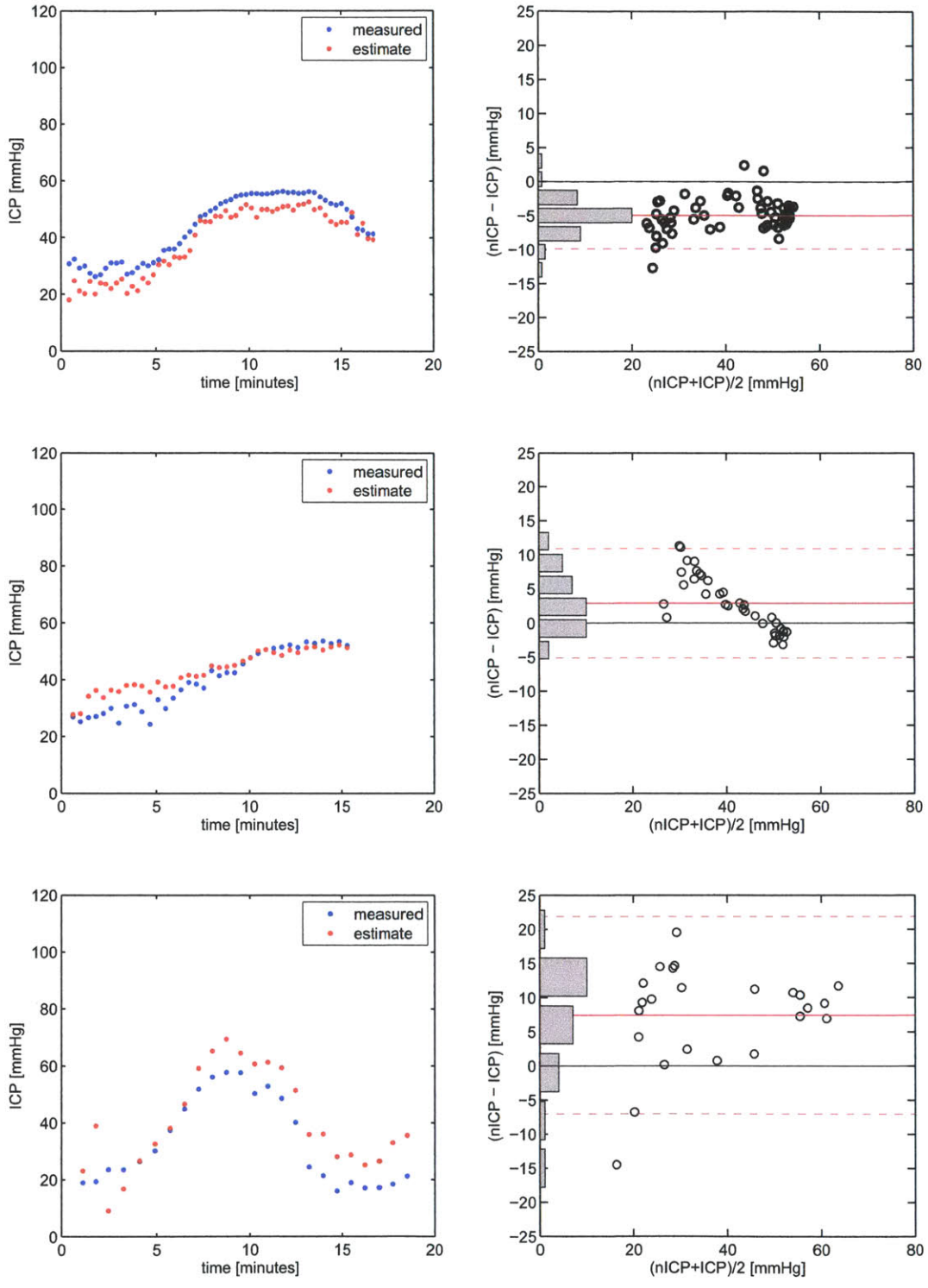

Figure 6-2: For clinical monitoring, an ICP estimate every 50-100 beats sufficiently meets the clinical monitoring needs. The comparison in this figure plots ICP (blue) and nICP (red) only every 60 beats. The left panels show ICP and nICP. The right panels show the corresponding Bland-Altman plots to assess the level of agreement between the two methods.

The Bland-Altman analysis is also shown, and reveals a bias of -4.9 mmHg and SDE of 2.2 mmHg. The second row in Figure 6-2 shows a comparison in a case of slowly increasing ICP in a 17-year old female (GCS = 4, and GOS = 3). The recorded ICP gradually increases from a level of about 30 mmHg to about 60 mmHg. The RMSE is 4.9 mmHg, the bias is 2.9 mmHg, and the SDE is 4 mmHg. Another such example is shown in the third row in Figure 6-2 for a 17-year old female with GCS = 5, and GOS = 5 (death within six months after hospitalization).

The six patient records shown as examples in this subsection demonstrate the generally good performance of nICP in tracking trends and sharp transients in invasively measured ICP.

Two extreme examples

In the above six examples we compared nICP and ICP in individual records and analyzed the estimation error. These are representative cases from the available pool of 45 patient records, and are selected to show a range of ICP variations from the database (low or normal ICP, high ICP, abrupt variations, and both short and long recording durations). To round out the examples, we now include beat-by-beat comparison for two more patient records, the first being the worst of all nICP estimates and the second a representative case of very good estimation performance. Figure 6-3(a) shows an example (37-year old male, GCS = 12 and GOS = 1) where nICP is quite far away from the measured ICP; the bias is about 22 mmHg. Possible reasons for this level of discrepancy are considered in Section 6.3.3. On the other hand, Figure 6-3(b) shows a case (16-year old male, GCS = 5 and GOS = 5) of very good estimation performance; the bias is only about 1.5 mmHg and SDE is about 3.5 mmHg. Visual inspection reveals that the estimation performance is quite remarkable.

6.2.2 Comparing independent estimates across all records

In this section we choose to analyze the nICP estimation error in a manner which makes the statistics more meaningful, though it is not how a clinical test of accuracy

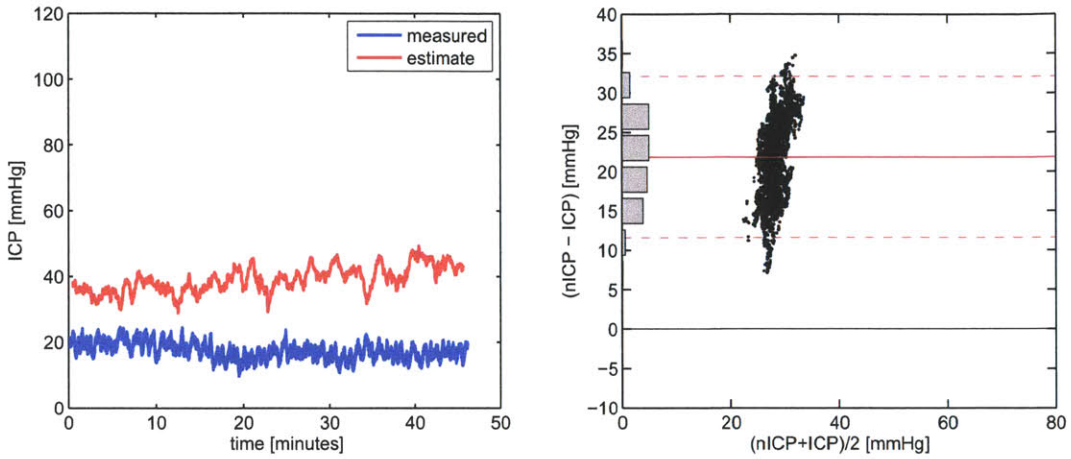

(a) A case of worst ICP estimation performance in a 37-year old male subject.

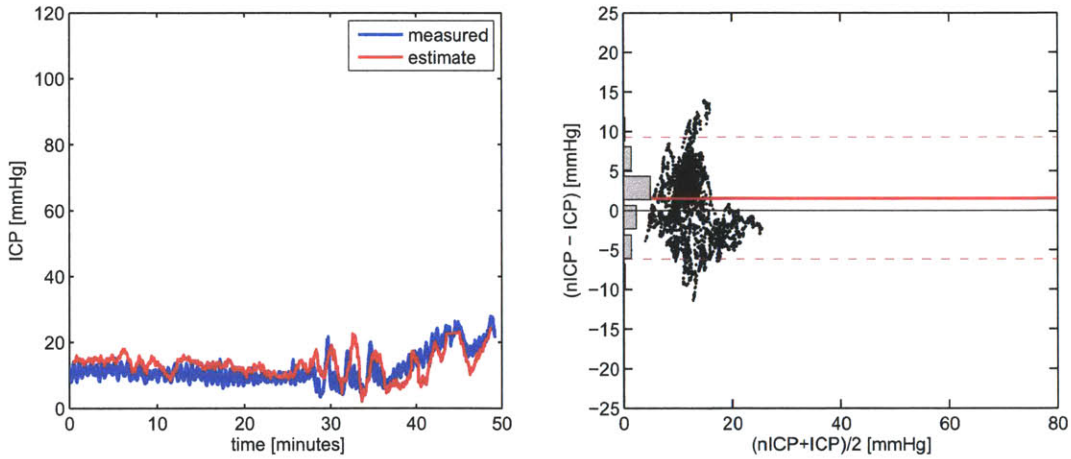

(b) ICP estimate tracks the measured ICP closely in a case of 16-year old male subject.

Figure 6-3: Examples representing two extreme cases of estimation performance, comparing nICP (red) and the invasively measured ICP (blue). The top row shows a case of poor estimation performance. The bottom row presents a case of very good ICP estimation, which picks up even small variations in the underlying ICP as well as tracking the baseline ICP. The left panels show beat-by-beat ICP and nICP. The right panels show Bland-Altman plots to assess agreement between the two methods.

will be designed as the estimates do not have to be independent of each other. We summarize the performance of our estimation algorithm over all the patient data that we have analyzed by comparing only the nICP values that are independent of each other. For that purpose, we selected nICP values that are estimated over non-overlapping windows of 60 beats, and compared with the measured ICP averaged over the same windows. This yields a total of 3,529 points across all 45 patient records (out of about 150,000 total estimates). The Bland-Altman plot in Figure 6-4 shows that all pooled independent estimates have a bias of 2 mmHg, and an SDE of about 9 mmHg. Although the computation of statistical means and variances is made easier by our self-imposed condition of independence of nICP values, it makes the estimation error go up, and clinical application of the method will not require the estimates to be independent.

A further averaging of the above independent estimates over 10-point, non-overlapping windows yields 353 independent comparisons, corresponding to an estimate over 600

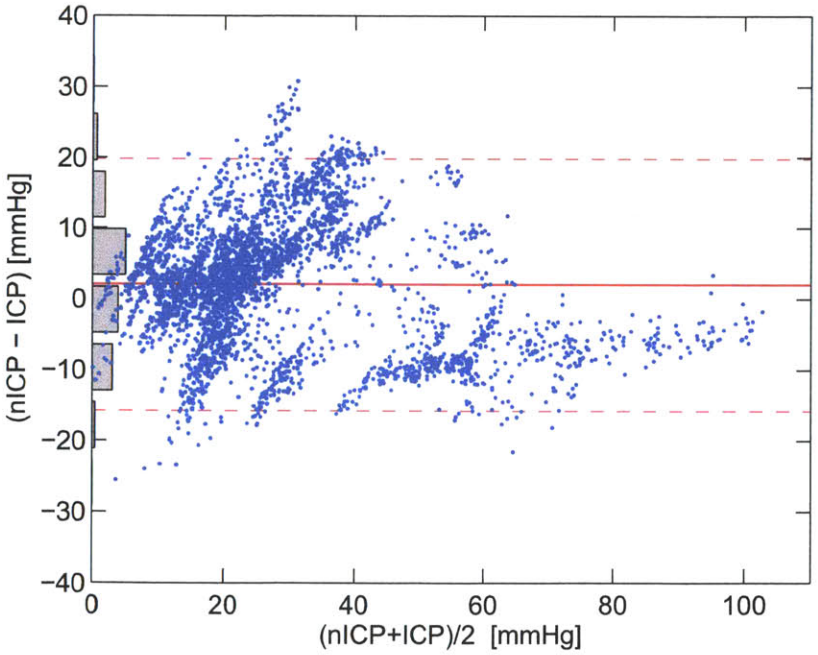

Figure 6-4: Bland-Altman plot of all 3,529 independently obtained estimates, each over a distinct 60-beat window. The bias is 2 mmHg, and standard deviation of error is 9 mmHg.

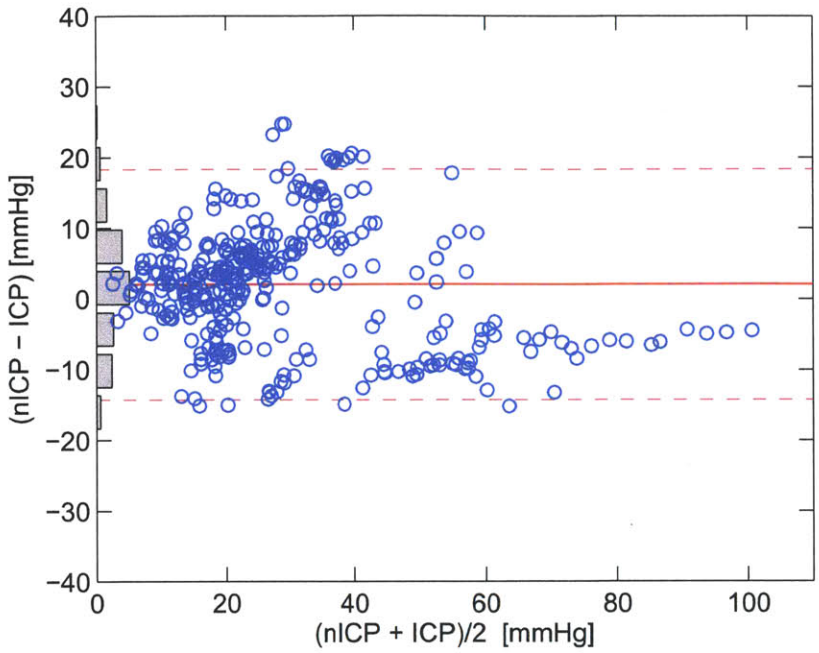

Figure 6-5: Bland-Altman plot of 10-point average of independent estimates, providing one comparison for each 600-beat window, hence 353 points total. The bias is 2 mmHg, and standard deviation of error is 8.2 mmHg.

beats, or about every 6-9 minutes in most patient records. The Bland-Altman analysis of the estimation error is shown in Figure 6-5. The bias remains unchanged while the SDE reduces to 8.2 mmHg.

For yet a more condensed set of comparisons, we compute the time-averages of measured ICP and of estimated nICP over each entire patient record, generating a single comparison for each patient, and a total of 45 comparisons. A Bland-Altman plot for the 45 points is shown in Figure 6-6. The overall bias is 1.8 mmHg, and SDE is 6.8 mmHg. The absolute error is less than 6 mmHg in 33 records (73%), less than 10 mmHg in 39 records (87%), and less than 15 mmHg in 44 subjects. As can be seen in Figure 6-6, one patient record has a large positive error, with a bias of about 22 mmHg. If we exclude this case and re-calculate the error statistics, the bias reduces to 0.9 mmHg and the SDE is 6 mmHg. The outlier is the same patient record that we discussed in Figure 6-3(a).

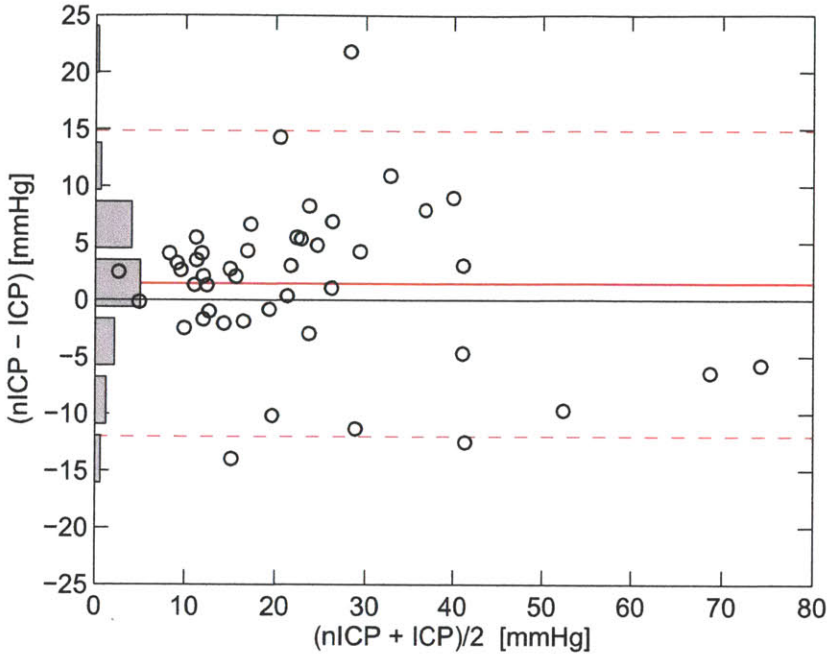

Figure 6-6: Bland-Altman plot of error between respective time-averages of measured ICP and nICP estimates; the bias is 1.8 mmHg and standard deviation of error is 6.8 mmHg.

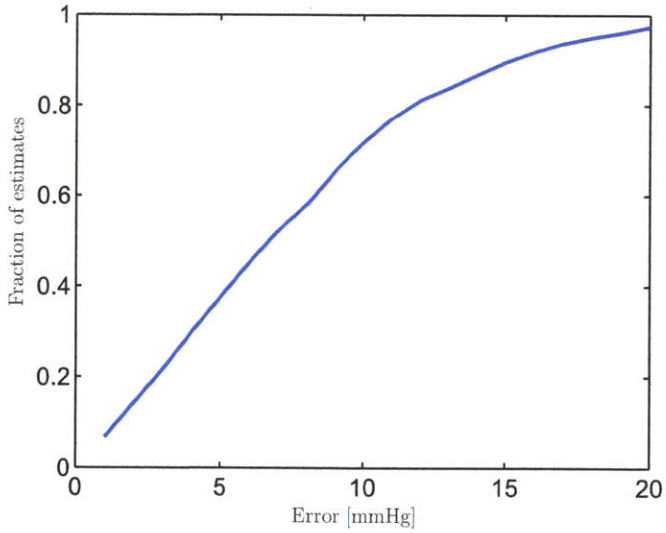

Figure 6-7: Cumulative distribution of number of independent estimates as a function of absolute estimation error $|\text{nICP} - \text{ICP}|$. About 80% estimates have an absolute error less than 10 mmHg. However, requiring nICP estimates to be independent is unnecessarily stringent; see text for detail.

Number of independent estimates with error below a certain threshold

To obtain another view of the performance of estimation, we construct a cumulative distribution showing the fraction of the 3,529 independent estimates with absolute error less than a specified threshold, see Figure 6-7. About 80% estimates have an absolute error less than 10 mmHg. An estimation error of 5 to 6 mmHg (or higher) can be critical at an ICP level around 15 mmHg, as the threshold for intracranial hypertension is at about 20 mmHg; an ICP above 20-25 mmHg calls for an immediate intervention. Therefore, ideally we would like to see the error to be less than 6 mmHg for about 90% of our estimates. There are several factors that contribute to the error in estimates, as we discuss in Section 6.3.3.

6.2.3 Correlation analysis of ICP estimation error

Having compared nICP against ICP in a number of ways, we want to assess whether the estimates are systematically influenced by other physiological variables. Figure 6-8 shows a scatter plot of ICP estimation error against the average of measured and estimated ICP, for all 3,529 independent data windows used in earlier plots. A least-squares linear fit between them is also superimposed. The slope of this line is -0.09 ± 0.02, and the R^2-statistic is equal to 0.032. This analysis indicates that the linear model has a large residual error and is therefore a poor fit to the data. No significant relationship is evident between the estimation error and mean ICP.

Figure 6-9 shows a scatter plot of estimation error against the mean arterial blood pressure (MAP) values for all independent estimates across all patient records (3,529 points). A least-squares linear fit between the estimation error and MAP is also superimposed. The slope of this line is -0.13 ± 0.02, and the R^2-statistic is equal to 0.048, which again indicates a poor fit of the data by the line. The predictive value of the linear model is therefore quite low. Regressions of the estimation error against diastolic and systolic ABP provided similar results.

A further analysis is performed for ICP estimation error against mean CBFV. Figure 6-10 shows the scatter plot and the best-fit least-squares line. The slope of this line is -0.07 ± 0.01 mmHg/(cm/s), and the R^2-statistic is equal to 0.047,

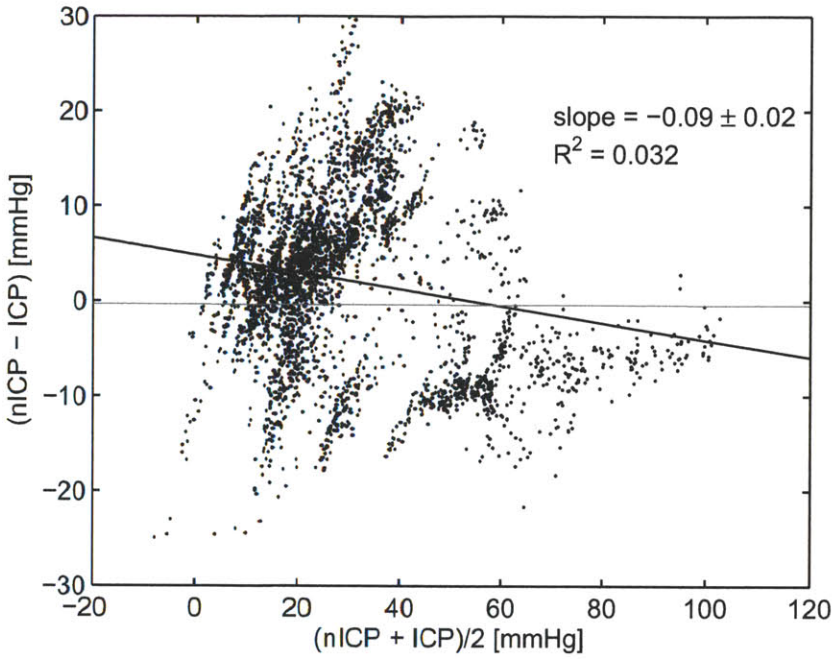

Figure 6-8: A linear model between average ICP and the estimation error has poor predictive value, as $R^2 = 0.032$ and the slope of the least-squares line is -0.09.

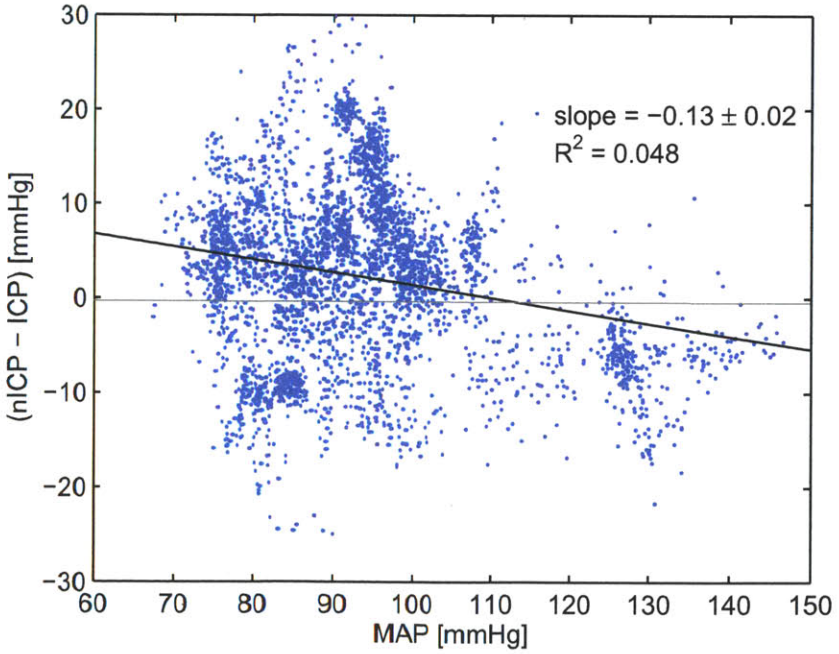

Figure 6-9: Exploring correlation between ICP estimation error and MAP: the scatter plot and best linear fit of the data indicate that error has no significant relationship with MAP.

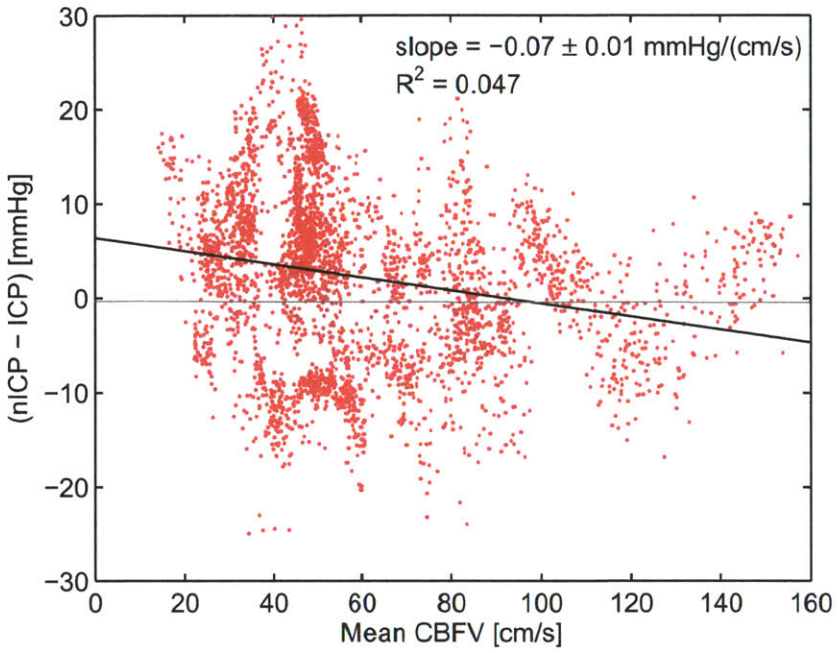

Figure 6-10: Exploring correlation between ICP estimation error and mean CBFV: the scatter plot and best linear fit of the data indicate that error has no significant relationship with mean CBFV.

indicating — once again — a large residual error and a poor fit of the data by the linear model. The analysis shows no significant relationship between the estimation error and mean CBFV.

Our overall impression from this set of regression studies is that the reduced dynamic model we have employed in our estimation algorithm has largely captured the dependence of ICP on ABP and CBFV, at least in the sense that the estimation residual does not display any significant correlation with ABP and CBFV.

6.2.4 Estimates using bilateral TCD

In the majority of the patient records available to us, bilateral TCD measurements were made and CBFV waveforms for both the left and right sides were recorded. Our ICP estimation algorithm needs and uses only one of the CBFV measurements, as ICP is expected to be uniform across left and right hemispheres. The estimation results presented above are obtained using CBFV data from one side only (left-side, for the

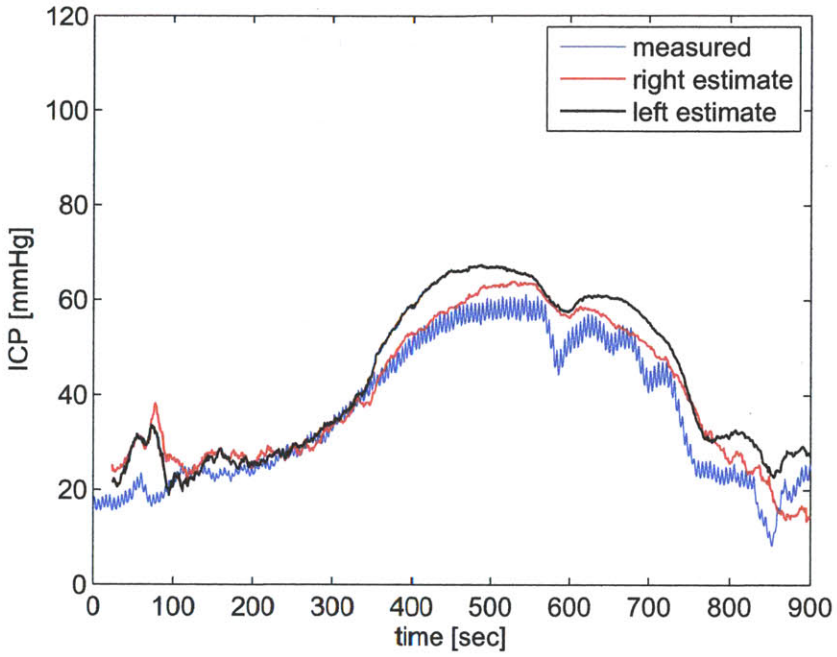

Figure 6-11: Left (blue) and right (red) nICP estimates obtained from the bilateral TCD measurements: estimates from the two sides generally agree within a close range. The invasively measured ICP (green) is also shown as a reference.

sake of consistency). However, to test the reliability of our ICP estimation method, we can compute the left and right-sided ICP estimates using CBFV measured from the corresponding side in each patient (with the same ABP measurement used in both computations). The representative results in Figure 6-11 for a particular patient show the left and right ICP estimates agreeing well in their time course, both tracking the trends in the underlying ICP quite remarkably, though they differ slightly near the end of the rise in ICP, between 300 and 400 seconds but lock with each other again. (A similar difference is seen for about 100 seconds when the ICP starts to decline.) This example aptly sums up our observations in the overall analysis of the patient records, where bilateral nICP estimates could be computed. In almost all cases in which CBFV measurements from the left and right are of comparable signal quality, the estimates from the two sides are consistent, contain the same dynamic trends and variations, and are within a 4-5 mmHg of each other.

6.3 Discussion

The above comparisons show that our non-invasive estimates of ICP track the invasive measurements of ICP rather well. The estimates are obtained continuously, as frequently as one for each cardiac beat of the input waveforms, which is desirable for continuous monitoring. The bias in the estimates is very low, and the associated standard deviation of error is around 8 mmHg. The natural question now is whether this estimation performance is adequate for clinical application.

6.3.1 What is acceptable clinical accuracy?

The question of acceptable clinical accuracy does not have a simple answer. Even though one might wish to have a very small tolerance limit for the error, the actual requirement is rather loose. For example, respiration-induced rhythmic oscillations in mean ICP are typically 3-4 mmHg. Therefore, any deviation of less than 4 mmHg between mean ICP measurement and an estimate is not particularly significant. However, even invasively obtained ICP measurements in current practice are less accurate than that.

As discussed earlier in Section 3.1, the ventricular catheter with external calibration is the most accurate method of ICP measurement and is considered the clinical 'gold standard', though it is not without problems [29]. Certain ventricular measurement devices cannot be calibrated *in vivo* and may encounter drift. For example, the Camino (Camino Laboratories, San Diego, CA) catheter-tip transducer has a reported drift of 3 mmHg over a 24-hour period [79]. Parenchymal sensor probes have been a very popular choice for ICP monitoring. The popular Codman MicroSensor (Codman and Shurtleff Inc., Raynham, MA) has a maximum absolute error of 6 mmHg [80] when tested in a laboratory setting to measure the pressure of a water column. When used for continuous measurement, this device has a maximum drift of about 2 mmHg in 24 hours, and a total drift of 4 mmHg over several days [80]. Another device for parenchymal measurement of ICP is the Spiegelberg transducer

(B Braun Ltd.), which has the unique capability to automatically re-calibrate itself at regular intervals to improve its measurement accuracy. Comparison of parenchymal measurement of ICP by the Spiegelberg device against ventricular measurements showed that a 96% agreement limit of the two methods is ± 10 mmHg [81].

Simultaneous measurements by two parenchymal sensors in the same brain can show large differences. In a study by Banister *et al.*, comparing Camino and Codman MicroSensor devices, good agreement was observed between the two probe readings in 11 out of 17 patients, and 99% of the 'good' measurements were within an absolute difference of 10 mmHg [77]. However, in the remaining 6 patients 40% of the comparisons had absolute errors larger than 10 mmHg, and differences in excess of 15 mmHg were also observed.

Other invasive methods such as the subdural bolt are even less accurate, particularly when they are blocked, and tend to underestimate ICP [78]. ICP measurements in the subarachnoid and epidural spaces have also been shown to contain significant error [82, 83]. Comparison of simultaneous measurements via epidural and parenchymal (or ventricular) sensors reveal a difference of 10 mmHg or larger for at least 10 minutes in 33% cases [82, 83]. In an investigation focused only on hydrocephalus cases, subarachnoid measurements of ICP were found to have misleading measurements, reading below 15 mmHg when the intracranial conditions indicated a high pressure [78]. By measuring ICP much closer to the region of CSF reabsorption rather than generation, these devices will read lower than ventricular ICP, because of the pressure drop associated with CSF circulation.

Noting that these invasive devices, currently widely used in practice, have apparently significant measurement errors, one wonders if what is accepted should define what is clinically acceptable. Ideally, an acceptable error should be based on physiological variability of ICP and the thresholds for clinical decision-making. From this viewpoint, an error tolerance of at most 4-5 mmHg may seem to be acceptable.

6.3.2 Estimation accuracy

Comparison of our ICP estimates against the tolerances quoted above indicates that our estimates appear reasonably close to the clinically accepted methods. Given that the difference between simultaneous measurement by two parenchymal probes can range as high as 10 mmHg (or even higher), our estimates in fact track parenchymal ICP quite well. As noted earlier, 39 out of 45 estimates (time-averaged over each entire patient record) have an absolute error less than 10 mmHg with our estimation algorithm.

Although our ICP estimates have an error comparable to the deviation in parenchymal probes, the 'gold standard' method is intraventricular measurement of ICP. Our method does not yet show the accuracy range of 4-5 mmHg associated with such measurement. However, the low bias and generally remarkable tracking of sharp trends in measured ICP by our nICP estimates are quite striking. Our approach offers promise for improvement performance if we can address the sources of error in the estimates and reduce the standard deviation of error by a half. These sources of error are discussed next.

6.3.3 Sources of error in our nICP estimation

Several sources contribute to performance degradation of our nICP estimates, and we describe the major ones below.

- **Discrepancy in ABP:** Our algorithm uses radial measurements of ABP, in place of cerebral ABP, applying an estimated phase-offset to synchronize the peripheral ABP measurements with the CBFV measurements at the MCA. An estimation error in phase offset causes significant bias in the ICP estimates. Furthermore, differences in the morphology of the ABP waveforms measured at a radial artery and those at the middle cerebral artery are not compensated in our estimation algorithm and may have some effect on estimation performance.

- **Issues with TCD signal:** As noted earlier, our ICP estimate is independent of any constant scaling of CBF, which justified our directly using CBFV

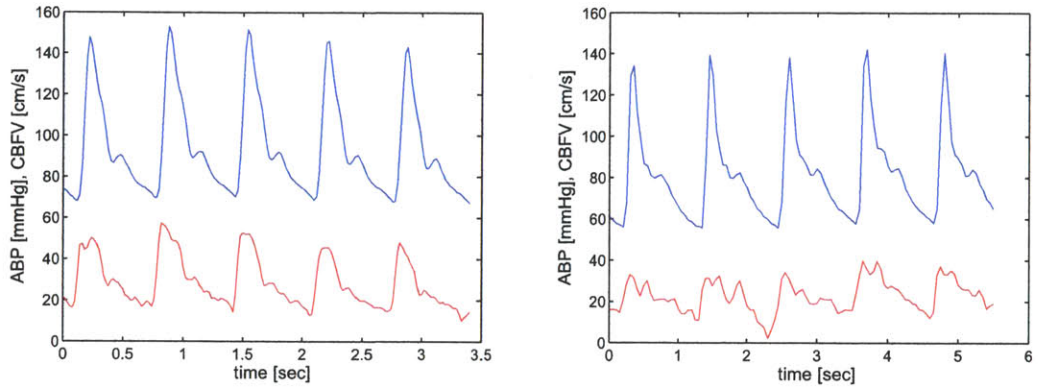

(a) Example of relatively good signal quality.

(b) Example of poor signal quality.

Figure 6-12: Signal quality of the recorded ABP (blue) and CBFV (red) waveforms varied across patient data. Both sampling frequency and amplitude resolution have a significant effect on the intrabeat analysis performed in our estimation algorithm.

measurements as a proxy for CBF. However, if scaling factors, such as the cross-sectional area of the MCA or the angle of insonation vary quickly *within* the estimation window, the ICP estimate will be affected. In addition, artifacts in TCD measurements are reflected in the ICP estimates. For example, dispersion and quantization errors in the TCD signal cause the intra-beat analysis to be noisy, and result in large beat-to-beat dispersion. In our analysis we noted that the ABP waveforms had a smoother beat morphology than the TCD waveforms, as the latter were often contaminated by abrupt variations. These quantization effects and dispersion in the CBFV waveform are a major source of dispersion in the ICP estimates. A comparison of relatively good-quality and poor-quality TCD waveforms is shown in Figure 6-12. Even though the signal quality in the left panel is less than optimal for extracting the morphological features required by our estimation algorithm, the CBFV waveform at least has the expected time-course. In the right panel, we see how artifact, and possibly a shallow insonation angle, can lead to unphysiological CBFV waveforms. In our experience, patient records with better TCD signal quality produce ICP estimates with less fluctuations and smaller variance. The quality of the TCD signal may be the reason why TCD measurements have received little attention

in the literature for detailed intrabeat analysis of the kind that our algorithm performs. Improvements in this technology can lead to better morphological analysis and reduce the variance of ICP estimates, and we are optimistic that such improvements will come (particularly if manufacturers recognize that there is value in better capture of the intrabeat flow morphology).

- **Sampling frequency:** Since we employ time-domain analysis of the ABP and CBFV waveforms to extract morphological features and their variations, the sampling rate of the waveforms has a direct impact on performance. It determines, for example, the timing jitter in the discrete-time indices for beat-onset detection and for extracting such features as end-diastolic and systolic times. A low sampling rate adds more noise to these marker locations and introduces both bias and dispersion in the estimates. The estimation performance is expected to improve by increasing the sampling rate to 125-200 Hz. Again, it is quite reasonable to expect TCD instrumentation to move in this direction. Returning to Figure 6-12, we note that the left panel shows a comparatively better quality signal, but even here the ABP waveform exhibits rather sharp artifacts (piece-wise linear segments) during systole, indicating that the sampling frequency is too low for the corresponding heart rate. This problem is exacerbated in the waveforms shown in right panel. Low sampling frequency makes the extraction of the intrabeat features challenging, and leads to higher dispersion in the final ICP estimates. We believe that state-of-the-art data-acquisition technology will allow us to collect data at much higher fidelity than what was available in the data we used.

- **Signal quality:** Estimation performance depends directly on the input signal quality. Signal quality depends on noise and other artifact in the waveforms. Noise in the measurements degrades the estimation performance, e.g., it makes the approximation of the derivative in (5.4) poorer. We applied a simple low-pass filter only in the cases that were affected severely by high-frequency noise. Other appropriate signal processing steps may be applied to remove noise and

artifact from the input signal waveforms.

- **Inaccuracy in beat-onsets:** The beat-onset detection algorithm provides time-instants (sample numbers) to mark the start of each cardiac beat. Any jitter in these markers (in integer multiples of the sampling interval), directly affects the subsequent selection of points by the algorithm, such as the markers of sharp transitions in the ABP pulse, and deteriorates the results of computation.

- **Lack of patient information:** As discussed in Section 5.2.4, a change in the patient posture, for example a head-up tilt, can cause discrepancy between the radial measurement of ABP and cerebral ABP, as the ABP measurement is usually calibrated at the level of the heart. Our analysis showed that this discrepancy in ABP measurement appears directly in our nICP estimate. Therefore, it is important to record any posture changes that the patient might be going through, maybe for therapeutic reasons, and perform the correction in measured ABP before feeding into the estimation algorithm. However, our patient data did not have this sort of information available, and it might have contributed to significant bias in the estimates, such as the one seen in the case of Figure 6-3(a).

- **Algorithm choices:** Dispersion in the estimates can be controlled by some algorithm choices, such as the number of consecutive beats (or window length) used to set up the least-squares formulation for a robust estimate of the parameters. A larger window serves to average out the noise better but can degrade tracking of the transients. A window length of 10 to 60 beats was used in the results reported here.

6.4 Concluding Remarks

We have presented the validation of our ICP estimates against invasively measured ICP in 45 patient records, consisting of a total of about 35 hours of recorded data (>150,000 cardiac beats) and more than 3,500 independent ICP estimates. Compar-

ison of beat-by-beat estimates shows that nICP tracks the trends and even abrupt variations in ICP remarkably well. The overall bias in independent estimates is about 2 mmHg and the standard deviation of error is 8-9 mmHg. These numbers do not yet meet the accuracy target of about 4-5 mmHg error, but the estimates show the promise of the approach. If the issues causing bias and dispersion in the estimates are addressed, estimation performance is expected to improve to clinically acceptable levels.

Chapter 7

Exploring Model-Based Assessment of Cerebrovascular Autoregulation

As described in Chapter 5, our non-invasive model-based estimation algorithm provides continuous beat-by-beat estimates of cerebrovascular resistance (R) and compliance (C), in addition to an estimate of ICP. Temporal profiles of resistance and compliance estimates, possibly obtained separately for the left and right hemispheres, along with (measured) ABP, CBFV and (estimated) ICP, reveal much about the state of the cerebral vasculature. For one thing, we are then able to estimate CPP. Furthermore, the estimate of R and CPP can be used for a non-invasive and continuous assessment of cerebral autoregulation. Specifically, appropriate variations in R in response to abrupt changes in CPP suggest an effective autoregulation; lack of such adaptation suggests loss of autoregulation capacity.

An assessment of cerebrovascular autoregulation will aid in characterizing injury and recovery processes, and guide therapeutic action, for example in head trauma, stroke or cerebral artery disease. Furthermore, continuous and non-invasive model-based monitoring of cerebrovascular properties can help track a patient's cerebrovascular state more frequently and conveniently than current imaging-based analysis. There is also growing evidence suggesting that pre-term neonates might lack a fully

developed cerebral vasculature and hence the ability to regulate their cerebral blood supply [25, 135]. Tools for assessing autoregulation will potentially add to our understanding of such issues in this population.

Section 7.1 presents a few examples of autoregulation from the estimates of R and CPP, using the patient data we analyzed for validating our ICP estimates in Chapter 6. In Section 7.2, we describe our exploratory study on a data set comprising seven stroke patients and control subjects, who underwent a protocol of controlled interventions; we qualitatively validate our R and C estimates on the basis of their adaptation to the interventions. We discuss these results and possibilities for future work in Section 7.3.

7.1 Using R and CPP Estimates to Assess Autoregulation

Recall that the mean CBF (which we denote simply by CBF here, for notational simplicity) is given by

$$\text{CBF} = \frac{\text{CPP}}{R}, \tag{7.1}$$

where R is the cerebrovascular resistance represented in our model. Cerebrovascular autoregulation compensates for variations in CPP (within the operational range of autoregulation) by altering R. Our estimation algorithm provides estimates of CPP (= MAP − nICP) and R for each cardiac beat. Actually, as was shown in (5.16), our estimates of R are scaled by the unknown conversion of CBFV to CBF (e.g., the cross-sectional area of the MCA); recall from (5.16) that if CBF = αCBFV, then $\widehat{R} = \alpha R$. However, our interest is only in reliable variations in R, so with the assumption that the scale factor does not change significantly over the time scales of interest, we shall use our estimated R as a reasonable proxy for cerebrovascular resistance. Similarly, we shall (under the same assumption) use CBFV as a proxy for CBF.

From our estimates of CPP and R, and using the measured CBFV, we can attempt to infer the status of the cerebral autoregulation. Specifically, we can analyze the

dynamic trends in R during endogenous or exogenously induced variations in CPP, to determine whether cerebrovascular resistance adapts in a timely manner and in proportion to the change in CPP, in order to keep CBFV at the desired level. Such an analysis of the variables that are directly at the center of the physiological regulatory mechanism provides more insight and is easier to interpret, than the rather indirect existing approaches to assessment of autoregulation (as we pointed out in Chapter 3; see [30, 89] for a review of various existing approaches). Below, we demonstrate the sort of analysis we envision, by showing examples of some relevant patient records from our ICP validation data set, for which we have computed estimates of both ICP (and thus CPP) and R.

7.1.1 Example 1

We present an example first of how the estimates of R and CPP depict the effectiveness of cerebrovascular autoregulation. The top two panels in Figure 7-1 show MAP and ICP measurement, and the third panel shows the corresponding CPP. Note gradual fall in CPP (due to an underlying drop in MAP and rise in ICP) over 500 seconds in a patient (17-year old female, GCS = 5; the patient did not survive). The fourth panel in Figure 7-1 shows the corresponding beat-averaged CBFV (as our discussion about autoregulation in this chapter will refer to beat-averaged quantities, including MAP, ICP, and CPP). We observe that that while CPP drops from about 95 mmHg to 60 mmHg, CBFV is tightly maintained around 37 cm/s. This remarkable control suggests the compensatory action of cerebrovascular autoregulation in this duration of more than 4 minutes. The last panel in Figure 7-1 confirms this conjecture, as the estimated R decreases by about 40% of its initial value to mute the deficit in CPP, which is also about 40% of its starting point. Furthermore, the adaptation of resistance is fast enough to maintain CBFV close to its baseline throughout this initial interval.

The CPP continues to drop below 60 mmHg, but at that point the compensatory drop in resistance is not sufficient to maintain the CBFV, which starts to fall as well around $t = 360$ seconds. Ultimately, the CPP falls to less than 40 mmHg, and CBFV

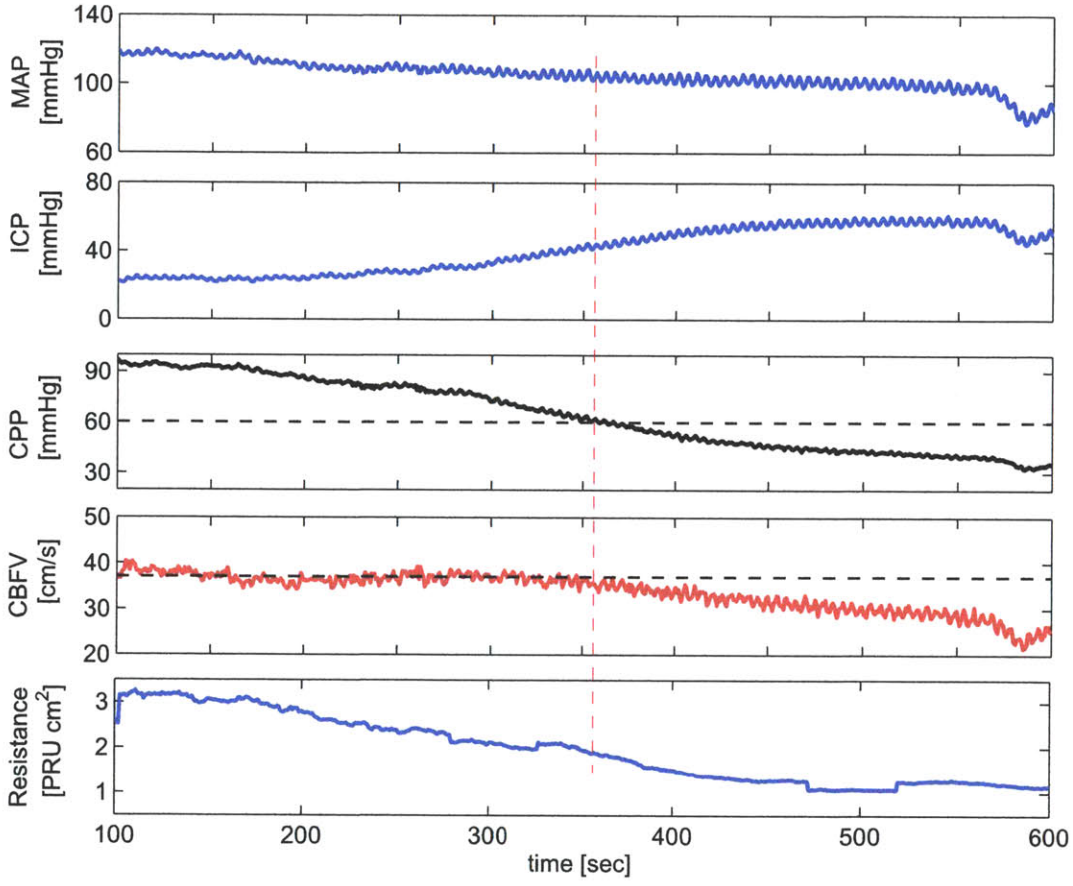

Figure 7-1: Cerebral autoregulation in action, as revealed by concomitant variations in CPP (actual) and R: while CPP falls by more than 30 mmHg, between 100 and 360 seconds, (mean) CBFV is remarkably maintained about its baseline (about 37 cm/s), which is explained by the accompanying drop in resistance. After CPP falls below 60 mmHg, CBFV also starts to drop.

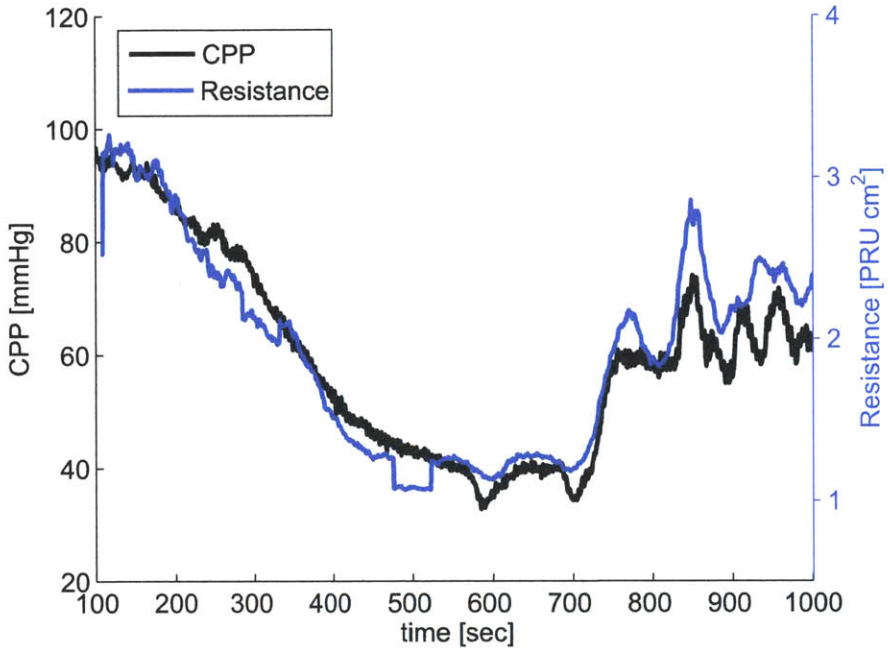

Figure 7-2: Time scale of autoregulation: the estimate of R has a fast response to variations in CPP, particularly in the most active region of autoregulation, CPP $>$ 60 mmHg.

also drops to about 30 cm/s; however, the latter drops only about 20% in the face of an almost 35% drop in CPP (from 60 mmHg to below 40 mmHg), thanks to a continuing decrease in the resistance.

Figure 7-2 shows CPP and R superimposed for the complete duration of the record (15 minutes). During the initial period between 100 and 350 seconds, when CPP is above 60 mmHg, the response time of the resistance is very quick, as it seems to drop at a faster rate than CPP. This is perhaps the region where autoregulation is most effective in this patient. The region above 60-70 mmHg is generally known as the flat part of the autoregulation plateau. When CPP is less than 50 mmHg, the resistance response is slightly slower, though it still tracks the CPP variations, and the autoregulatory capacity seems to be more limited.

This example lays down the basic ideas of a novel approach to form a non-invasive and continuous assessment of autoregulation. The next example shows similar features, but on a much slower time scale.

7.1.2 Example 2

Figure 7-3 shows another example involving a sudden drop in CPP, caused by a plateau wave in ICP. CPP drops from its baseline of 70 mmHg to about 35 mmHg and stays low for nearly 12 minutes. However, the corresponding CBFV, shown in the second panel, returns to its baseline much before the return of CPP. The last panel in Figure 7-3 shows the estimate of R provided by the estimation algorithm. It can be seen that the resistance starts to decrease immediately following the decline in CPP, and reduces to less than half of its baseline value, thus explaining the recovery of CBFV. The resistance stays at a lower level for the duration of the plateau wave. Finally, when CPP recovers (around $t = 45$ minutes) and subsequently increases above its baseline (beyond $t = 47$ minutes), the resistance first returns to its initial baseline and then increases, which brings CBFV down. This indicates an active response of the cerebral vasculature to compensate for the changes in CPP.

The dynamic behavior of CPP, mean CBFV and R in this example presents some issues and questions. First, cerebrovascular autoregulation is usually formulated in terms of CPP and CBF, rather than CBFV. If the scale factor for transformation of CBFV to CBF over the episode shown in Figure 7-3 is strongly pressure dependent, then the dynamic change seen in R might not truly reflect the action of a regulatory mechanism. Second, pressure autoregulation usually operates on the time scale of tens of seconds, while here the full response of R is not attained until after 10 minutes. At about 45 minutes, CBFV has an over-shoot type behavior, which perhaps indicates an episode of reactive hyperemia, as the CPP returns to its baseline. One should keep in mind, however, that the patient of Figure 7-3 is severely sick, which could conceivably impact not only the magnitude but also the time course of autoregulatory processes. Furthermore, the CPP falls to an extremely low level, less than 40 mmHg, where autoregulatory capacity is minimal. Irrespective of the particular situation of this patient, we feel that the variations of R in Figure 7-3 give credence to our argument that our model-based approach can be used for assessment of autoregulation.

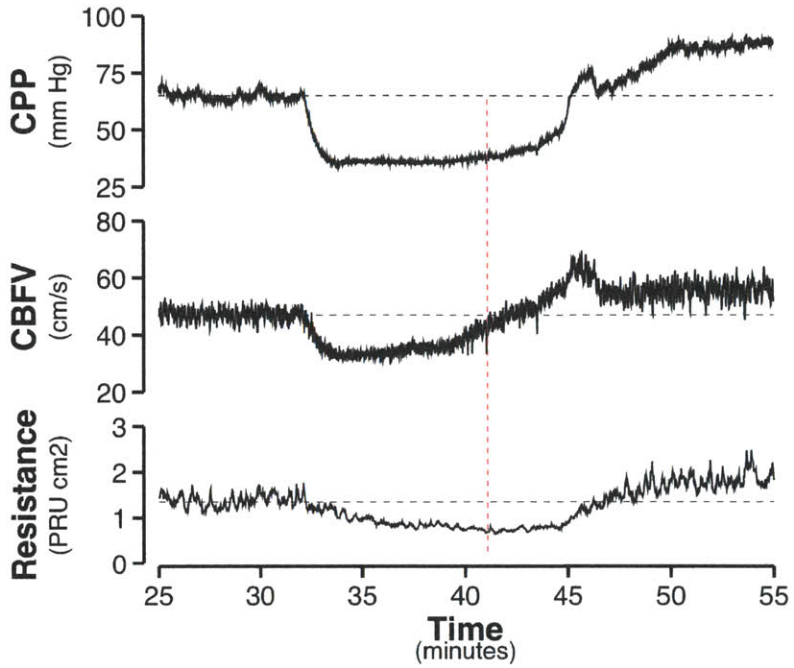

Figure 7-3: An assessment of autoregulation can be made by combining measurements of mean CBFV and estimated CPP and resistance. An example of a patient record is shown.

7.1.3 Why MAP *alone* fails to tell the story?

Most of the current approaches to characterize cerebral autoregulation suffer from the lack of access to ICP (due to the invasiveness of its measurement) and therefore rely on MAP only, rather than CPP, as a measure of the driving pressure for cerebral perfusion. Such an assessment can be misleading, as shown in Figure 7-4, in which an increase in (measured) ICP results in a *decrease* of CPP, even though MAP increases above its baseline (normal) range. If autoregulation assessment were based on MAP alone, one would be misled into thinking that the perfusion pressure has increased. After around the 40-minute mark, while MAP is increasing from about 80 mmHg to over 100 mmHg, yet we see a slight decrease in mean CBFV. This would probably suggest an increased resistance of the cerebral arteries. However, if we include ICP into our analysis, we see a plateau rising from about 20 mmHg to above 60 mmHg (the third panel in Figure 7-4 shows the measured ICP and our nICP estimate). Even though MAP has risen, too, the net change in CPP (measured CPP shown in the last

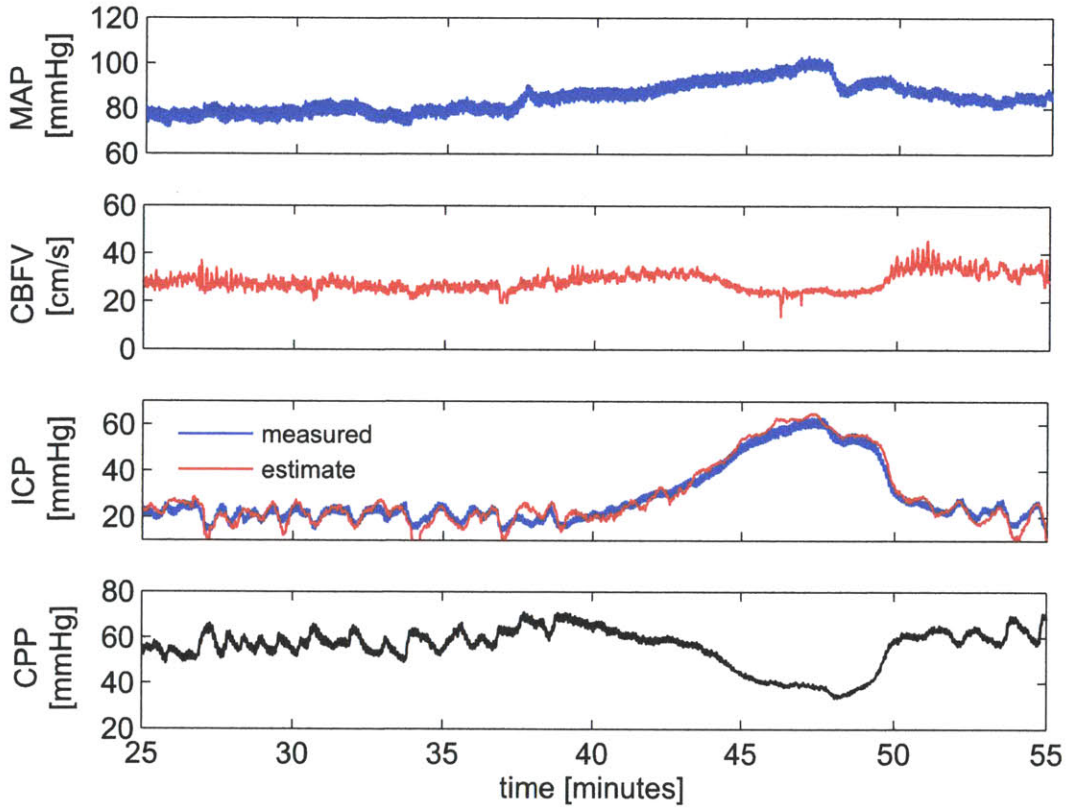

Figure 7-4: Characterization of autoregulation based on MAP alone, rather than CPP, can lead to erroneous conclusions (see text for a detailed discussion).

panel in Figure 7-4) is a drop of about 20 mmHg, which will lead to the *opposite* conclusion, namely that the resistance either decreased or stayed the same. Therefore, this example shows that ignoring ICP in autoregulation assessment can be grossly misleading.

Our model-based estimation algorithm provides continuous estimates of ICP, hence CPP, as well as R, allowing more accurate assessment of autoregulation. Furthermore, as the model parameters are the dominant cerebrovascular properties actively involved in the control mechanism, interpretation of autoregulation in terms of these parameters has a physiological basis. A direct patient-specific analysis of the variables central to autoregulation, i.e., CPP, R and CBFV, reveals the cerebrovascular state in a more meaningful way than a correlation-based index, calibrated using empirical calculations or observations on a set of population data, as is common to the majority of currently proposed indices of cerebrovascular autoregulation discussed in Chapter 3. Further work is needed to develop and refine the approach outlined here, and to generate an associated quantitative index of cerebrovascular autoregulation, which can then be tested in laboratory and clinical settings.

7.2 Exploratory Study Involving Stroke Patients

Although no gold standard measurements are available to validate our R and C estimates, we can supply some degree of qualitative validation by examining the response of these estimates to specific interventions that alter cerebrovascular resistance and compliance properties. We can also compare bilateral estimates of R and C in patients who might have asymmetric vasculature properties, for example due to a unilateral stroke or infarct in a carotid or cerebral artery. We were able to carry out such corroboration of our estimates using data from stroke and control subjects, courtesy of Dr. Vera Novak, Beth Israel Deaconess Medical Center (BIDMC), Boston, MA. We now describe these experiments and results.

7.2.1 Data and interventions

The data were collected at the BIDMC's Syncope and Falls in the Elderly (SAFE) Laboratory under the supervision of Dr. Vera Novak, and include records for stroke and diabetes mellitus patients, as well as elderly subjects studied under controlled interventions in a laboratory environment. The database contains over 300 continuous recordings of CBFV via bilateral TCD, radial ABP, end-tidal CO_2 and O_2, and information on interventions, age, gender, race, ethnicity and anthropometric measurements (height, weight), along with anatomical and perfusion MRI studies of the brain. Although ICP was not measured for patients in this study, the other information is available and valuable for our investigation of autoregulation.

The data were collected in a laboratory setting before and during a set of interventions performed according to a fixed protocol. The interventions included hyperventilation for 200 seconds, hypoventilation for the next 200 seconds, and a head-up tilt for 10 minutes.

7.2.2 Cerebrovascular estimates

The estimates of C, R and ICP were computed from the CBFV and ABP waveforms using our model-based algorithm described in the previous chapters. The data from a total of 7 subjects (3 stroke and 4 control cases). The ABP measurement is calibrated to the level of the heart, so we applied a correction to the measured ABP to correct (approximately) for the relative height between the heart and the MCA during head-up tilt. Below, we describe the estimates in two representative cases: one is a stroke patient (with a left-sided infarct) and the other a control.

The measurement data and our estimates of ICP, resistance R and compliance C are shown in Figure 7-5, for the stroke patient in the left column and the control subject in the right column. The top two panels contain MAP and bilateral CBFV measurements for the left (blue) and the right (red) hemispheres. Note the asymmetry of the left and right CBFV in the stroke patient, and remarkable symmetry in the control subject. The lower three panels contain the estimates; each panel shows

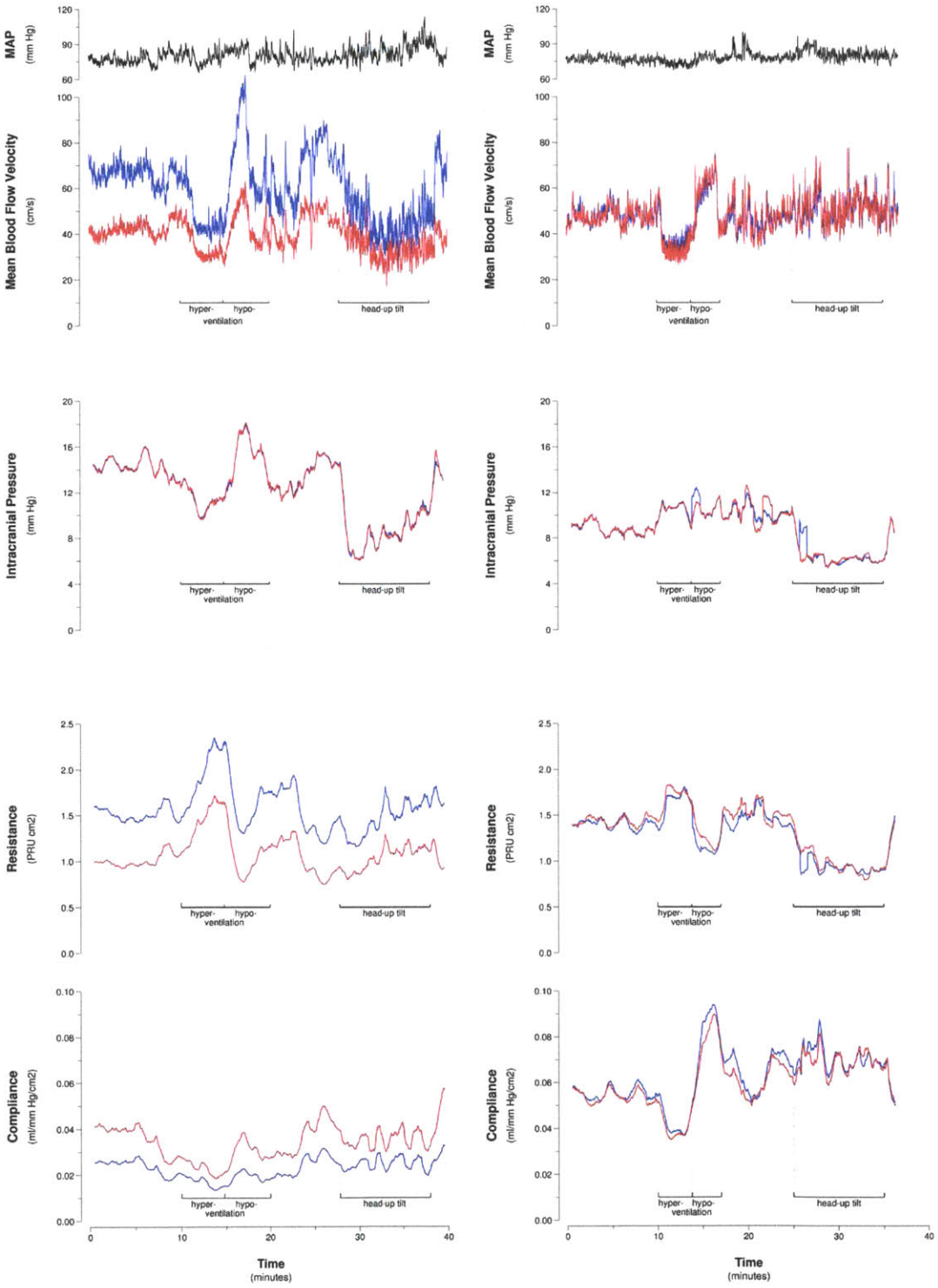

Figure 7-5: Comparing MAP and mean CBFV measurements along with the ICP, resistance and compliance estimates for stroke (left column) and control (right column) cases. Mean CBFV and the estimates are shown for both the left and right hemispheres, in blue and red respectively. The dashed markers indicate the intervals of the various interventions.

estimates for the left and right hemispheres. The following observations can be made from these results.

- The responses in estimated ICP, R and C to the various interventions are consistent with what one would expect to find, given the nature of the interventions. Specifically, the changes in these quantities line up well with the markers for the interventions. Hyperventilation is expected to cause cerebral vasoconstriction, marked by an increase in resistance and a drop in compliance, while hypoventilation has exactly the opposite response. These are indeed observed in the fourth and fifth panels, for both subjects, for both the left- and the right-sided estimates.

  ICP is expected to respond to hyperventilation (and hypoventilation) by a small upward (downward) shift, which is observed in the estimate for the stroke subject. The estimate in the control case does not agree with this expectation, though its overall variation is somewhat muted (remains between 8 and 10 mmHg, and the little variations are not synchronized with interventions), particularly when compared with the variations seen in the stroke case. Such aspects need further exploration. During the head-up tilt, ICP is expected to drop and to come back at the end of the tilt, and this again is observed in the ICP estimates.

- Figure 7-5 shows that the ICP estimates obtained using left-side and right-side data coincide to a remarkable degree, both for the control and the stroke subjects. This alignment is despite the fact that CBFV for the stroke patient differs by more than a scale factor between the left and right hemispheres, as can be seen in the top panels of Figure 7-5.

- The resistance and compliance estimates in the left and right hemispheres match closely for the control case but they are different in the stroke patient. With the stroke patient, the resistance estimate for the left hemisphere is higher than for the right, which would seem to be consistent with the infarct on the left side (reduced blood flow), though of course there may also be differences in

the respective scale factors for transformation from CBFV to CBF. A similar discrepancy can be noted in the compliance estimate for the stroke patient, where the side with infarct (left) has a lower compliance estimate.

These are just preliminary results in an exploratory study of the application of our model-based estimation to stroke patients. However, these add credibility to the approach and demonstrate the plausibility of our R and C estimates.

7.3 Discussion

Continuous resistance and compliance estimates in parallel with estimated CPP provides a dynamic profile of the cerebral vasculature, which can be helpful in various clinical circumstances. Firstly, the temporal variations in R and C in response to administration of a drug or other intervention can be revealing about the status of cerebral vasculature. Secondly, the response of these vascular properties to variations in MAP or ICP or both can be an indicator of the effectiveness of autoregulation. Thirdly, an asymmetry between the left and right estimates of R (and, similarly C) can be a useful indicator of the state of recovery after a cerebrovascular disease, infarction, or vasospasm.

A current limitation in autoregulation assessment is the lack of a gold standard measure of autoregulation. Therefore, our estimates, or the assessment based on them, cannot be directly validated. This is a current shortcoming of the field of cerebrovascular autoregulation. Nevertheless, the preliminary results presented in this chapter show the potential of forming clinically useful methods for the assessment of autoregulation.

Chapter 8

Conclusions and Future Work

8.1 Conclusions

We have developed a model-based approach for continuous and non-invasive estimation of ICP, CPP, cerebrovascular resistance, and cerebrovascular compliance. Being able to non-invasively track trends in these quantities opens the door for novel approaches to neuro-critical care and improved assessment of cerebral autoregulation.

Our algorithms interpret available clinical data using the constraints provided by a reduced-order mathematical model of cerebrovascular dynamics, to relate CBFV (in the MCA, acquired by TCD ultrasound) and ABP to ICP. The model provides a simplified mechanistic view of the relevant cerebrovascular physiology. The estimation algorithm then solves for the unknown model parameters using the time-synchronized measurements of radial ABP and CBFV. To obtain robust estimates, the algorithm extracts information from the intrabeat variations in the input waveforms, as well as their variations across cardiac beats. Furthermore, our estimation approach is immune to discrepancies in translating TCD measurements of CBFV to CBF, as our ICP estimates are independent of the unknown scale factors required for translating TCD measurements into CBF. To our knowledge, such a model-based approach to interpreting the ABP and CBFV waveforms has been missing.

Our ICP estimates track invasive ICP measurements in 45 patient records with promising accuracy. While there is no unanimous agreement on the desired clinical

accuracy for a non-invasive ICP monitoring method, we believe an absolute error of less than 4-5 mmHg can be tolerated without affecting clinical decision-making. Our non-invasive estimates have a small bias of about 2 mmHg, and the standard deviation of error in independent estimates is about 8 mmHg. The standard deviation of error across all patient records is about 6 mmHg. These tolerances are currently larger than the target range of 4-5 mmHg. However, the accuracy of our model-based method is already comparable with some of the invasive approaches for ICP measurement [1]. Furthermore, we believe that several characteristics of the current input data cause deterioration of estimation performance. Addressing these issues is likely to improve the error statistics.

In summary, the distinguishing features of our estimation method are as follows:

- Our non-invasive continuous ICP estimation approach is based on a mechanistic model of the cerebrovascular physiology and therefore provides estimates of clinically interpretable and actionable parameters. Our three-parameter model is a highly reduced representation of cerebrovascular physiology, which retains the association of its parameters to the underlying physiological variables.

- The estimation algorithm combines time-synchronized measurements of ABP and CBFV, using the model constraint to compute beat-by-beat estimates of ICP, R and C, which can be provided in real-time.

- The estimation algorithm exploits intrabeat variations in the ABP and CBFV waveforms, as well as their beat-to-beat variations, to compute robust estimates.

- Our ICP estimates are independent of the unknown scale factor between CBF and the TCD measurements of CBFV.

- Our model-based estimation approach does not require any training on population data or specification of any external parameters.

[1] While evaluating the estimation performance of our method, we did not exclude any outliers. However, evaluations of different ICP measurement modalities have been more liberal in removing such cases [77, 79, 81].

- The estimates do not depend on the history outside the estimation window of a few consecutive cardiac beats, as the estimation algorithm does not learn within a specific patient.

- The method does not require any calibration data.

8.2 Future Work

The following items are natural next steps of this project, and can be part of future research and development.

- **Improvements in data acquisition**

  As pointed out earlier, sampling frequency and quantization artifacts in the input measurements significantly affect estimation performance. The patient data used for validation of our ICP estimates was collected in the 1990's, with the limitations of technology at that time. With better instrumentation, improvements in the data acquisition are easily possible nowadays. For example, a sampling frequency of 200 Hz or above is quite common in biomedical equipment and data recording. Similarly, the TCD signal quality needs to be improved to reduce dispersion in the estimates. Data acquisition should also take into account patient posture, to account for the hydrostatic offset from the measured ABP, which is usually calibrated at the level of the heart, to ABP at the level of the MCA.

- **Expansion to a diverse patient population**

  Our validation was primarily centered on of one particular pathology, namely comatose patients with closed-head TBI. The next step should be to apply our approach to data representing a diverse set of pathologies, including hydrocephalus, brain tumor, and other forms of TBI.

- **Further refinement and validation of ICP estimates**

  With improvements in data acquisition, our method might be able to incorporate certain enhancements in its specific computational steps, benefiting from

the higher quality of signals. For example, an increased sampling frequency will allow the phase offset estimation to be performed at higher time resolution, and accuracy in the offset estimate will likely reduce the bias in the estimates. Similarly, filtering to remove noise, numerical approximation of the derivative of ABP in the algorithm, and signal-quality assessment should be revisited, to leverage improvements in data acquisition.

As the method is tested in a diverse patient population, we might also need to revisit our mathematical model. Our estimation performance with a simple model has been very encouraging. It is conceivable, however that in a particular pathophysiological scenario, a revised version of the model better captures the corresponding cerebrovascular dynamics, and thus improves the estimation performance.

- **Prototype system development**

  We foresee establishing a dedicated data acquisition infrastructure at a neurocritical care unit of a collaborating hospital. A logical next step in support of this effort is to build a component-based prototype system and use it for prospective, real-time validation of our method.

- **Quantifying and validating autoregulation**

  Our qualitative analysis of CPP and R estimates in Chapter 7 in order to assess the status of autoregulation shows sufficient promise to warrant further exploration. In a future project, our model-based estimates may be quantitatively analyzed in order to develop an index of cerebrovascular autoregulation, and to consider approaches to the subtle task of clinical validation. Our exploratory study in stroke subjects also suggests the possibility of using non-invasive continuous estimates of resistance and compliance in monitoring the cerebral vasculature.

- **Improvements in hardware and integration**

  Finally, the innovation laid out in this thesis provides opportunities for hardware integration and sensor improvements. Improvements in the TCD technology are

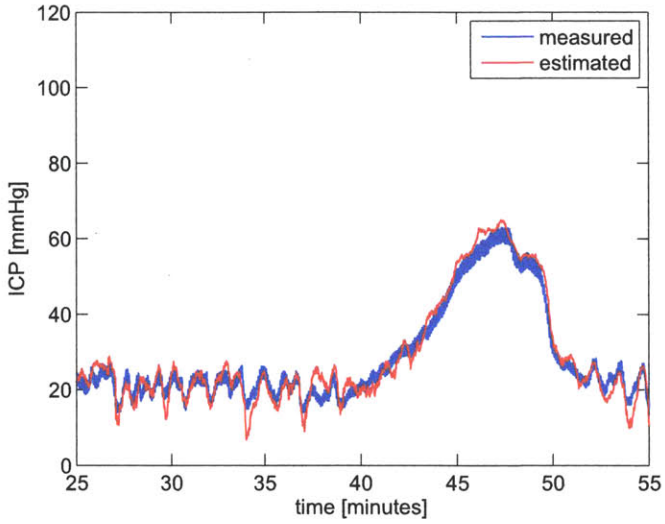

Figure 8-1: An example of very striking estimation performance, particularly because no invasive measurement was used to train or calibrate the estimation method. Estimation performances like these point to the promise of our model-based patient-specific approach.

required to provide measurements at higher amplitude resolution and sampling frequency to facilitate intrabeat morphological analysis of its waveforms (of the type employed by our estimation algorithm). Furthermore, the TCD sensor technology can be enhanced, perhaps through development of self-focusing arrays, to reduce the expertise required to perform the CBFV measurements at the target cerebral artery, as well as to improve signal quality. Finally, the Finapres-type device may be combined with TCD to reduce the footprint of the ICP estimation hardware.

We plan to build upon this work in the near future and address some of the above items. Our enthusiasm rests on the promise provided by the overall estimation results, and especially results such as that shown in Figure 8-1, in which our non-invasive ICP estimate tracks exceedingly well even the minute fluctuations in measured ICP, without using any calibration data. The compelling motivation for our work is the prospect of helping to reduce the morbidity and mortality associated with brain injury and cerebrovascular disease.

Part IV

Appendices and Bibliography

Appendix A

Cerebral Venous System and Starling Resistor Model

Veins are thin-walled, collapsible vessels with very little capacity to withstand negative transmural pressures. The cerebral veins in the cranial space are surrounded by CSF, and its associated fluid pressure (ICP) provides an external pressure that exceeds the internal (luminal) venous pressure of the larger cerebral veins. These cerebral veins therefore will be in a partially (or fully) collapsed state [13, 14]. Collapse of flaccid vascular structures is a common occurrence in biological fluid flow, and underlies respiratory flow limitation or our understanding of the venous return curve, for example. Here, we describe a very simple model, the Starling resistor, that accounts for some of the observed characteristics of such vessels. The topic of fluid flow through collapsible vessels is still an active area of research in computational fluid dynamics. A review of the dynamic behavior of such vessels is well beyond the scope of this appendix. The interested reader might consult [136] or [137] for detailed treatments of this subject.

A.1 The Starling Resistor Model

The Starling resistor model is often used to capture the pressure-flow relationships in vessels that can collapse. Common examples of this in biological system are blood

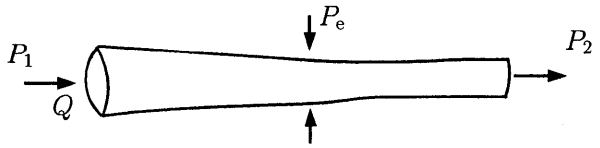

Figure A-1: Flow through a collapsible tube: P_1 and P_2 are the upstream and downstream pressures, respectively, and P_e is the external pressure. Flow is denoted by Q.

flow through peripheral veins, and air flow through the respiratory system. We first present the Starling resistor model and then elaborate on it.

Figure A-1 shows a collapsible tube with a steady flow Q through it, an inlet pressure P_1, an outlet pressure P_2, and an external pressure P_e. We assume a uniform external pressure along the tube length. Furthermore, we assume that both ends of the tube are connected to rigid vessels so that there is no possibility of a collapse upstream of the inlet or downstream of the outlet.

In the Starling resistor model, three conditions are distinguished, based on the values of the steady state pressures P_1, P_2 and P_e [11, 137].

Case I: $(P_1 > P_2 > P_e)$ In this case the tube is completely open. As long as the tube is distended/open, flow is proportional to the pressure difference $P_1 - P_2$. The constant of proportionality is the inverse of the resistance of the tube, $1/R$. Pressure drops steadily along the length of the tube, from P_1 to P_2. At all points along the tube, the inside pressure is greater than the external pressure and hence the tube stays open. Flow is independent of P_e.

Case II: $(P_1 > P_e > P_2)$ As P_e is increased from below P_2 to above P_2, the tube starts to collapse due to the higher external pressure, with the cross sectional area of the tube decreasing in the region where inside pressure is less than the external pressure. This causes the flow to drop relative to the flow in Case I, because the downstream pressure is now effectively P_e. The Starling resistor model in fact assumes that flow in this region is independent of P_2 — hence, also known as the "vascular

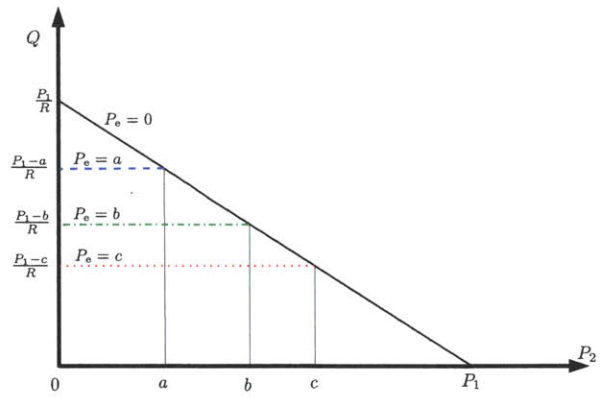

Figure A-2: Behavior of the Starling resistor model. The heavy black line corresponds to flow in the uncollapsed state, with $Q = (P_1 - P_2)/R)$. Different external pressure conditions lead to collapse of the tube at different values of P_2, causing different net flow in each case.

waterfall". At any given P_2, the effective resistance of the tube is given by

$$R_{\text{collapsed}} = \frac{P_1 - P_2}{Q_{\text{collapsed}}}, \tag{A.1}$$

and $R_{\text{collapsed}} > R$. Since decreasing P_2 does not increase the flow, which stays at the same $Q_{\text{collapsed}}$, the effective resistance of the tube increases.

Case III: $(P_e > P_1 > P_2)$ Finally, when the external pressure is equal to the inlet pressure, the tube is completely collapsed and there is no flow; the tube offers infinite resistance.

The behavior of the model is graphically shown in Figure A-2. The Starling resistor model clearly gives a simplified view of the pressure-flow relationships in collapsible tubes. A more realistic model that takes account of the elastic properties of the tube, the viscosity of the fluid and the flow velocity profile (or the Reynold's number) will have characteristics more like those shown in Figure A-3. However, the simple view is still good enough to closely study various practical scenarios, such as blood flow through peripheral cerebral veins that are generally in collapsed state, and flow of air through the respiratory system.

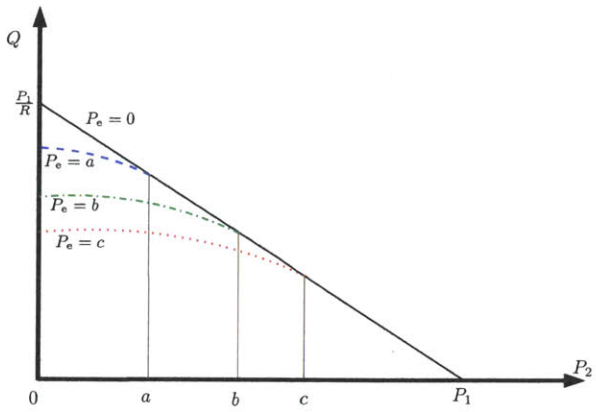

Figure A-3: Pressure-flow relationships for a more realistic representation of collapsible tubes than the Starling model.

A.2 Collapsibility of Cerebral Venous System

Due to ICP being above venous pressure in most situations of interest, the cerebral veins are believed to be in a collapsed state. The invocation of a Starling resistor model is thus quite natural, as has been used in the models of the cerebrovascular dynamics [14,87]. Experimental studies in dogs also concluded that a Starling resistor model is an accurate representation of the cerebral venous blood flow [138]. Depending on the local pressure and the vessel radii, veins are either in a collapsed state or in a distended state. We term this as 'distributed venous collapse', and it warrants a more careful description of the flow through the venous system. Smaller cerebral veins join in to larger cerebral veins, also called bridge veins, which then ultimately connect to the venous sinuses. The mean luminal capillary pressure is normally about 30 mmHg, which decreases along the flow in the venous system, reduces to less than 10 mmHg in the large veins, and is only about 5 mmHg in the venous sinuses. At an intermediate point on the large cerebral veins, ICP (7-15 mmHg normally; higher in intracranial hypertension) exceeds the internal luminal pressure (around 5 mmHg) [13, 14] and causes the veins to collapse, the segment proximal to the arterial side being open, and the distal segment being collapsed. Due to the rigidity of their walls, the venous sinuses do not usually collapse, even though their luminal pressure is less than ICP.

Appendix B

Validation of Estimation Algorithm Using Simulated Data

In Chapters 4 and 5, we developed our reduced model and the algorithm to estimate its parameters. Before applying our algorithm to the clinical data described in Chapter 6, we validated our estimation algorithm on simulated ABP, CBF and ICP waveforms. To generate these signals, we simulated the modified Ursino-Lodi model of Chapter 4, and recorded the pressure and flow waveforms throughout the model, including ICP and CBF. We then analyzed these waveforms in the context of our estimation algorithm (based on our reduced model) and obtained the estimates of R, C and ICP. Comparison of the estimates against the chosen values shows good agreement between simulation and estimation. The results of these studies formed the basis for an initial publication [10], and patent disclosure [139] that has now resulted in a patent application [140]. Success in simulation studies encouraged us to test our method on real clinical measurements, the estimation results for which were presented in Chapter 6. In this appendix, we present the results of two simulation studies in detail.

B.1 Model Simulation for Data Synthesis

To generate data for our analysis purposes, we supply an experimental ABP waveform as input to the modified Ursino-Lodi model (see Section 4.3). The control loops are kept operational and model parameters are set to the nominal values specified in [9]. To represent some of the phenomena of clinical interest, such as intracranial hypertension and plateau waves [75, 133, 134], we choose appropriate perturbations on I_{i} (see Figure 4-7). We simulate the model and record the model output (pressure and flow waveforms), including ICP and CBF. An example of these simulated waveforms was presented in Figure 4-8, and Figure 4-9. These waveforms are then used to analyze the performance of our estimation scheme. We present two such cases and discuss the performance of our estimation algorithms for these data sets.

B.2 Analysis of Data for Estimation Results

Example 1

In one of the simulation runs, a perturbation I_{i} of 1 ml/sec was applied at $t = 10$ sec for a duration of 10 seconds, and then at $t = 40$ sec for a duration of 5 seconds. The model was simulated for an experimental ABP waveform provided as the input. Cycle-averaged ABP, CBF and q_1 (i.e., the flow through R_{a}) are shown in Figure B-1. We also record cerebrovascular resistance and arterial compliance, whose variations represent the autoregulatory mechanism.

The dashed lines in Figure B-2 show the beat-by-beat values of compliance, resistance and ICP obtained from the simulation for this particular run. ICP increases rapidly to about 40 mmHg at $t = 10$ sec, and to 45 mmHg at $t = 40$ sec due to the perturbations in I_i. Another observation to be made here is that the resistance shows a dramatic change at about $t = 160$ sec. This variation corresponds to a sudden drop in the input MAP around that time.

Taking the simulated ABP and CBF waveforms, the estimation algorithm computes beat-by-beat estimates of C, R, and ICP. Figure B-2 shows that the estimates

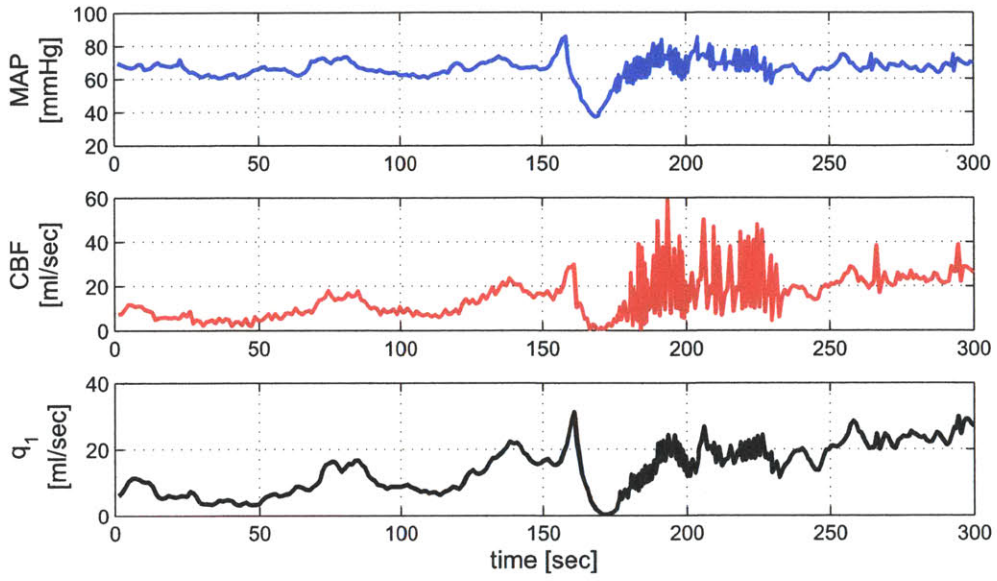

Figure B-1: Simulation data set 1: cycle-averaged ABP, CBF, and q_1 (flow through R_a) obtained by simulating the modified Ursino-Lodi model are shown (top to bottom).

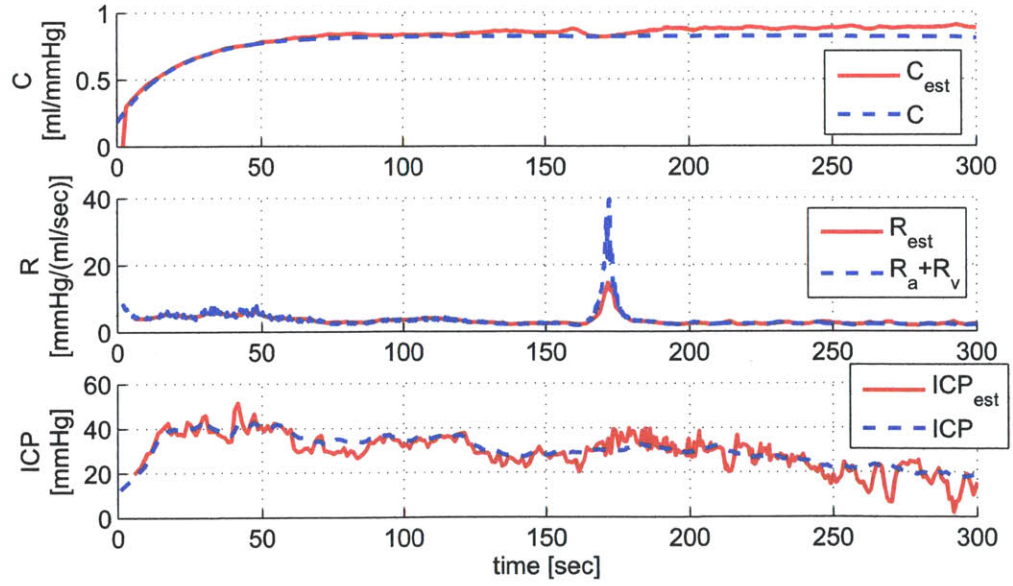

Figure B-2: Estimation performance: beat-by-beat values of C, R and ICP are shown, where the blue (dashed) lines correspond to the simulated values in the Ursino-Lodi model, and the estimates are shown in red (solid) lines.

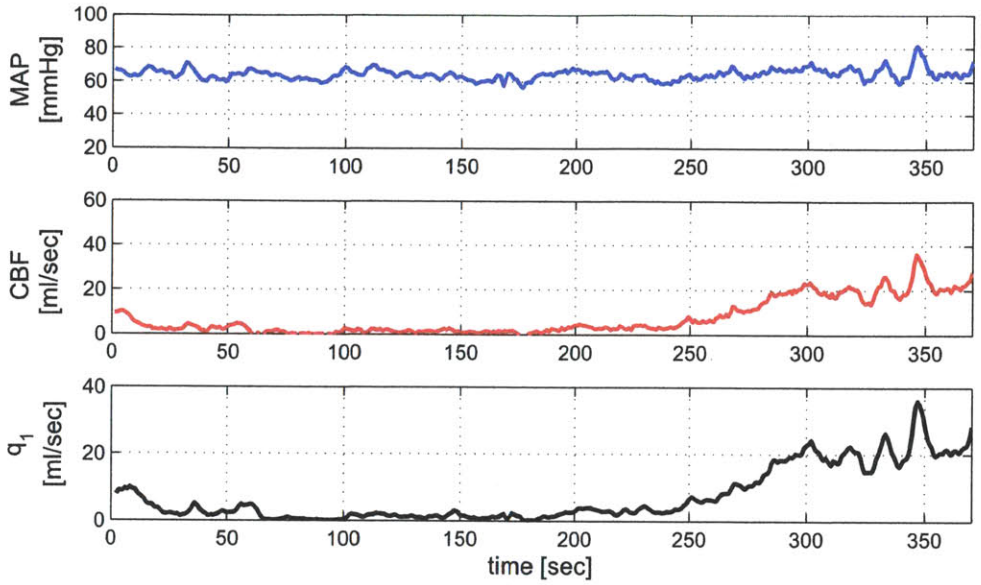

Figure B-3: Simulation data set 2: cycle-averaged ABP, CBF, and q_1 (flow through R_a) generated by simulating the modified Ursino-Lodi model are shown (top to bottom).

(solid lines) agree with the simulation values (dashed lines) quite closely. Note that the simulated ICP contains significant dynamic variations throughout the simulation period, which are tracked by the estimated ICP quite well.

Example 2

In a second simulation study, we again use an experimental ABP waveform as the driving input for numerical simulation of the modified Ursino-Lodi model. Cycle-averaged ABP, CBF and q_1 are shown in Figure B-3. A perturbation was applied to simulate variations in ICP by injecting CSF into the cranial space at $t = 10$ sec at a rate of 1.5 ml/sec for 10 seconds, and at $t = 60$ sec at a rate of 3 ml/sec for 5 seconds. Corresponding to these time instants, the simulated ICP rises to approximately 40 mmHg, then drops below 40 mmHg and rises again to approximately 45 mmHg as shown in the last panel in Figure B-4 by the dashed line. The simulated compliance and resistance are shown in the first and second panel, respectively.

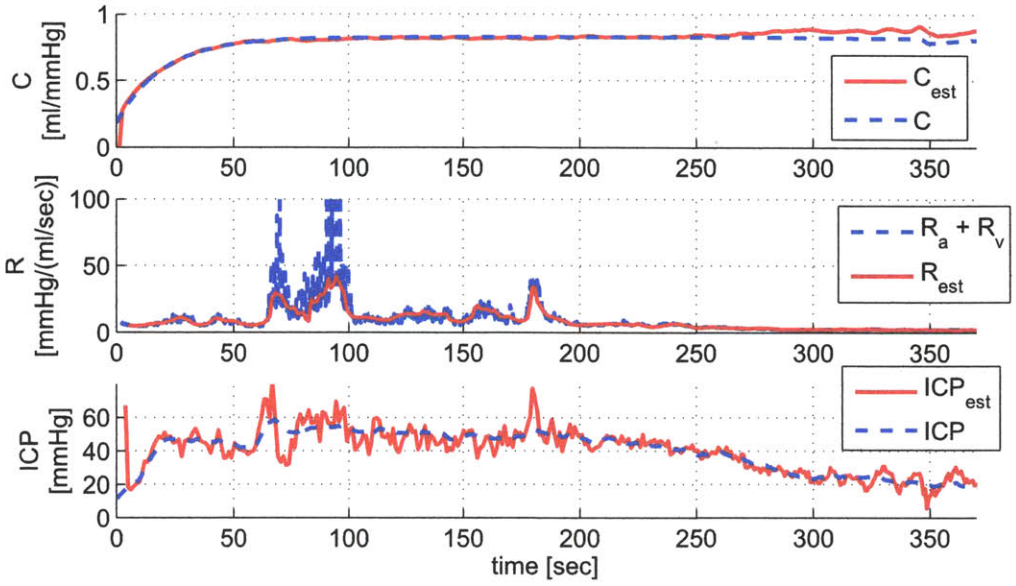

Figure B-4: Estimation performance: beat-by-beat values of C, R and ICP are shown, where the blue (dashed) lines correspond to the simulated values in the Ursino-Lodi model, and the estimates are shown in red (solid) lines.

Taking the simulated waveforms of ABP and CBF as the available data, our estimation algorithm produced estimates of C, R and ICP as shown in Figure B-4. As seen in the previous example, the estimates (solid lines) generally show good agreement with the simulated values (dashed lines) for all three parameters. However, note that for a period of about 30 seconds around $t = 80$ sec, the simulated (reference) resistance is very high and contains huge dispersion. This is caused by the mean CBF being close to zero during this time interval (see Figure B-3). We also observe a relatively large estimation error in R and an unusual deviation in the ICP estimate during this period. Another episode of similar behavior, though much shorter than the first one, can be seen at about $t = 175$ sec. The estimated resistance tracks this rather abrupt variation in the simulated resistance remarkably well.

The input CBF recovers from zero after $t = 250$ sec, as also seen by the resistance dropping very low. In this period of about 100 seconds, the input MAP and CBF contains prominent dynamic variations, which induces variability in the ICP estimate. Note that the ICP estimate also captures the sudden rises in simulated ICP, caused

by the intended perturbation I_i, at $t = 10$ sec and $t = 60$ sec, respectively. Again a higher variability in the input ABP and CBF near the end of simulation period induces variations in our ICP estimates.

Our simulation studies show that the estimates of our reduced model agree with the reference values specified in the simulations. In particular, the ICP estimates track the simulated ICP closely. These results encouraged us to apply our estimation algorithm to real clinical measurements.

Appendix C

Other Parameter Estimation Approaches

In Chapter 5, we described a two-step algorithm to estimate the parameters of our reduced model. That is however only one of several possible approaches to parameter estimation. Applying different system identification ideas, we developed at least three other estimation strategies: single-step estimation, estimation via modulating functions, and estimation from cycle-averaged ABP and CBFV measurements. In this appendix, we first provide a brief description of these approaches, and then highlight the key features of our two-step estimation algorithm, which make its performance superior to the ones described here.

I. Single-Step Direct Estimation

Recall the differential equation for the reduced model, which relates the measured variables $q(t)$ and $p_{\mathrm{a}}(t)$ to the parameters R, C, and p_{ic}:

$$q(t) = C\frac{dp_{\mathrm{a}}(t)}{dt} + \frac{p_{\mathrm{a}}(t) - p_{\mathrm{ic}}}{R}\,. \tag{C.1}$$

From the available continuous measurements (or their approximations) of $p_{\mathrm{a}}(t)$ and $q(t)$, we can develop a direct estimation scheme, which solves for all three unknown parameters in a single step. Choosing K data points over an interval possibly spanning

several consecutive beats, we write the above constraint on the measurements in the following linear form:

$$\begin{bmatrix} q(t_1) \\ q(t_2) \\ \vdots \\ q(t_K) \end{bmatrix} = \begin{bmatrix} \dot{p}_{\mathrm{a}}(t_1) & p_{\mathrm{a}}(t_1) & -1 \\ \dot{p}_{\mathrm{a}}(t_2) & p_{\mathrm{a}}(t_2) & -1 \\ \vdots & & \\ \dot{p}_{\mathrm{a}}(t_K) & p_{\mathrm{a}}(t_K) & -1 \end{bmatrix} \begin{bmatrix} C \\ \frac{1}{R} \\ \frac{p_{\mathrm{ic}}}{R} \end{bmatrix} . \tag{C.2}$$

Appropriate selection of the data data points is required to capture sufficient variability of the measured signals, so that the matrix in (C.2) has columns that are numerically (i.e., robustly) independent. We then obtain a least-squared error solution for the unknown parameters C, $1/R$, and p_{ic}/R. The process is repeated for the next selection of K data points, usually obtained by advancing to the next cardiac beat.

Stability of the computed estimates strongly depends on richness of the data, as this determines the degree of linear independence of the columns of the coefficient matrix in (C.2)), or condition number. Furthermore, in our experiences with this approach we found the estimate of C to be highly sensitive to the variations and noise in the measurements. This is partly related to the need in this approach to compute derivative of ABP measurements, which is generally a source of numerical instability.

II. Modulating Function Approach to Estimation

The modulating function (or mod-function) approach to system identification is usually applied to alleviate problems due to differentiation of the measurements that may be involved in system identification, as was the case in the above approach. Taking the derivative of a measurement also differentiates any additive noise, amplifying the resulting noise in parameter estimates. We explain the mod-function approach in the context of our model parameter estimation.

A direct time-domain identification process using (C.1) involves computing $\frac{dp_{\mathrm{a}}(t)}{dt}$, which amplifies noise in the measured $p_{\mathrm{a}}(t)$. The mod-function approach suggests multiplying both sides of the equation by a smooth function (which is easy to dif-

ferentiate), and integrating over a fixed time interval. Exploiting the principle of integration by parts, the derivatives of the measurement signals can be replaced by the derivative of the mod-function, thus avoiding the problem of accentuating noise in the measurements. More detail on system identification based on the mod-function approach can be found in [141].

A particular mod-function approach to estimate our model parameters uses a rectangular pulse as the mod-function. Now choosing a window of appropriate size, usually a fraction of the beat duration, and integrating (C.1) over the window yields an equation with the three desired unknown variables,

$$\bar{q}[n] = C\Delta p[n] + \frac{(\bar{p}[n] - p_{\mathrm{ic}})}{R}\,, \tag{C.3}$$

where $\bar{q}[n]$, $\bar{p}[n]$, and $\Delta p[n]$ are defined as:

$$\begin{aligned}
\bar{q}[n] &= \frac{1}{T_n - T_{n-1}} \int_{T_{n-1}}^{T_n} q(t)dt\,, \\
\bar{p}[n] &= \frac{1}{T_n - T_{n-1}} \int_{T_{n-1}}^{T_n} p_{\mathrm{a}}(t)dt\,, \\
\Delta p[n] &= \frac{p_{\mathrm{a}}(T_n) - p_{\mathrm{a}}(T_{n-1})}{T_n - T_{n-1}}\,.
\end{aligned}$$

Advancing the window to the next beat-segment, we can write another similar equation. Repeating the process for several consecutive beats yields a system of linear equations, which we solve by a least-squared error approach, as described in the single-step estimation. The computed estimates are associated to the middle beat of the estimation window, and the process is repeated starting over at the next cardiac beat.

III. Estimation Using Beat-Averaged Measurements

It seems desirable to explore whether our model parameters can be reliably estimated from only the mean ABP and mean CBFV. We accordingly developed a set-up similar to (C.1), but specified in terms of beat-averaged $p_{\mathrm{a}}(t)$ and beat-averaged $q(t)$.

The system of equations looks quite similar to the one obtained in Section I here. However, since the measurements are specified as beat-by-beat averages, which vary far less than the pulsatile waveforms, the system tends to have poorer numerical conditioning. We found the estimates obtained via this scheme approach somewhat close to the expected parameter values only when the means of the measurements showed appreciable variations.

Summary

The two-step algorithm described in Chapter 5 provided more robust estimates than the three approaches described in this appendix, and therefore was used to analyze patient records. By exploiting particular intrabeat features of the time-synchronized ABP and CBFV waveforms, the two-step algorithm represents the reduced model by two distinct dynamic constraints, and obtains a least-squared-error solution for the parameters involved in each constraint. Furthermore, careful selection of the data points to be processed within each cardiac beat reduces the effects of noise in the measurements, and minimizes the propagation of error in the estimate computed in the first step to the next step. Attention to these specific details proved crucial to robust estimation of our model parameters.

Appendix D

Summary of Clinical Data and Estimation Performance

The table below provides a record-by-record summary of the clinical data and the estimation error in our nICP estimates in all 45 patient records that were analyzed for validating the estimates. Clinical measurements are summarized by their time-averages, computed over the entire record for MAP, mean CBFV, ICP, and heart rate (HR); HR is derived from the ABP waveform, and has the units of beats per minute (bpm). Estimation error (nICP-ICP) in each record is summarized by root-mean-square-error (RMSE), bias, and standard deviation of error (SDE).

Patient ID	MAP (mmHg)	CBFV (cm/s)	HR (bpm)	ICP (mmHg)	RMSE (mmHg)	Bias (mmHg)	SDE (mmHg)
A	80.1	49.4	73	11.8	3.7	1.5	3.4
B	103.1	83.7	78	7.5	7.1	3.3	6.4
C	90.7	54.9	98	6.2	8.6	7.9	3.5
D	76.2	85.0	90	8.5	5.7	5.5	1.5
E	86.7	42.6	59	13.6	3.2	2.7	1.7
F	101.6	47.0	87	22.2	6.5	5.6	3.3
G	96.2	86.6	76	13.2	2.5	−0.5	2.5
H	87.1	133.7	81	17.4	2.6	−1.4	2.2
I	86.7	76.9	57	1.4	3.6	2.3	2.8
J	75.4	66.7	102	14.6	3.6	2.2	2.9

Patient ID	MAP (mmHg)	CBFV (cm/s)	HR (bpm)	ICP (mmHg)	RMSE (mmHg)	Bias (mmHg)	SDE (mmHg)
K	85.4	87.5	86	9.5	6.1	3.1	5.3
L	81.5	82.3	87	9.8	4.3	3.7	2.3
M	89.4	84.2	91	11.2	3.5	−2.6	2.2
N	93.9	27.3	91	8.2	3.1	2.7	1.5
O	80.5	43.2	96	11.0	2.2	2.2	0.5
P	80.1	59.4	86	22.1	14.5	−14	3.9
Q	77.9	45.6	92	15.3	4.8	−1.9	4.5
R	84.4	81.5	92	19.7	10.3	5.4	8.8
S	89.1	50.1	96	22.9	7.9	6.8	4
T	99.2	51.0	79	25.8	5.5	1	5.5
U	85.3	40.7	70	17.4	22.4	21.9	4.8
V	93.5	59.5	73	25.2	6	−3.8	4.9
W	80.3	69.4	90	24.8	11.1	−10.2	4.5
X	79.5	73.6	94	19.6	7	5.1	4.8
Y	89.2	34.1	76	5.0	11.4	−0.2	11.5
Z	74.6	24.5	79	12.9	3.4	−1.5	3.2
AA	77.7	31.4	84	13.9	8.2	6.5	4.9
AB	94.6	29.4	80	32.8	10.3	7.4	7.4
AC	99.6	40.7	69	34.6	11.8	−11.4	2.9
AD	112.6	115.3	100	19.8	6.6	−0.9	6.6
AE	107.9	146.3	67	20.2	5.8	5.3	2.5
AF	108.1	146.7	67	20.2	4.3	3	3.2
AG	100.5	113.1	81	21.2	3	0.3	3
AH	85.3	42.8	53	10.4	6.8	5.8	3.6
AI	95.8	34.2	110	13.4	15	14.2	4.5
AJ	78.1	32.5	74	35.5	9.3	9.1	1.9
AK	130.1	75.0	121	77.2	6.1	−5.7	2.1
AL	130.8	85.6	110	71.9	7.4	−6.7	3.2
AM	78.7	58.6	89	47.6	12.6	−12.5	1.9
AN	96.0	50.7	92	57.2	9.7	−9.6	1
AO	94.4	47.7	76	27.3	12.4	10.9	6
AP	86.1	30.1	80	27.3	7.8	3.8	6.8
AQ	87.1	24.5	107	43.4	5.4	−4.9	2.2
AR	80.8	66.2	55	14.8	4.4	4.3	1.3
AS	83.3	40.5	72	39.6	4.9	2.9	4

Table D.1: A record-by-record summary of clinical data and the ICP estimation error in all 45 patient records.

Appendix E

Correlation Coefficient Fails to Quantify Agreement

As argued in detail by Bland and Altman in their seminal papers [131, 132, 142], correlation or regression analysis is *not* the appropriate way to compare the agreement of two methods of measurement for some common underlying quantity. We use an expression for the correlation coefficient R between the results of the two methods of measurement to show that R can be low (near 0) even when agreement is good, and conversely, that R can be high (near 1) even when agreement is poor [1]. These conclusions are illustrated by testing agreement between an invasive ("gold-standard") measurement of ICP and a non-invasive estimate of it.

Perhaps part of the tendency in the literature to measure agreement using the correlation coefficient R (rather than a direct mean-square-error, for instance) results from inadequate recognition that the (unfortunately named) correlation coefficient is actually a normalized measure of *covariance* rather than correlation. Specifically, R is a measure of how the *deviation from the mean* for one variable relates to (or helps in linear prediction of) the *deviation from the mean* in the other variable. Thus R says nothing about how close or far apart the mean values themselves are (as Example 3 below makes abundantly clear).

[1] Apologies for the dual use of R, which everywhere in the document denotes cerebrovascular resistance but in this appendix stands for the correlation coefficient, following the convention used in the statistics literature. This appendix makes no reference to cerebrovascular resistance.

E.1 Assessing Agreement Between Two Measurement Modalities

For conceptual and notational simplicity, the analysis below is stated in terms of random variables, with their associated means, variances, covariances and correlation coefficients. However, all the expressions have direct counterparts in terms of *sample* means, variances, covariances and correlation coefficients.

Let P be the underlying random variable of interest (for instance, true ICP in a randomly chosen patient at a randomly selected time), and let G be the current clinical gold-standard measurement of P (or, more generally, a measurement of P obtained using a particular measurement modality, whose agreement with another measurement modality is to be assessed). We assume that G and P are related through the expression

$$G = P + W \ ,$$

where W is a random variable denoting measurement noise. Let us assume W has mean 0 and variance σ_W^2, while P has mean μ_P and variance σ_P^2. Then G has mean

$$\mu_G = \mu_P \ ;$$

and if we assume for simplicity that P and W are uncorrelated, then G has variance

$$\sigma_G^2 = \sigma_P^2 + \sigma_W^2 \ .$$

(The various assumptions can be relaxed, but the issues with correlation analysis can be illustrated even under these simplifying assumptions.) Using $E[X]$ to denote the expected (or mean) value of the random variable X, we can most directly assess the agreement of G and P by the mean-square-error:

$$E[(G - P)^2] = E[W^2] = \sigma_W^2 \ .$$

Now let F be a different measurement (or estimate) of P, obtained using a second measurement modality. We assume the relation

$$F = P + V,$$

where V denotes the measurement (or estimation) noise associated with this modality, with mean μ_V that may be nonzero (if F is a biased measurement or estimate), and variance σ_V^2. We again assume for simplicity that the noise V is uncorrelated with P, and also that it is uncorrelated with the noise W of the first (gold-standard) measurement modality. Then the mean and variance of F are respectively given by

$$\mu_F = \mu_P + \mu_V$$

and

$$\sigma_F^2 = \sigma_P^2 + \sigma_V^2 \ ,$$

while the covariance of F and G is

$$\sigma_{F,G} = \sigma_P^2 \ .$$

The agreement of F with P is assessed by the mean-square-error

$$E[(F-P)^2] = E[V^2] = \mu_V^2 + \sigma_V^2 \ .$$

We would consider F to be a good measurement (or estimate) of P if this level of agreement is comparable with that of the gold standard, i.e., if

$$\mu_V^2 + \sigma_V^2 \approx \sigma_W^2 \ .$$

The agreement of the two measurement modalities F and G is given by the mean-square-error

$$E[(F-G)^2] = E[V^2] + E[W^2] = \mu_V^2 + \sigma_V^2 + \sigma_W^2 \ .$$

If this is not much more than $2\sigma_W^2$, i.e., twice the variance of the gold-standard measurement, then we have an indication that the measurement F may be essentially as good as the gold standard G.

E.2 The Inadequacy of Correlation Analysis

Now examine the correlation coefficient of F and G, defined by

$$\rho_{F,G} = \frac{\sigma_{F,G}}{\sigma_F \sigma_G} = \frac{\sigma_P^2}{\sqrt{(\sigma_P^2 + \sigma_V^2)(\sigma_P^2 + \sigma_W^2)}} .$$

When this is computed as a *sample* correlation coefficient, it is denoted by r or R.

The problems with using the correlation coefficient as a measure of agreement become immediately evident from the above expression. Consider the following two scenarios, both of them very likely to be encountered in practice:

(1) If σ_P^2 is small compared to *either* σ_V^2 *or* σ_W^2 (or both), then the correlation coefficient $\rho_{F,G}$ will be small (near 0), *even if* F and G track P and each other well. (For our ICP estimation example, if — over the given data window — the excursions in underlying or true ICP are small compared to the standard deviations of either the measurement or estimation noises, then R will be small, even if the estimate tracks the measurement well. This is illustrated in Example 1 of the next section.)

(2) At the other extreme, if σ_P^2 is large compared to *both* the variances σ_V^2 *and* σ_W^2, then the correlation coefficient $\rho_{F,G}$ will be large (near 1), *even when* F and G do *not* track P or each other well. (For our ICP estimation example, if — over the given data window — the excursions in underlying or true ICP are large compared to the standard deviations of both the measurement and estimation noises, then R will be large, even when the estimate does not track the measurement well. This is illustrated in Example 2 of the next section.)

E.3 Examples

We now illustrate the above analysis with the help of three examples. In the first two examples below, both taken from our nICP estimation results (with G = ICP and F = nICP), we have estimated the required variances σ_P^2, σ_V^2 and σ_W^2 using the following expressions, which are easily derived:

$$\sigma_P^2 = \sigma_{F,G} \ ,$$
$$\sigma_W^2 = \sigma_G^2 - \sigma_{F,G} \ ,$$
$$\sigma_V^2 = \sigma_F^2 - \sigma_{F,G} \ .$$

The quantities on the right are in turn estimated directly from the data for F and G, by using the appropriate sample variances in place of the probabilistic variances.

Example 1 (Good Agreement, But Low Correlation)
To illustrate the first way in which a correlation analysis fails, we consider a pair of nICP estimate and measured ICP in a particular patient from our set of 45 patient records. The nICP estimate was computed over 7446 beats (total duration just above two hours). Given F and G for this patient, we compute the following quantities directly from the data vectors:

$$\sigma_G^2 = 4.9 \ , \sigma_F^2 = 9.9 \ , \sigma_{F,G} = 3.4 \ , \mu_V = 0.13 \ .$$

The derived variances obtained for P, W and V are

$$\sigma_P^2 = 3.4 \ , \sigma_W^2 = 1.5 \ , \sigma_V^2 = 6.5 \ .$$

All variances are given in mmHg^2. Thus, the estimation noise has a standard deviation of 2.5 mmHg, compared with 1.2 mmHg in the gold-standard measurement. Comparing the mean-square-error of the two methods also shows good agreement

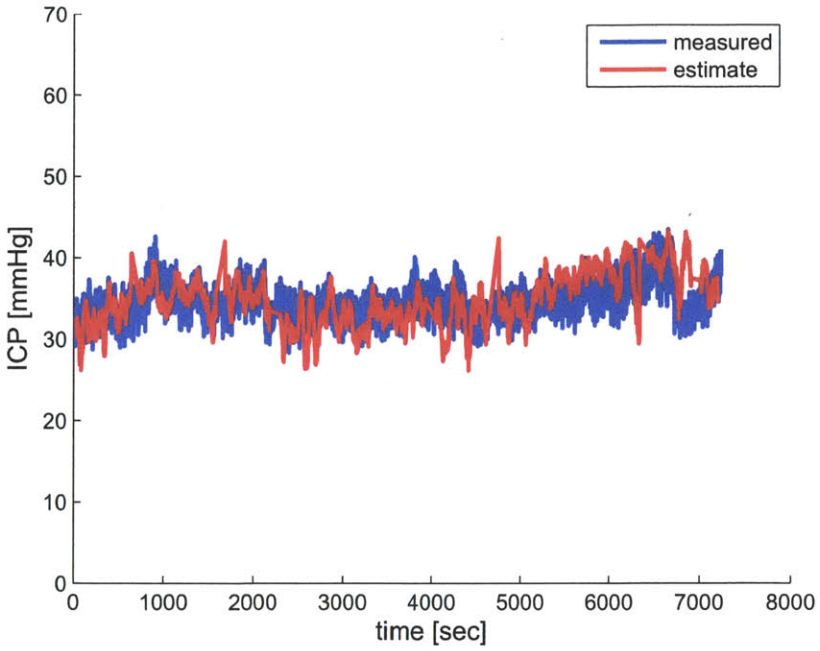

Figure E-1: Waveform comparison of non-invasive ICP estimate (red) against invasive ICP (blue) for Example 1.

between the two methods, only a difference of about 5 mmHg^2:

$$\mu_V^2 + \sigma_V^2 = 6.52 \text{ , while } \sigma_W^2 = 1.5 \text{ .}$$

The correlation coefficient works out to be $R = 0.49$, which would suggest a somewhat poor agreement between the two modalities for ICP determination. However, visual inspection of the measured and estimated ICP in Figure E-1 shows close agreement between the two modalities.

A Bland-Altman analysis and the difference/error histogram are shown in Figure E-2, which agree with visual inspection of the signals, and the story told by the comparison of mean-square-error: the bias is only 0.13 mmHg and the standard deviation of the difference is 2.8 mmHg (i.e., σ_{F-G}, where $\sigma_{F-G}^2 = \sigma_W^2 + \sigma_V^2$).

Example 2 (High Correlation, But Poor Agreement)

To illustrate the second way in which the correlation coefficient fails as a measure

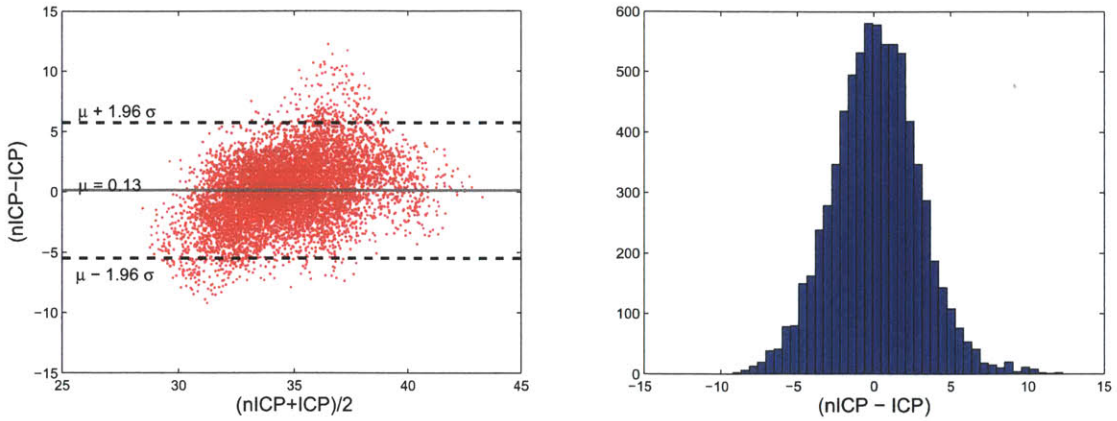

(a) Bland-Altman plot.

(b) Histogram of the error.

Figure E-2: A Bland-Altman plot and a histogram of error for the nICP estimate and invasive measurement of ICP in Example 1.

of agreement between two methods, we consider a different pair of nICP estimate and measured ICP. Given F and G for this patient record, we compute the following quantities directly from the data vectors

$$\sigma_G^2 = 234.2\ , \sigma_F^2 = 218.3\ , \sigma_{F,G} = 204.9\ , \mu_V = 12.9\ .$$

The derived variances are then

$$\sigma_P^2 = 204.9\ , \sigma_W^2 = 29.3\ , \sigma_V^2 = 13.4\ .$$

Comparing the mean-square-error of the two methods shows a relatively poor agreement, a difference of about 150 mmHg^2:

$$\mu_V^2 + \sigma_V^2 = 179.8\ , \text{while } \sigma_W^2 = 29.3\ .$$

Comparison of our nICP estimate against invasively measured ICP yields a correlation coefficient $R = 0.91$, which seems to suggest very good agreement. Figure E-3 shows waveforms of the measured and estimated ICP. While the correlation coefficient improved (0.91 compared with 0.49), visual inspection, the Bland-Altman analysis in

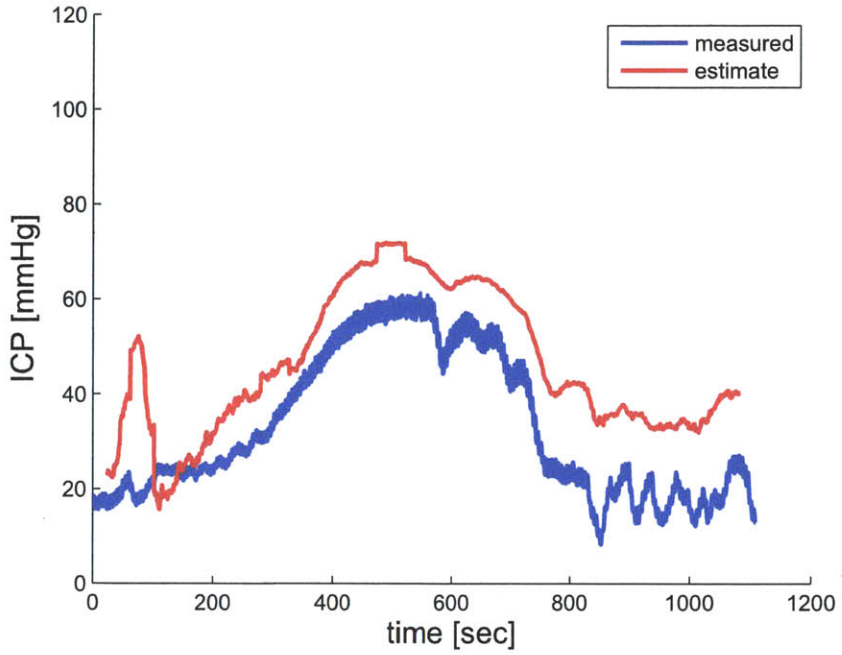

Figure E-3: Waveform comparison of non-invasive ICP estimate (red) against invasive ICP (blue) for Example 2.

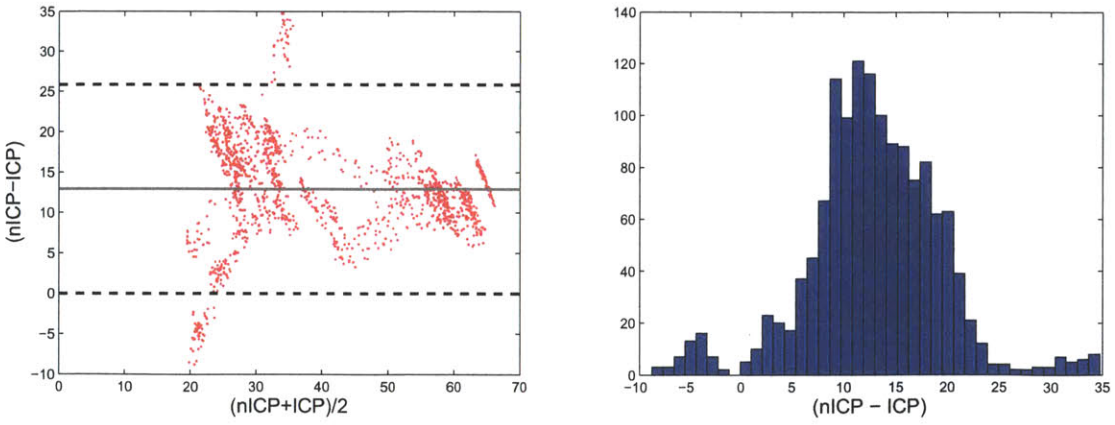

(a) Bland-Altman plot.

(b) Histogram of the error.

Figure E-4: A Bland-Altman plot and a histogram of error for the nICP estimate and invasive measurement of ICP in Example 2.

Figure E-4, and the mean-square-error all suggest that the estimation performance is inferior to the previous example: it has a larger bias of 12.9 mmHg, and the standard deviation of the difference is 6.5 mmHg.

Example 3 (Two extreme scenarios)

Examples 1 and 2 used the actual measurements of ICP and our nICP estimates in two patient records in order to show inadequacy of R to correctly evaluate the estimation performance (against the "gold standard" ICP). To conclude the discussion, we consider a final example by creating two extreme scenarios. Imagine two methods of assessing a common quantity. The first scenario is shown in Figure E-5(a), where the two methods agree with each other quite well, only differing due to a small fluctuation around a common mean. The bias is zero, and the mean-square-error is only 1 unit-squared, which indicate a very good agreement. However, the correlation coefficient R for the two time-series is 0. The second scenario is shown in Figure E-5(b). Visually it is clear that the two methods have a large difference between them. The bias and the mean-square-error, which are 20 units and 400 unit-squared respectively, also point to a large disagreement between the methods. However, the correlation coefficient R is 1. In both these scenarios, R clearly does not represent the level of

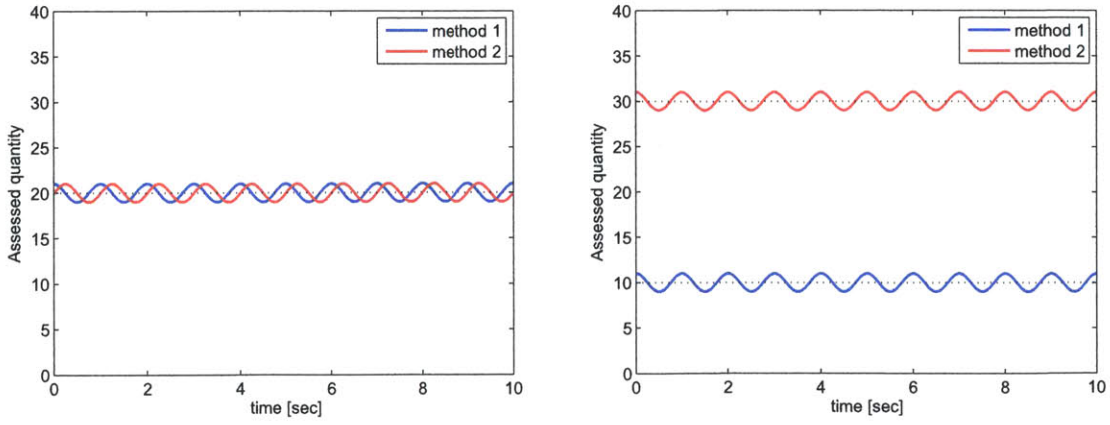

(a) Good agreement, but $R = 0$.

(b) Large difference, but $R = 1$.

Figure E-5: Two examples to show how the correlation coefficient R completely fails to quantify agreement between two methods of assessing a common quantity.

agreement between the two methods.

Summary

We hope that these examples have illustrated that the correlation coefficient is not a good summary statistic/measure to quantify agreement between two time-series, particularly when evaluating two methods to assess the same underlying variable.

Bibliography

[1] E. R. Kandel, J. H. Schwartz, and T. M. Jessell. *Principles of Neural Science.* Mcgraw Hill, New York, 4th edition, 2000.

[2] L. S. Costanzo. *Physiology.* Saunders, Elsevier, Philadelphia, 2nd edition, 2002.

[3] C. D. Clemente, editor. *Gray's Anatomy: Anatomy of the human body.* Lea & Febiger, Philadelphia, 30th edition, 1985.

[4] F. J. M. Walters. Intracranial pressure and cerebral blood flow. *Update in Anesthesia, Physiology*, 8:18–23, 1998.

[5] http://emcritic.org, Website accessed in February 2011.

[6] S. Sorek, J. Bear, and Z. Karni. Resistance and compliance of a compartmental model of the cerebrovascular system. *Annals of Biomedical Engineering*, 17:1–12, 1989.

[7] M. Ursino and C. A. Lodi. Interaction among autoregulation, CO_2 reactivity, and intracranial pressure: a mathematical model. *American Journal of Physiology - Heart and Circulatory Phsiology*, 274:1715–1728, 1998.

[8] S. A. Stevens, J. Stimpson, W. D. Lakin, N. J. Thakore, and P. L. Penar. A model for idiopathic intracranial hypertension and associated pathological ICP wave-forms. *IEEE Transaction on Biomedical Engineering*, 55(2):388–398, 2008.

[9] M. Ursino and C. A. Lodi. A simple mathematical model of the interaction between intracranial pressure and cerebral hemodynamics. *Journal of Applied Physiology*, 82:1256–1269, 1997.

[10] F. M. Kashif, T. Heldt, and G. C. Verghese. Model-based estimation of intracranial pressure and cerebrovascular autoregulation. *Computers in Cardiology*, 35:369–372, 2008.

[11] R. W. Brower and A. Noordergraaf. Pressure flow characteristics of collapsible tubes: A reconciliation of seemingly contradictory results. *Annals of Biomedical Engineering*, 1:333–335, 1973.

[12] J. P. Holt. The collapse factor in the measurement of venous pressure: The flow of fluid through collapsible tubes. *American Journal of Physiology*, 134:292–299, 1941.

[13] Y. Nakagawa, M. Tsuru, and K. Yada. Site and mechanism for compression of the venous system during experimental intracranial hypertension. *Journal of Neurosurgery*, 41:427–434, 1974.

[14] M. Chopp and H. D. Portnoy. Starling resistor as a model of the cerebrovascular bed. In *Ishii, I.; Nagai, H; and Brock, M. eds. Intracranial Pressure V*, pages 174–179, Berlin, Heidelberg, 1983. Springer-Verlag.

[15] J. D. Miller, D. P. Becker, J. D. Ward, H. G. Sullivan, W. E. Adams, and M. J. Rosner. Significance of intracranial hypertension in severe head injury. *Journal of Neurosurgery*, 47:503–516, 1977.

[16] The Brain Trauma Foundation. Guidelines for the management of severe traumatic brain injury, 3rd edition. *Journal of Neurotrauma*, 24:S1–S106, 2007.

[17] L. A. Steiner and P. J. Andrews. Monitoring the injured brain: ICP and CBF. *British Journal of Anaesthesia*, 97:26–38, 2006.

[18] R. Hlatky, A. B. Valadka, and C. S. Robertson. Intracranial hypertension and cerebral ischemia after severe traumatic brain injury. *Neurosurgury Focus*, 14:1–4, 2003.

[19] G. J. Bouma, J. P. Muizelaar, and S. C. Choi. Cerebral circulation and metabolism after severe traumatic brain injury: the elusive role of ischemia. *Journal of Neurosurgery*, 75:685–693, 1991.

[20] K. H. Chan, N. M. Dearden, J. D. Miller, P. J. Andrews, and S. Midgle. Multimodality monitoring as a guide to treatment of intracranial hypertension after severe brain injury. *Neurosurgery*, 32:547–553, 1993.

[21] A. Marmarou, R. L. Anderson, J. D. Ward, S. C. Choi, and H. F. Young. Impact of ICP instability and hypotension on outcome in patients with sever head trauma. *Journal of Neurosurgery*, 75:S59–S66, 1991.

[22] H. Feldmann, G. Klages, F. Gartner, and J. Scharfenberg. The prognostic value of intracranial pressure monitoring after severe head injuries. *Acta Neurochirurgica Supplement (Wien)*, 28:74–77, 1979.

[23] H. S. Levin, H. M. Eisenberg, H. E. Gary, A. Marmarou, M. A. Foulkes, J. A. Jane, L. F. Marshall, and S. M. Portman. Intracranial hypertension in relation to memory functioning during the first year after severe head injury. *Neurosurgery*, 28:196–200, 1991.

[24] R. Aaslid, T. M. Markwalder, and H. Norned. Noninvasive transcranial Doppler ultrasound recording of flow velocity in basal cerebral arteries. *Journal of Neurosurgery*, 57:769–774, 1982.

[25] A. J. du Plessis. Cerebrovascular injury in premature infants: current understanding and challenges for future prevention. *Clinical Perionatology*, 35(4):609–41, 2008.

[26] R. B. Panerai, A. W. R. Kelsall, J. M. Rennie, and D. H. Evans. Analysis of cerebral blood flow autoregulation in neonates. *IEEE Transactions on Biomedical Engineering*, 43(8):779–788, 1996.

[27] L. F. Marshall, R. W. Smith, and H. M. Shapiro. The outcome aggressive treatment in severe head injuries. Part I: the significance of intracranial pressure monitoring. *Journal of Neurosurgery*, 50:20–25, 1979.

[28] M. Czosnyka and J. D. Pickard. Monitoring and interpretation of intracranial pressure. *Journal of Neurology, Neurosurgery & Psychiatry*, 75:813–821, 2004.

[29] Z. Feldman and R. K. Narayan. Intracranial pressure monitoring: techniques and pitfalls. In *Head injury*, pages 247–274. Eds. P. R. Cooper, Williams and Wilkins, 1993.

[30] Czosnyka M., Brady K., Reinhard M., Smielewski P., and Steiner L. A. Monitoring of cerebrovascular autoregulation: facts, myths, and missing links. *Neurocritical care*, 10:373–386, 2009.

[31] W. Wakeland and B. Goldstein. A review of physiological simulation models of intracranial pressure dynamics. *Computers in Biology and Medicine*, 38:1024–1041, 2008.

[32] B. Schmidt, J. Klingelhöfer, J. J. Schwarze, D Sander, and I. Wittich. Noninvasive prediction of intracranial pressure curves using transcranial doppler ultrasonography. *Stroke*, 28:2465–2472, 1997.

[33] P. D. Mourad, B. Mohr, M. Kliot, and R. C. A. Frederickson. *Systems and methods for determining intracranial pressure non-invasively and acoustic transducer assemblies for use in such systems.* U.S. Patent 7,547,283, PhysioSonics, Inc., 2004.

[34] X. Hu, V. I. Nenov, and N. A. Martin. *Data mining system for noninvasive intracranial pressure assessment.* PCT/US2007/008534, University of California, 2007.

[35] O. Frank. Die Theorie der Pulswelle. *Zeitschrift fur Biologie*, 85:91–130, 1926.

[36] K. Sagawa, R. K. Lie, and J. Schaefer. Translation of Otto Frank's paper 'Die Grundform des arteriellen Pulses'. *Journal of Molecular and Cellular Cardiology*, 22:253–277, 1990.

[37] T. A. Parlikar. *Modeling and monitoring of cardiovascular dynamics for patients in critical care.* PhD thesis, Massachusetts Institute of Technology, Cambridge, MA, 2007.

[38] A. Monro. Observations on the structure and function of the nervous system. *Edinburgh: Creech & Johnson*, 1783.

[39] G. Kellie. Appearances observed in the dissection of two individuals; death from cold and congestion of the brain. *Transcripts Medical Surgical Society of Edinburgh*, 1:84–169, 1824.

[40] B. Mokri. The Monro-Kellie hypothesis: applications in CSF volume depletion. *Neurology*, 56(12):1746–1748, 2001.

[41] F. H. Martini, M. J. Timmons, and B. Tallitsch. *Human Anatomy.* Benjamin Cummings, Pearson, 6th edition, 2009.

[42] D. N. Irani. *Cerebrospinal Fluid in Clinical Practice.* Saunders (Elsevier Health Sciences), Philadelphia, 1st edition, 2008.

[43] M. A. Uddin, T. U. Haq, and M. Z. Rafique. Cerebral venous system anatomy. *Journal of the Pakistan Medical Association*, 56(11):516–519, 2006.

[44] K. Elf, P. Nilsson, E. Ronne-Engstrom, T. Howells, and P. Enblad. Cerebral perfusion pressure between 50 and 60 mm hg may be beneficial in head-injured patients: a computerized secondary insult monitoring study. *Neurosurgery*, 56:962–971, 2005.

[45] J. A. Friedman, V. G. Khurana, R. E. Anderson, and F. B. Meyer. Cerebral blood flow: Physiology and measurement techniques. In *Neurosurgery: Principles and Practice.* Eds. Moore, A.J. and Newell, D.W., Springer, 2005.

[46] J. G. McComb. Recent research into the nature of cerebrospinal fluid formation and absorption. *Journal of Neurosurgery*, 59:369–383, 1983.

[47] R. W. Cutler, L. Page, J. Galicich, and G. V. Watters. Formation and absorption of cerebrospinal fluid in man. *Brain*, 91:707–720, 1968.

[48] A. C. Guyton. *Textbook of Medical Physiology.* W. B. Saunders, Philadelphia, 8th edition, 1991.

[49] R. D. Adams, C. M. Fisher, S. Hakim, R. G. Ojemann, and W. H. Sweet. Symptomatic occult hydrocephalus with "normal" cerebrospinal pressures: a treatable syndrome. *The New England Journal of Medicine*, 273:117, 1965.

[50] A. Marmarou. *A theoretical model and experimental evaluation of the cerebrospinal fluid system.* PhD thesis, Drexel University, Philadelphia, 1973.

[51] S. Hakim, J. G. Venegas, and J. D. Burton. The physics of cranial cavity, hydrocephalus and normal pressure hydrocephalus: mechanical interpretation and mathematical model. *Surgical Neurology*, 5(3):187–210, 1976.

[52] A. Marmarou, K. Shulman, and R. M. Rosende. A nonlinear analysis of the cerebrospinal fluid system and intracranial pressure dynamics. *Journal of Neurosurgery*, 48:332–344, 1978.

[53] http://www.thamburaj.com, Website accessed in February 2011.

[54] G. J. Bouma and J. P. Muizelaar. Cerebral blood flow, cerebral blood volume, and cerebrovascular reactivity after severe head injury. *Journal of Neurotrauma*, 9(Supplement 1):S333, 1992.

[55] P. Mavrocordatos, B. Bissonette, and P. Ravussin. Effects of neck position and head elevation on intracranial pressure in anesthetized neurosurgical patients. *Journal of Neurosurgical Anesthesiology*, 12:10–14, 2000.

[56] L. A. Fleisher. *Evidence-Based Practice of Anesthesiology.* Saunders (Elsevier Health Sciences), Philadelphia, 1st edition, 2009.

[57] F. Munar, A. M. Ferrer, M. de Nadal, M. A. Poca, S. Pedraza, J. Sahuquillo, and A. Garnacho. Cerebral hemodynamic effects of 7.2% hypertonic saline in patients with head injury and raised intracranial pressure. *Journal of Neurotrauma*, 17:41–51, 2000.

[58] J. M. Drake, J. R. W. Kestle, and S. Tuli. Csf shunts 50 years on – past, present and future. *Childs Nervous System*, 16:800–804, 2000.

[59] http://www.americanheart.org, Accessed in February 2011.

[60] Institute of Medicine. *Long-Term Consequences of Traumatic Brain Injury.* Volume 7 of Gulf War and Health. National Academy of Scienes, Washington, DC, 2009.

[61] E. Singer. Brain Trauma in Iraq. *Technology Review*, 111:53–59, 2008.

[62] C. W. Hoge, D. McGurk, J. L. Thomas, A. L. Cox, C. C. Engel, and C. A. Castro. Mild traumatic brain injury in U.S. soldiers returning from Iraq. *The New England Journal of Medicine*, 358(5):453–463, 2008.

[63] K.M. Guskievicz, S.W. Marshall, J. Bailes, M. McCrea, R.C. Cantu, C. Randolph, and B.D. Jordan. Association between recurrent concussion and late-life cognitive impairment in retired professional football players. *Journal of Neurosurgery*, 57(4):719–726, 2005.

[64] B. E. Masel and D. S. DeWitt. Traumatic brain injury: a disease process, not an event. *Journal of Neurotrauma*, 27:1529–1540, 2010.

[65] P. C. Mifflin. *Saving Very Premature Babies: Key Ethical Issues.* Elsevier Health Sciences, 2003.

[66] Y. W. Wu, G. J. Escobar, J. K. Grether, L. A. Croen, J. D. Greene, and T. B. Newman. Chorioamnionitis and cerebral palsy in term and near-term infants. *Journal of the American Medical Association*, 290(20):2677–2684, 2003.

[67] D. Moster, R. T. Lie, and T. Markestad. Long-term medical and social consequences of preterm birth. *The New England Journal of Medicine*, 359(3):262–273, 2008.

[68] M. R. Bullock and M. Gugliotta. Pathophysiology. In J. Jallo and C. M. Loftus, editors, *Neurotrauma and Critical Care of the Brain*, chapter 2, pages 23–41. Thieme, New York, NY, 2009.

[69] D. DeWitt. Traumatic cerebral vascular injury: the effects of concussive brain injury on the cerebral vasculature. *Journal of Neurotrauma*, 20(9):795–825, 2003.

[70] A. Säljö, B. Svensson, M. Mayorga, A. Hamberger, and H. Bolouri. Low-level blasts raise intracranial pressure and impair neurocognitive function in rats. *Journal of Neurotrauma*, 26:1345–1352, 2009.

[71] A. Marmarou. A review of progress in understanding the pathophysiology and treatment of brain edema. *Neurosurgury Focus*, 22(5):E1, 2007.

[72] Defense and Veterans Brain Injury Center. *Screening and diagnosis of Military mTBI: Review and analysis.* Wright Patterson AFB, OH, 2009.

[73] Defense Centers of Excellence (DCoE) For Psychological Health & Traumatic Brain Injury. *Portable, Field-Based Devices for the Early Diagnosis of Mild Traumatic Brain Injury.* www.dcoe.health.mil, September 20, 2010.

[74] B. I. Omalu, S. T. DeKosky, R. L. Minster, M. I. Kamboh, R. L. Hamilton, and C. H. Wecht. Chronic traumatic encephalopathy in a National Football League player. *Journal of Neurosurgery*, 57(1):128–134, 2005.

[75] N. Lundberg. Continuous recording and control of ventricular fluid pressure in neurosurgical practice. *Acta Psychiatrica et Neurologica Scandinavica*, 36(Supplement 149):1–193, 1960.

[76] A. Raabe, R. Stöckel, D. Hohrein, and J. Schöche. An avoidable methodological failure in intracranial pressure monitoring. *Acta Neurochirurgica Supplement*, 71:59–61, 1998.

[77] K. Banister, I. R. Chambers, M. S. Siddique, Femandes H. M., and A. D. Mendelow. Intracranial pressure and clinical status: assessment of two intracranial pressure transducers. *Physiological Measurement*, 21:473–479, 2000.

[78] J. D. Miller. Inaccurate pressure readings for subarachnoid bolts. *Neurosurgery*, 19(2):253–255, 1986.

[79] I. Piper, A. Barnes, D. Smith, and L. Dunn. The Camino intracranial pressure sensor: Is it optimal technology? An internal audit with a review of current intracranial pressure monitoring technologies. *Neurosurgery*, 49:1158–1165, 2001.

[80] M. H. Morgalla, L. Krasznai, K. Dietz, H. Mettenleiter, M. Deininger, and E. H. Grote. Methods of experimental and clinical assessment of the relative measurement accuracy of an intracranial pressure transducer. *Journal of Neurosurgery*, 95:529–532, 2001.

[81] I. R. Chambers, M. S. Siddiqui, K. Banister, and A. D. Mendelow. Clinical comparison of the spiegelberg parenchymal transducer and ventricular fluid pressure. *Journal of Neurology, Neurosurgery & Psychiatry*, 71:383–385, 2001.

[82] A. Raabe, R. Totzauer, O. Meyer, R. Stöckel, D. Hohrein, and J. Schöche. Reliability of epidural pressure measurement in clinical practice: behavior of three modern sensors during simultaneous ipsilateral intraventricual or intraperenchymal pressure measurement. *Neurosurgery*, 43:306–311, 1998.

[83] P. K. Eide. Comparison of simultaneous intracranial pressure (ICP) signals from ICP sensors placed within the brain parenchyma and epidural space. *Medical Engineering & Physics*, 30:34–40, 2008.

[84] R. Aaslid, K. F. Lindegaard, W. Sorteberg, and H. Nornes. Cerebral autoregulation dynamics in humans. *Stroke*, 20:45–52, 1989.

[85] T. David and S. Moore. Modeling perfusion in the cerebral vasculature. *Medical Engineering Physics*, 30:1227–45, 2008.

[86] R. B. Panerai. Complexity of the human cerebral circulation. *Philosophical Transactions of the Royal Society A*, 367:1319–1336, 2009.

[87] M. Ursino and C. A. Lodi. A mathematical study of human intracranial hydrodynamics Part 1 — the cerebrospinal fluid pulse pressure. *Annals of Biomedical Engineering*, 16(4):379–401, 1988.

[88] M. Ursino and C. A. Lodi. A mathematical study of human intracranial hydrodynamics Part 2 — simulation of clinical tests. *Annals of Biomedical Engineering*, 16(4):403–416, 1988.

[89] R. B. Panerai. Cerebral autoregulation: from models to clinical applications. *Cardiovascular Engineering*, 8:42–59, 2008.

[90] M. Jachan, M. Reinhard, L. Spindeler, A. Hetzel, B. Schelter, and J. Timmer. Parametric versus nonparametric transfer function estimation of cerebral autoregulation from spontaneous blood-pressure oscillations. *Cardiovascular Engineering*, 9:72–82, 2009.

[91] R. Zhang, J. H. Zuckerman, C. A. Giller, and B. D. Levine. Transfer function analysis of dynamic cerebral autoregulation in humans. *American Journal of Physiology - Heart and Circulatory Phsiology*, pages 233–241, 1998.

[92] R. B. Panerai, D. M. Simpson, S. T. Deverson, P. Mahony, P. Hayes, and D. H. Evans. Multivariate dynamic analysis of cerebral blood flow regulation in humans. *IEEE Transactions on Biomedical Engineering*, 47(3):419–423, 2000.

[93] G. B. Boylan, K. Young, R. B. Panerai, J. M. Rennie, and D. H. Evans. Dynamic cerebral autoregulation in sick newborn infants. *Pediatric Research*, 48(1):12–17, 2000.

[94] J. S. Bendat and A. G. Piersol. *Random Data*. Wiley-Interscience, 1986.

[95] F. P. Tiecks, A. P. Lam, R. Aaslid, and D. W. Newell. Comparison of static and dynamic cerebral autoregulatory measurements. *Stroke*, 26:1014–1019, 1995.

[96] M. Czosnyka, P. Smielewski, P. Kirkpatrick, D. K. Menon, and J. D. Pickard. Monitoring of cerebral autoregulation in head-injured patients. *Stroke*, 27:1829–1834, 1996.

[97] A. Lavino, E. Schmidt, C. Haubrich, P. Smielewski, J.D. Pickard, and M. Czosnyka. Noninvasive evaluation of dynamic cerebrovascular autoregulation using Finapres plethysmograph and transcranial Doppler. *Stroke*, 38:402–404, 2007.

[98] C. Zweifel, A. Lavinio, L. A. Steiner, D. Radolovich, P. Smielewski, I. Timofeev, M. Hiler, M. Balestreri, P. J. Kirkpatrick, J. D. Pickard, P. Hutchinson, and M. Czosnyka. Continuous monitoring of cerebrovascular pressure reactivity in patients with head injury. *Neurosurgury Focus*, 25:E2, 2008.

[99] X. Hu, A. W. Subudhi, P. Xu, S. Asgari, R. C. Roach, and M. Bergsneider. Inferring cerebrovascular changes from latencies of systemic and intracranial pulses: a model-based latency subtraction algorithm. *Journal of Cereb Blood Flow Metabolism*, 29:688–697, 2009.

[100] M. S. Olufsen, A. Nadim, and L. A. Lipsitz. Dynamics of cerebral blood flow regulation explained using a lumped parameter model. *American Journal of Physiology*, 282:R611–R622, 2002.

[101] P. W. Hanlo, R. J. Peters, R. H. Gooskens, R. M. Heethaar, R. W. Keunen, A. C. van Huffelen, C. A. Tulleken, and J. Willemse. Monitoring intracranial dynamics by transcranial doppler — a new Doppler index: trans systolic time. *Ultrasound in Medicine and Biology*, 21(5):613–621, 1995.

[102] A. Reid, R. J. Marchbanks, D. E. Bateman, A. M. Martin, A. P. Brightwell, and J. D. Pickard. Mean intracranial pressure monitoring by a non-invasive audiological technique: a pilot study. *Journal of Neurology, Neurosurgery & Psychiatry*, 52:610–612, 1989.

[103] T. Ueno, R. E. Ballard, L. M. Shuer, J. H. Cantrell, W. T. Yost, and A. R. Hargens. Noninvasive measurement of pulsatile intracranial pressure using ultrasound. *Acta Neurochirurgica*, 71:66–69, 1998.

[104] B. Schmidt, M. Czosnyka, A. Raabe, H. Yahya, J. J. Schwarze, D. Sackerer, D. Sander, and J. Klingelhöfer. Adaptive noninvasive assessment of intracranial pressure and cerebral autoregulation. *Stroke*, pages 84–89, 2003.

[105] B. Schmidt, M. Weinhold, M. Czosnyka, S. A. May, R. Steinmeier, and J. Klingelhöfer. Accuracy of non-invasive ICP assessment can be increased by an initial individual calibration. *Acta Neurochirurgica Supplement*, 102:49–52, 2008.

[106] P. B. Raksin, N. Alperin, A. Sivaramakrishnan, S. Surapaneni, and T. Lictor. Noninvasive intracranial compliance and pressure based on dynamic magnetic resonance imaging of blood flow and cerebrospinal fluid flow: review of principles, implementation, and other noninvasive approaches. *Neurosurgery Review*, 14(4):e4, 2003.

[107] M. Swoboda, M. G. Hochman, and F. J. Fritz. *Non-invasive intracranial pressure sensor.* U.S. Patent Pub. No. US 2010/0204589 A1, NeuroDx Development, 2010.

[108] W. Wakeland, R. Agbeko, K. Vinecore, M. Peters, and B. Goldstein. Assessing the prediction potential of an in silico computer model of intracranial pressure dynamics. *Critical Care Medicine*, 37(3):1079–1089, 2009.

[109] H. W. Querfurth. *Methods of and systems and devices for assessing intracranial pressure non-invasively.* U.S. Patent 7,122,007 B2, Caritas St. Elizabeth Medical Center of Boston, Inc., 2006.

[110] A. Ragauskas, G. Daubaris, A. Dziugys, V. Azelis, and V. Gc drimas. Innovative non-invasive method for absolute intracranial pressure me surement without calibration. *Acta Neurochirurgica Supplement*, 95:357–361, : 005.

[111] F. Bono, D. Messina, C. Giliberto, D. Cristiano, G. B oussard, F. Fera, F. Condino, A. Lavano, and A. Quattrone. Bilateral tran verse sinus stenosis predicts IIH without papilledema in patients with mi raine. *Neurology*, 67:419–423, 2006.

[112] M. T. Torbey, R. G. Geocadin, A. Y. Razumovsky, D. Rig monti, and M. A. Williams. Utility of CSF pressure monitoring to identify i liopathic intracranial hypertension without papilledema in patients with chro ic daily headache. *Cephalalgia*, 24:495–502, 2003.

[113] W. D. Lakin, S. A. Stevens, B. I. Tranmer, and P. L. Per ar. A whole-body mathematical model for intracranial pressure dynamics. *Jo rnal of Mathematical Biology*, 46:347–383, 2003.

[114] R. B. Panerai. Modelling cerebral blood flow autoregulat on in humans. In *EMBS Proceedings of the 23rd Annual International Confe ence of the IEEE*, volume 1, pages 240–243, 2001.

[115] V. Novak, A. Yang, L. Lepicovsky, A. Goldberger, L. Lipsit , and C.-K. Peng. Multimodal pressure-flow method to assess dynamics of cere ral autoregulation in stroke and hypertension. *BioMedical Engineering Online* 3(39), 2004.

[116] T. Heldt, R. Mukkamala, G. B. Moody, and R. G. Mark. C /Sim: a cardiovascular simulator for teaching and research. *The Open Pacin , Electrophysiology and Therapy Journal*, 3:45–54, 2010.

[117] T. Heldt. *Computational Models of Cardiovascular Respc nse to Orthostatic Stress.* PhD thesis, Harvard MIT Division of Health Scienc s and Technology, Massachusetts Institute of Technology, Cambridge, MA, 20(4.

[118] G. C. Verghese. Getting to the gray box: Some challenges for model reduction. Inaugural plenary lecture, *American Control Conference*, St. Louis, MO, June 2009.

[119] E. P. Ahearn, K. T. Randall, J. D. Charlton, and R. N. Johnson. Two compartment model of the cerebrospinal fluid system for the study of hydrocephalus. *Annals of Biomedical Engineering*, 15(5):467–484, 1987.

[120] M. Czosnyka, S. Piechnik, H. K. Richards, P. Kirkpatrick, P. Smielewski, and J. D. Pickard. Contribution of mathematical modelling to the interpretation of bedside tests of cerebrovascular autoregulation. *Journal of Neurology, Neurosurgery & Psychiatry*, 63:721–731, 1997.

[121] C. A. Lodi and M. Ursino. Hemodynamic effect of cerebral vasospasm in humans: A modeling study. *Annals of Biomedical Engineering*, 27:257–273, 1999.

[122] M. C. Aoi, C. T. Kelley, V. Novak, and M. S. Olufsen. Optimization of a mathematical model of cerebral autoregulation using patient data. In *Proceedings of the 7th IFAC Symposium on Modeling and Control in Biomedical Systems*, pages 181–186, Denmark, 2009.

[123] G. P. Molhoek, K. H. Wesseling, J. J. Settels, E. van Vollenhoven, H. W. H. Weeda, B. de Wit, and A. C. Arntzenius. Evaluation of the Penaz servoplethsymo-manometer for the continuous, non-invasive measurement of finger blood pressure. *Basic Research in Cardiology*, 79:598–609, 1984.

[124] J. Penaz. Photoelectric measurement of blood pressure, volume and flow in the finger. In *Digest of the 10th International Conference on Medical and Biological Engineering. eds: A. Albert, W. Vogt, W. Hellig*, Dresden, 1973.

[125] G. Parati, R. Casadei, A Groppelli, M. D. Rienzo, and G. Mancia. Comparison of finger and intra-arterial blood pressure monitoring at rest and during laboratory testing. *Hypertension*, 13(6):647–655, 1989.

[126] D. W. Baker. Pulsed ultrasonic Doppler blood-flow sensing. *IEEE Trans Sonics Ultrasonics*, Su-17:170–182, 1970.

[127] C. H. Chen, E. Nevo, B. Fetics, P. H. Pak, F. C. P. Yin, W. L. Maughan, and D. A. Kass. Estimation of central aortic pressure waveform by mathematical transformation of radial tonometry pressure: validation of generalised transfer function. *Circulation*, 95:1827–1836, 1997.

[128] M. Karamanoglu, D. E. Gallagher, A. P. Avolio, and M. F. O'Rourke. Pressure wave propagation in a multi-branched model of the human upper limb. *American Journal Physiology: Heart and Circulatory Physiology*, 269:H1363–H1369, 1995.

[129] W. Zong, T. Heldt, G. B. Moody, and R. G. Mark. An open-source algorithm to detect onset of arterial blood pressure pulses. *Computers in Cardiology*, 34:259–262, 2003.

[130] T. A. Parlikar, T. Heldt, G. V. Ranade, and G. C. Verghese. Model-based estimation of cardiac output and total peripheral resistance. *Computers in Cardiology*, 34:379–82, 2007.

[131] J. M. Bland and D. G. Altman. Statistical methods for assessing agreement between two methods of clinical measurement. *Lancet*, i:307–310, 1986.

[132] D. G. Altman and J. M. Bland. Measurement in medicine: the analysis of method comparison studies. *The Statistician*, 32:307–317, 1983.

[133] M. Hayashi, Y. Handa, H. Kobayashi, H. Kawano, H. Ishii, and S. Hirose. Plateau-wave phenomenon (I). *Brain*, 114:2681–2691, 1991.

[134] M. Hayashi, H. Kobayashi Y. Handa, , H. Kawano, S. Hirose, and H. Ishii. Plateau-wave phenomenon (II). *Brain*, 114:2693–2699, 1991.

[135] M. van de Bor and F. J. Walther. Cerebral blood flow velocity regulation in preterm infants. *Biology of the Neonate*, 59:329–335, 1991.

[136] B. Schaller. Physiology of cerebral venous blood flow: from experimental data in animals to normal function in humans. *Brain Research Reviews*, 46:243–260, 2004.

[137] R. D. Kamm. Flow through collapsible tubes. In *Handbook of Bioengineering.* Eds. R. Skalk and S. Chien, McGraw Hill, 1986.

[138] J. M. Luce, J. S. Huseby, W. Kirk, and J. Butler. A Starling resistor regulates cerebral venous outflow in dogs. *Journal of Applied Physiology*, 53:1496–1503, 1982.

[139] F. M. Kashif, T. Heldt, and G. C. Verghese. *Systems and methods for cerebrovascular modeling and for noninvasive or minimally invasive estimation of intracranial pressure and autoregulation.* U.S. Provisional Patent Application 61/095,892, filed September 10, 2008.

[140] F. M. Kashif, T. Heldt, and G. C. Verghese. *Systems, Devices and Methods for Noninvasive or Minimally-Invasive Estimation of Intracranial Pressure and Cerebrovascular Autoregulation.* U.S. Patent Application 12/555,713, filed September 8, 2009.

[141] G. P. Rao and H. Unbehauen. Identification of continuous-time systems. *IEE Proceedings of Control Theory Applications*, 153(2):185–220, 2006.

[142] http://www-users.york.ac.uk/ mb55/meas/ba.htm, Website accessed in July 2010.